UNIVERSITÀ
POLITECNICA
DELLE MARCHE

Facoltà di Ingegneria Informatica
Dottorato di Ricerca in Ingegneria dell'Informazione

Adaptation of the Segmented Beat Modulation Method to support diagnosis of cardiovascular disorders using electrocardiographic tracings acquired by wearable sensors

Candidate:
Amnah Nasim

Advisor:
Professor Laura Burattini

Academic Year 2017-2020

UNIVERSITÀ
POLITECNICA
DELLE MARCHE

Facoltà di Ingegneria Informatica
Dottorato di Ricerca in Ingegneria dell'Informazione

Adaptation of the Segmented Beat Modulation Method to support diagnosis of cardiovascular disorders using electrocardiographic tracings acquired by wearable sensors

Candidate:
Amnah Nasim

Advisor:
Professor Laura Burattini

Academic Year 2017-2020

Università Politecnica delle Marche
Facoltà di Ingegneria Informatica
Dottorato di Ricerca in Ingegneria dell'Informazione
Via Brecce Bianche – 60131 Ancona (AN), Italy

Dedicated to my parents and my lovely sister.

Acknowledgments

Throughout the writing of this dissertation and overall the course of my research at Università Politecnica Delle Marche, I have received a great deal of support and assistance from both my professional and personal circles.

First of all, I would like to thank my supervisor, Professor Laura Burattini, whose expertise was invaluable in formulating the research questions and methodology. Your insightful feedback pushed me to sharpen my thinking and brought my work to a higher level. You provided me with the tools that I needed to choose the right direction and successfully complete my dissertation. From critical thinking to polishing my scientific writing, I am forever obliged for your patience, guidance and mentorship.

I would like to acknowledge my very kind colleague Ilaria Marcantoni for always being a person with positive vibes, Agnese Sbrollini for her critical analysis and feedback that helped me improve my research skills and Micaela Morettini for being a perfectionist proofreader for all my paper manuscripts. I especially thank Prof. Franchesco Di Nardo for being an extremely kind and supportive person the entire duration of my stay at UNIVPM. You have been a really good sport.

I would also like to thank my Professors back in Pakistan, Dr. Aneela Zameer, Dr. Adnan Maqsood, Dr. Ahmed Ejaz Nadeem (RIP) and Mr. Sikandar Hayat Mirza for being a great source of encouragement throughout my career.

In addition, I would like to thank my mother and my lovely sister for their wise counsel and sympathetic ear. You are my strength. A special thanks to my father. You are my root. Finally, I could not have completed this dissertation without the support of my friends, Jiaojiao Zhang for sticking together through the thick and thin of living abroad, Sehrish Akhter for being full of positivity and hope and lastly Farzeen Munir who provided stimulating discussions as well as happy distractions to rest my mind outside of my research.

Ancona, November 2020

Amnah Nasim

Abstract

Designing automatic cardiovascular disease (CVD) diagnostic systems specifically for signals acquired using wearable electrocardiogram (ECG) sensors becomes a challenge specifically requiring solutions for signal distortions caused by high level of motion artifacts and efficient CVD diagnosis. Hence the aim of this thesis is to develop an adaptation of Segmented Beat Modulation Method (SBMM, a template-based method for denoising of ECG signals) using wearable ECG data to additionally account for non-sinus rhythms and to increase the usability of modern wearable sensors in comparison to traditional in-clinic machines for CVD diagnosis. SBMM has currently failed to work with abnormal or arrhythmic (rare but critical events often leading to sudden cardiac death) heartbeats which hugely limits its applicability to cardiovascular disease diagnosis in a real-world scenario. To this aim, this work presents Extended Segmented Beat Modulation Method with a heartbeat classification function using convolutional neural network (CNN) that first separates the normal (N) from supraventricular (S) and ventricular (V) heartbeats and secondly uses separate median representative templates to denoise and reconstruct the clean ECG recording. Overall, the CNN classification accuracy (Ac) was 91.5% while the positive predictive (PP) values were 92.8%, 95.6%, and 83.6%, for N, S, and V beat classes, respectively. Eventually, signal-to-noise (SNR) improvement was less than 2 dB in the absence of noise but increased in the presence of noise until exceeding 5 dB in the presence of electrode motion artifacts. Hence, ESBMM proved to be a reliable tool to classify cardiac beats into N, S, and V classes and to denoise ECG tracings characterized by both sinus and non-sinus rhythms maintaining the morphological variability in the pseudo-periodic ECG signal. Other improvements proposed to SBMM are a preliminary compression test using discrete cosine transform. The method is evaluated using SNR and compression ratio (CR) considering varying levels of signal energy in the reconstructed ECG signal. For denoising, an average SNR of 4.56 dB was achieved representing an average overall decline of 1.68 dBs (37.9%) as compared to the uncompressed signal processing while 95% of signal energy is intact and quantized at 6 bits for signal storage (CR=2) compared to the original 12 bits, hence resulting in 50% reduction in storage size. Another improvement dynamic-template SBMM adapts SBMM to heart rate and generates the template in a dynamic fashion every 20 seconds and is particularly targeted and tested for long-term ECG data acquisitions. Another presented improvement adapts SBMM to modern fast hardware using vectorization technique and graphical processing units called GPU-SBMM. GPU-SBMM application yielded a significant increase of SNR

(from 1±5 dB to 19±5 dB; $p < 10^{-10}$). Additionally, a considerable speed up in the algorithm runtime (3.56x on average on an NVIDIA GeForce GPU) was achieved. In a secondary domain, an automated arrhythmia detection system is presented that is designed to produce maximum diagnostic accuracy with minimum amount of data (removing redundant and noisy data) using differential evolution (DE) and a less computationally intense probabilistic neural network (PNN). All tests are performed for ambulatory and long term ECG signals acquired using wearable sensing modality. The proposed DE-PNN scheme provides better classification accuracy considering 8 classes with only 41 features optimized from a 253 element feature set implying an 83.7% reduction in direct amplitude features compared to the other evolutionary and statistical schemes. In conclusion, this work has proved beneficial for improving the quality and efficiency of automatic cardiovascular disease diagnosis system on a modern and evolving cardiovascular health monitoring platform i.e. wearable ECG sensors.

Sommario

Lo scopo di questa tesi è adattare il Segmented Beat Modulation Method (SBMM), un metodo per il filtraggio di segnali electrocardiografici (ECG), per tenere conto sia dei ritmi cardiaci sinusali che non e per aumentare la sua usabilità includendo i moderni sensori indossabili oltre ai tradizionali dispositivi clinici per la diagnosi di patologie cardiovascolari. Infatti, SBMM non è attualmente in grado di funzionare in presenza di battiti cardiaci anormali o aritmici (eventi critici che potrebbero portare allaa morte cardiaca improvvisa), il che limita enormemente la sua applicabilità alla diagnosi di malattie cardiovascolari in uno scenario reale. A questo scopo, questo lavoro presenta il Extended Segmented Beat Modulation Method (ESBMM) con una funzione di classificazione del battito cardiaco utilizzando la convolutional neural network (CNN) che separa prima i battiti cardiaci normali (N) da quelli sopraventricolari (S) e ventricolari (V), e in secondo luogo utilizza modelli rappresentativi mediani separati per filtrare e ricostruire la registrazione ECG pulita. Nel complesso, l'accuratezza (Ac) della classificazione CNN era del 91,5% mentre i valori di predizione positive erano del 92,8%, 95,6% e 83,6%, rispettivamente per le classi di battito N, S e V. Alla fine, il miglioramento del rapporto segnale-rumore (SNR) è stato inferiore a 2 dB in presenza di livelli di rumore trascurabile, ma è aumentato in presenza di rumore fino a superare i 5 dB in presenza di artefatti da movimento degli elettrodi. Pertanto, ESBMM si è dimostrato uno strumento affidabile per classificare i battiti cardiaci in classi N, S e V e per filtraggio di tracciati ECG caratterizzati da ritmi sia sinusali che non sinusali mantenendo la variabilità morfologica nel segnale ECG pseudo-periodico. Altri miglioramenti proposti a SBMM sono un test di compressione preliminare che utilizza la trasformata coseno discreta. Il metodo viene valutato utilizzando SNR e il rapport di compressione (CR) considerando diversi livelli di energia del segnale ECG ricostruito. Per il filtraggio, è stato raggiunto un SNR medio di 4,56 dB che rappresenta un calo complessivo medio di 1,68 dB (37,9%) rispetto all'elaborazione del segnale non compresso mentre il 95% dell'energia del segnale è intatto e quantizzato a 6 bit per la memorizzazione del segnale (CR=2) rispetto ai 12 bit originali, con conseguente riduzione del 50% delle dimensioni di archiviazione. Un altro miglioramento è l'adattamento dell'SBMM alla frequenza cardiaca in modo dinamico ogni 20 secondi, particolarmente indicato per l'acquisizione di dati ECG a lungo termine. Un altro miglioramento presentato adatta SBMM al moderno hardware veloce utilizzando la tecnica di vettorizzazione e le unità di elaborazione grafica chiamate GPU-SBMM. L'applicazione GPU-SBMM ha prodotto un aumento significativo dell'SNR (da 15 dB a 195 dB; p<10-10). Inoltre, è stata raggiunta una

notevole velocità nel runtime dell'algoritmo (3,56x volte GPU NVIDIA GeForce). In aggiunta, viene presentato un sistema automatico di rilevamento dell'aritmia progettato per produrre la massima precisione diagnostica con una quantità minima di dati utilizzando differential evolution (DE) e una probabilistic neural network (PNN) meno pesante dal punto di vista computazionale. Tutti i test sono stati eseguiti su ECG ambulatoriali e a lungo termine acquisiti utilizzando sensoristica indossabile. Lo schema DE-PNN proposto ha fornito una migliore accuratezza di classificazione considerando 8 classi con solo 41 caratteristiche ottimizzate da un insieme di 253 elementi che hanno causato una riduzione dell'83,7% delle caratteristiche di ampiezza diretta. In conclusione, questo lavoro si è dimostrato utile per migliorare la qualità e l'efficienza del sistema di diagnosi automatica delle malattie cardiovascolari su una piattaforma di monitoraggio della salute cardiovascolare moderna e in evoluzione, ovvero sensori ECG indossabili.

Summary

Electrocardiogram (ECG) signals acquired using wearable sensors are often a source of inaccurate information due to noise especially signal distortions arising due to body movements of the patient or subject. Hence, designing diagnostic systems specifically for signals acquired using wearable ECG sensors becomes a challenge. The aim of this thesis was to design and develop algorithms that overcome the limitation of Segmented-Beat Modulation Method (SBMM) of being applicable to only normal sinus beats and extend its applications to everyday long-term monitoring scenarios and fast-processing hardware devices. SBMM is a template-based filtering technique used to clean noisy ECG signals proposed by Prof. Laura Burattini in 2014 being applicable to only normal sinus rhythm cardiac cycles (CC) (SBMM algorithm has also been patented in 2014). Template-based techniques usually do not reproduce beat-to-beat heart rate variability. Instead SBMM, due to the modulation procedure that prolongs the template for short beats and shortens the template for long beats, can adjust for short-term as well as long-term heart rate variability.

To this aim, a novel Extended Segmented-Beat Modulation Method (ESBMM) was dveloped that adds a classification function based on a convolutional neural network (CNN) to classify the beats into three beat classes selected among the five beat classes defined by the American National Standards Institute (ANSI) and the Association for the Advancement of Medical Instrumentation (AAMI) standard (ANSI/AAMI EC57:1998) and further apply SBMM for the denoising of arrhythmic beats. ESBMM includes four main steps: (1) CC identification (PQRST, onset: 250 ms before the R-peak position, offset: 250 ms before the next consecutive R-peak position) and segmentation into PQRS and TU segments; (2) wavelet-based time-frequency feature extraction; For each CC, a feature vector was computed. The feature vector was constructed using temporal intervals, features obtained by applying discrete wavelet transform to the modulated CC, and statistical features. The features related to temporal intervals are RR interval and CC duration. The features based on the 'Daubechies 4' wavelet transform of the modulated CC are obtained using decomposed wavelet coefficients at detail levels 4 to 7 (cD4, cD5, cD6, and cD7). The statistical features are kurtosis (4th order statistics) and skewness (3^{rd} order statistics) calculated respectively, for the entire CC, and of P (onset: 250 ms before the R-peak position, offset: 40 ms before the R-peak position), QRS (onset: 250 ms before and after the R-peak position), and TU (onset: 40 ms after the R-peak position, offset: 40 ms before the next consecutive R-peak position) waves taken from the modulated CC since they represent the morphological distortion of the entire CC and

of P, QRS, and TU waves, respectively. (3) CNN-based classification to discriminate among normal (N), supraventricular (S), and ventricular (V) beats. True AAMI beat labels were used as references during training; and (4) a template-based denoising procedure. ESBMM was tested using the MIT-BIH arrhythmia database (developed by the collaborative efforts of Massachusetts Institute of Technology and Boston's Beth Israel Hospital) and available opensource at Physionet (https://physionet.org). A noise robustness study was performed by adding three different noise types typically affecting the ECG i.e. baseline wander, muscle activity, and electrode motion artifacts to the input ECG signal. All noise signals were taken from the MIT-BIH Noise Stress Test database also available on Physionet and consist of real noise recordings acquired through ECG electrodes located on the limbs. Both clean and corrupted versions of each ECG segment were eventually submitted to the ESBMM in order to evaluate its robustness to noise in terms of accuracy (Acc), positive predictivity (PP) of N, S and V beats, and signal-to-noise ratio improvement. Overall, the classification Acc was 91.5% while the positive predictive values were 92.8%, 95.6%, and 83.6%, for N, S, and V classes, respectively. The signal-to-noise ratio (SNR) improvement after filtering was between 0.15 dB and 2.66 dB, with a median value equal to 0.99 dB, which is significantly higher than 0 ($p<0.05$). Regarding noise robustness, Acc and PP of N were only slightly affected by noise; PP of S decreased significantly only in the presence of electrode motion artifacts; and PP of V was affected by all types of noise even though it remained at least at 60%. Eventually, SNR improvement was less than 2 dB in the absence of noise but increased in the presence of noise until exceeding 5 dB in the presence of electrode motion artifacts. In conclusion, ESBMM proves to be a reliable tool to classify cardiac beats into N, S, and V classes and to denoise ECG tracings characterized by both sinus and non-sinus rhythms.

Portable ECG sensors are defining the future of continuous, long-term and automatic cardiac health monitoring nowadays. The target problem for ECG acquisition and processing through patch-based wearable sensors is the noise induced by motion artifacts during ADL. Another novel improvement of SBMM with dynamic template newly computed every 20 seconds to make the algorithm applicable particularly for novel wearable ECG sensing device usage in daily life scenarios technically called activities of daily living (ADL). The algorithm was tested using a unique compilation of ADL and different types of falls performed by human subjects using a MARG sensor positioned at the subject's waist while performing different activities: drinking coffee, typing keyboard, pressing and releasing signal electrode, walking at 1 and 3 miles per hour and running at 5 and 7 miles per hour inducing diverse motion artifacts. This work used the ADL records for the analysis of human body movements only. Results stratified by daily activities indicate that dynamic-template SBMM filtering yields an overall improvement in signal-to-noise ratio for ECG signals corrupted by motion artifacts supporting the hypothesis that the dynamic-template SBMM is an efficient denoising algorithm for ECG signal processing acquired through wearable sensors.

Currently used 24-hour ECG monitors have been shown to skip detecting arrhythmias that may not occur frequently or during standardized ECG test. Hence, online ECG processing and wearable sensing applications have been becoming increasingly popular in the past few years to solve a continuous and long-term ECG monitoring problem. With the increase in the usage of online platforms and wearable devices, there arises a need for increased storage capacity to store and transmit lengthy ECG recordings, offline and over the cloud for continuous monitoring by clinicians. Hence, to test the applicability of SBMM to long-term, online and wearable ECG monitoring scenario, a data compression and signal quality trade-off assessment was performed in case of compressed data. In this work, a discrete cosine transform compressed SBMM is proposed and its applicability in case of ambulatory ECG monitoring is tested using MIT- BIH ECG Compression Test Database containing Holter recordings. The method is evaluated using SNR and compression ratio (CR) considering varying levels of signal energy in the reconstructed ECG signal. For denoising, an average SNR of 4.56 dB was achieved representing an average overall decline of 1.68 dBs (37.9%) as compared to the uncompressed signal processing while 95% of signal energy is intact and quantized at 6 bits for signal storage (CR=2) compared to the original 12 bits, hence resulting in 50% reduction in storage size.

Sport-related sudden cardiac death (SRSCD), defined as "death occurring during sport or within one hour of cessation of training", is the leading cause of death in athletes. SRSCD occurs in the presence of underlying cardiovascular pathologies, some of which may be identified by processing ECG recordings acquired during training (TECGs). Popular wearable monitoring sensors of cardiac activity are typically used for training optimization. Still, they can also provide useful information for SRSCD risk assessment. However, for a timely prediction of critical events, TECGs from wearable sensors need to be efficiently and accurately processed during or immediately after training. This is a challenging task since TECGs are typically highly corrupted by noise and interferences, which may jeopardize their interpretation and identification of critical morphologies. Another improvement to SBMM to adapt it to GPU acceleration to make it compatible with modern hardware. The study aimed to evaluate the ability of the SBMM to denoise TECGs, and to improve SBMM implementation by GPU acceleration to make it compatible with modern hardware. To this aim, 19 4-to-6 min TECGs (sampling frequency: 256 Hz), acquired from 8 subjects while performing 4 different exercise tasks (walk, run, low-resistance bike and high-resistance bike), were analyzed. Signal-quality improvement was evaluated by computing the SNR for power of TECGs before and after GPU-SBMM application. Speed-up factor due to GPU acceleration was also evaluated. Results indicate that GPU-SBMM application yielded a significant increase of SNR (from 1±5 dB to 19±5 dB; $p< 10^{-10}$). Additionally, a considerable speed up in the algorithm runtime (3.56x on average on an NVIDIA GeForce GPU) was achieved. In conclusion, GPU-SBMM proves to be an efficient and accurate algorithm for TECG processing and may help fighting SRSCD.

Computer-aided ECG arrhythmia classification systems are popular nowadays that use intelligent techniques for the development of smart healthcare monitoring platforms. Using all the features calculated during feature extraction and a multi-layered classifier not only introduces heavy computational cost but also affects classifier performance due to the presence of redundant/corrupted features. Latest systems deploy a feature reduction/optimization step before classification to remove all unnecessary features. This also allows the use of a single layered or a computationally less intensive learning algorithm for classification. Therefore, to extract sufficient features and reduce their dimensions for classifiers to achieve optimal classification results is the primary task in the design of latest ECG arrhythmia classification systems. In this work, a heartbeat classification method was developed and tested based on evolutionary feature optimization using differential evolution (DE) and probabilistic neural network (PNN) as classifier to discriminate between normal and arrhythmic heartbeats. The presented method follows four steps: (1) preprocessing, (2) feature extraction and normalization, (3) DE feature optimization, and (4) PNN classification. First, using ECG records from the MIT-BIH arrhythmia database, heartbeats are identified using R-peak positions (onset: 250 ms before R-peak, offset: 450 ms after the R-peak) to extracting a sample representing complete beat morphology. Then, eight types of heartbeats are extracted from the complete set of beats using beat labels provided by MIT-BIH database. The identified ECG beat samples are then normalized by the Z-score method to reduce the signal amplitude biases from instrumental and human differences. In the next step, DE method is applied to reduce and optimize the direct beat morphology features. An initial population matrix is generated to represent the possible solution/optimization space. Randomly selecting two different individuals from the parent population, a 1-point crossover is performed. A bit-flip is performed with mutation probability 0.2 for all the population individuals. A novel fitness function modelled as the k-category Matthew's correlation coefficient is applied to optimize (minimize) the features that provide maximum precision for all eight beat classes. Fitness function for each individual in the population is calculated using the current-to-best strategy. This optimization procedure is run for 200 generations with 50 population size. This process evolves and accumulates better individuals until the termination criteria is reached. The process of optimization terminates if either the fitness value is stagnant for continuous 20 generations (stops improving) or user-selected 200 generations are reached. Lastly, a PNN (consisting of an input layer, a pattern layer, a summation layer, and an output layer.) classifier is employed to classify eight types of ECG arrhythmias, which are normal, left bundle branch block, right bundle branch block, premature ventricular contraction, atrial premature, ventricular escape, ventricular flutter wave and paced beat. Classification metrics; accuracy, F-score, area under the curve and Matthew's correlation coefficient are reported and compared. All measures are reported for both 'All features' and 'Optimized features' cases to present a comparison between classification improvement and feature reduction achieved using

the proposed method. The average number of generations by which the optimization is achieved was 7812. The DE-PNN scheme could classify normal with an accuracy of 99.45%, premature ventricular contraction with 99.18%, paced with 100.00%, right bundle branch block with 99.94%, left bundle branch block with 99.80%, atrial premature with 99.76%, ventricular flutter with 99.61%, and ventricular escape condition with 99.94% accuracy. The proposed DE-PNN scheme can provide better classification accuracy considering 8 classes with only 41 features optimized from a 253 element feature set implying an 83.7% reduction in direct amplitude features compared to the other evolutionary and statistical schemes, which validates that the proposed method can serve as a highly accurate and computationally efficient tool for automated diagnosis of heart diseases based on ECG signals.

In a minor domain, primarily to understand the effects of motion artifacts on signals acquired using wearable devices, 3 basic tests were conducted using recurrence quantification analysis (RQA), a technique is used to differentiate and analyze the regular and irregular parts of a time-series signal using recurrence plots and quantification measures. The first study presents RQA for human body movements during routine ADL using parameters recorded using a wearable sensor attached to the test subject's waist. The current research uses data from 8 subjects performing 5 different daily life activities, lying and stand, pick and stand, sitting and stand, step up and down, and walking. Simulating the RQA plots for activity and non-activity phases for squared vector magnitude parameter for each of the record we quantify the level of signal stability and disruption in terms of RQA analysis measures recurrence rate (RR), determinism (DET) and line entropy (ENT). The RQA parameters reveal a chaotic behavior in case of activity (RR=0.249, DET=0.510, ENT=0.732), and a stable or least chaotic behavior in case of non-activity (RR=0.466, DET=0.726, ENT=1.205) regions of time. The second study presents RQA of multiple ECG time series simultaneously recorded through different electrodes and depicts the effect of motion artifacts through electrode synchronization and non-synchronization. The ECG data is acquired from a healthy 25-year-old male performing different exercise activities such as standing, walking and jumping. Also, the electrode in every recorded signal is placed at angle offset of 0, 45 and 90. The RQA analysis measures RR, ENT and average diagonal length (L) reveal a highly stable and least chaotic signal in case of standing (RR=0.73, ENT=4.94, L=106.12), somewhat stable and a bit chaotic in case of walking (RR=0.75, ENT=5.35, L=129.13) and least stable and most chaotic in case of subject performing a jump (RR=0.61, ENT=5.07, L=99.16). Secondly, highest and second highest disturbances with respect to exercise movements are observed for electrode combinations (3,4) and (1,4). The third and most recent work presents RQA parameters as novel features for characterization of a fall event in case of backward and forward types of falls using data acquired through wearable sensors. Injuries caused by different types of falls are one of the vital health threats to the elder community living independent or otherwise. Characterization and detection of a fall event can trigger an alert and minimize the damage. Computing

cross recurrence plots and recurrence parameters; RR, DET and ENT for pre-fall, fall and post-fall phases, the level of signal stability and non-stability is quantified. The recurrence parameters show a stable behavior in case of pre-fall (RR=0.74, DET=0.85, ENT=4.36) and chaotic behavior in case of fall (RR=0.39 DET=0.80, ENT=3.13). To assess the discriminating capability of novel recurrence features, a support vector machine (SVM) is used to perform binary classification for pre-fall and fall classes. The SVM results in overall accuracy of 76% with a positive prediction of 82% for fall and 70% for pre-fall events.

Contents

List of Figures

List of Tables

Chapter 1

Cardiovascular diseases

Cardiovascular diseases (CVDs) are a group of disorders of the heart and blood vessels. CVDs including both heart and circulatory malfunctions manifest mostly in the form of heart attacks and stroke. Heart attacks and strokes caused by any blockage that stops the flow of blood to the heart or brain and are usually termed as acute events. The most common reason for this blockage is the accumulation of fatty deposits on the inner walls of the blood vessels that supply blood to the heart and brain. The major causes of strokes is bursting and bleeding of a blood vessel in the brain due to the formation of blood clots. The prevalent cause of heart attacks and strokes are usually the presence of a multitude of risk factors mainly categorized into 1) behavioral risk factors such as smoking, obesity, high alcohol consumption, unhealthy diet and physical inactivity and 2) pre-existing medical conditions such as high cholesterol, hypertension, diabetes, and hyperlipidaemia. Other important factors include, age, gender, genetics, sleep disorders and high stress levels. The effects of behavioral risk factors may show up in individuals as increased blood pressure, increased level of blood glucose, increased blood lipids, and obesity. These “intermediate risks factors” can be measured in primary care facilities and indicate an increased risk of developing a heart attack, stroke, heart failure and other complications. Decreasing or quitting altogether the use of tobacco, reducing of salt in everyday foods, adding more vegetables and fruits to the diet, exercising regularly and avoiding excessive alcohol consumption have been shown to reduce the risk of cardiovascular disease. Additionally, medical drug treatment of diabetes, hypertension and high blood lipids may be necessary to reduce cardiovascular risk and prevent heart attacks and strokes. People at high risk of cardiovascular disease due to the existence of one or more pre-existing medical conditions mentioned before need early detection and management using counselling and medicines, as appropriate. Moreover, health policies that create conducive environments for making healthy choices available and affordable are essential for motivating people to adopt and sustain healthy behavior. There are also a number of underlying determinants of CVDs or "the causes of the causes". These are a reflection of the major forces driving social, economic and cultural change – globalization, urbanization and population ageing. Other determinants of CVDs include poverty, stress and hereditary factors.

The biggest reason CVDs go undetected for a long period of time are the fact

that there are no visible symptoms that can timely identify the underlying CVD. A heart attack or stroke may be the first warning of an underlying CVD. The main symptoms of a heart attack include pain or discomfort in the central area of the chest; pain or discomfort in the arms, the left shoulder, elbows, jaw, or back. Additionally, the patient may encounter shortness of breath or difficulty in breathing; feeling light-headed or faint; feeling nauseous or vomiting; having cold sweats and becoming pale. The most common symptom of a stroke is sudden weakness of the face, arm, or leg, most often on one side of the body. Other symptoms include sudden onset of: numbness of the face, arm, or leg, especially on one side of the body; confusion, difficulty speaking or understanding speech; difficulty seeing with one or both eyes; difficulty walking, dizziness, loss of balance or coordination; severe headache with no known cause; and fainting or unconsciousness.

WHO identifies highly cost effective and affordable mediating actions also termed as 'Best buys' that can also be implemented in low-resource situations. Two types of such intervening actions are required to reduce the cardiovascular disease burden, 1) individual and 2) population-wide. Examples of population-wide interventions that can be implemented to reduce CVDs include: comprehensive tobacco control policies, taxation to reduce the intake of foods that are high in fat, sugar and salt, building walking and cycle paths to increase physical activity and strategies to reduce harmful use of alcohol. At the individual level, for prevention of first heart attacks and strokes, individual health-care interventions need to be targeted to those at high total cardiovascular risk or those with single risk factor levels above traditional thresholds, such as hypertension. The former approach is more cost-effective than the latter and has the potential to substantially reduce cardiovascular events. This approach is feasible in primary care in low-resource settings, including by non-physician health workers. For secondary prevention of cardiovascular disease in those with established disease, including diabetes, treatment with the following medications are necessary: aspirin, beta-blockers, statins. The benefits of these interventions are largely independent, but when used together with smoking cessation, nearly 75% of recurrent vascular events may be prevented. Currently there are major gaps in the implementation of these interventions particularly at the primary health care level. In addition costly surgical operations are sometimes required to treat CVDs. They include: coronary artery bypass, balloon angioplasty (where a small balloon-like device is threaded through an artery to open the blockage), valve repair and replacement, heart transplantation, artificial heart operations. Medical devices are required to treat some CVDs. Such devices include pacemakers, prosthetic valves, and patches for closing holes in the heart. People experiencing these symptoms should seek medical care immediately.

CVDs are further categorized as 1) vascular diseases that include: coronary heart disease (disease of the blood vessels supplying the heart muscle also called ischemic heart disease), peripheral arterial disease (disease of blood vessels supplying the arms and legs), cerebrovascular disease (disease of the blood vessels supplying the brain

includes stroke), renal artery stenosis (narrowing of one or both renal arteries blocking the blood flow to kidneys), aortic aneurysms (enlargement of the aorta causing aortic rupture) and 2) diseases including the heart that include: cardiomyopathy (diseases of cardiac muscle), hypertensive heart disease (diseases of the heart secondary to high blood pressure or hypertension), congenital heart disease (malformations of heart structure existing at birth), rheumatic heart disease (damage to the heart muscle and heart valves from rheumatic fever) and deep vein thrombosis and pulmonary embolism (blood clots in the leg veins, which can dislodge and move to the heart and lungs) etc.

1.1 Global CVD statistics

More people die annually from CVDs than from any other cause. An estimate provided by WHO states that 17.3 million people died from CVDs in 2008, constituting 30% of all global deaths. Of these deaths, an estimated 7.3 million were due to coronary heart disease and 6.2 million were due to stroke. Over 80% of CVD deaths happen in low- and middle-income countries. The cause of this highly CVD death in low- and middle-income countries compared to the global statistic is lack of integrated primary health care facilities for early diagnosis and appropriate quality treatment of people with high risk factors. As a result, many people in low- and middle-income countries are detected late in the course of the disease and die younger from CVDs and other noncommunicable diseases (NCD), often in their most productive years. The poorest people in low- and middle-income countries are affected most. At the household level, sufficient evidence is emerging to prove that CVDs and other NCDs contribute to poverty due to catastrophic health spending and high out-of-pocket expenditure. At macro-economic level, CVDs place a heavy burden on the economies of low- and middle-income countries. WHO projects that by 2030, almost 23.6 million people will die from CVDs, mainly from heart disease and stroke [10].

Tobacco use has been described as, 'the single largest avoidable health risk in the European Union' by the European Commission Directorate-General for Health and Food safety. A latest report by WHO, the World Heart Federation and the University of Newcastle Australia, confirms that a strong cause of morbidity and mortality due to coronary heart disease is tobacco smoking. Coronery heart disease is the leading cause of disability and death globally and is the reason for the loss of 9.4 million lives. Out of these, around 1.9 million (or approximately 21%) are attributable to tobacco use and exposure to second-hand smoke. Furthermore, the evidence shows that all types of tobacco and nicotine products contribute to heart disease, with smokeless tobacco being responsible for around 200000 annual deaths globally from coronary heart disease. E-cigarettes are also not harmless; their use raises blood pressure which increases the risk of cardiovascular disease. The global number of smokers, currently estimated at 1.3 billion, is projected to increase to 1.7 billion by the year 2025 if the increase in frequency of tobacco use remains unaffected [11].

Excessive tobacco use is related to many types of cancer and CVDs and is a major driving factor for death for approximately 6 million people annually. In Europe, for males and females aged $\geq$ 15 years, the median prevalence of regular daily smoking by 2014 estimates was 21%, based on data gathered from 29 ESC member countries. Prevalence figures range from lowest 11.9% in Sweden to highest 36.1% in Latvia [12].

Alcohol consumption defined as the amount of pure alcohol consumed in liters per adult (>15 years) over a calendar year and is a European Core Health Indicator [13] Excessive alcohol consumption remains a leading cause of premature death in the USA where it led to approximately 95,000 deaths and 2.8 million years of potential life lost each year in the United States from 2011 – 2015, shortening the lives of those who died by an average of 29 years and is responsible for 1 in 10 deaths among working-age adults [14]. In the EU, harmful alcohol use is the third biggest cause of premature death after tobacco and hypertension with alcohol dependence estimated to be responsible for more than 60% of all alcohol-attributable mortality [12]. Cultural and religious factors are likely to contribute to the very low alcohol consumption in many Middle East and North African countries.

Insufficient physical inactivity defined as the proportion of the population attaining less than 150 minutes of moderate-intensity physical activity per week or less than 75 minutes of rigorous-intensity is also one of the major CVD risk factors and is a cause of coronary heart disease, stroke, peripheral artery disease and heart failure [15]. Physical inactivity doubles the risk of developing heart disease and increases the risk of hypertension by 30%. It also double the risk of dying from CVD and stroke. Every year, more than 2 million deaths are attributable to physical inactivity worldwide [16]. Also the prevalence of overweight and obesity, defined by a body mass index (BMI) of $\geq$25 kg/m^2 and $\geq$30 kg/m^2, respectively, is increasing in both developed and developing countries. More people are now obese than are underweight both globally and in most regions of the world [17, 18].

1.2 CVD diagnosis methodologies

There are different types of medical tests acquired by different machines that provide information about the heart condition. Besides the basic heart rate and blood pressure check, other tests used to diagnose an abnormal function of the heart include:

1. Blood test
2. Echocardiogram
3. Stress test
4. Chest X-ray

5. Cardiac computerized tomography (CT) scan
6. Cardiac magnetic resonance imaging (MRI)
7. Cardiac catheterization
8. Electrocardiogram (ECG)
9. Wearable Holter monitoring

Most of these tests are either too expensive to be affordable for general public or invasive causing discomfort for the patient or have complex acquisition procedures that the patient might just want to avoid. Also due to the nature of some tests, they might not be able to provide a complete information about many heart abnormalities. These factors decrease their use in an everyday clinical diagnostic scenario. ECG is a noninvasive test widely used in hospitals and clinics due to ease of use, is affordable compared to other cardiac diagnostic tests and provides a quick result that provides the clinicians an early chance to detect any critical pathology.

1.3 Novel wearable vs traditional in-clinic ECG machines

Traditional in-clinic ECG machines are used to quantify the electrical activity of the heart spanning a brief period of time mostly a 10 second ECG test. This exam provides general physicians and cardiologists with information about potentially critical or non-critical cardiovascular conditions. Getting precise diagnostic measures is of extreme importance in such circumstances, especially if the patient has medical or genetic history of heart disease. Most of the heart abnormalities may not be displayed exactly in that brief time of ECG test but rather occur at any non-specific moment. Hence, traditional ECG in-clinic modality may not be able to detect correctly and in-time the type and extent of the CVD which is crucial in the treatment and hence prevention of CVD-related death. Current trends in wireless ECG monitoring systems have produced an innovative and versatile approach to wearable, wireless and mobile ECG devices for long-term and continuous monitoring of heart conditions. One of the biggest benefits of wearable ECG sensors is the increased accuracy. Different research studies and validation tests have presently proven that wearable ECG technology performs far better than clinical ECG machines [19, 20]. Lack of using a lot of wires makes it more difficult for the patient to misplace the electrodes due to sudden arm movement. Wearable ECG electrodes are more comfortable and less intrusive than the wires that otherwise encircle the chest and upper body of the patient. The discomfort connected to traditional machines is significant. Electrodes remain secured in the right place until the exam finishes. The placement of electrodes on the patient's chest is also simple and efficient. The main body of the wearable ECG device can either be attached to the belt of the patient or it can be placed on a table such as in Holter machines. Such machines are very easy to use even at home.

Placement is easy, wearing is comfortable and the main unit has to be nowhere near the body of the patient. All these advantages make the wearable ECG devices preferred by both doctors and patients who have to monitor their heart rate on a regular basis.

One such wide used example is a Holter monitor. Holter device presents a portable ECG monitoring system for real-time, continuous and long-term recording of a patient's ECG for CVD diagnosis [21, 22]. Holter ECG monitoring is the most extensively used technique for wearable sensing until now. Also there are many other devices but with less usability currently than Holter. For example, Zephyr Bioharness [23, 24] is a wireless and chest-based belt-type wearable device, capable of long-term recording of various physiological parameters, including heart rate, respiratory rate, body temperature, posture and activity levels. Blue Box [25] is a small wearable device that acquires and wirelessly transmits important cardiac parameters of ECG like heart rate, systolic time intervals, beat interval and ventricular depolarization duration. Another commercially available biosensing device called StressEraser [26] provides enhanced heart rate variability signal. Some similar belt-based systems were developed for wireless health monitoring [27]. Other popular wearable ECG sensing devices include smart textiles (shirts) [28, 29, 30, 31, 32] . Specific examples include LOBIN [28] which integrates wireless sensor networks (WSN) and e-textile into a smart shirt for ECG monitoring. BIOTEX, a wearable textile biosensor which collects physiological body parameters and additionally the elemental composition of body fluids particularly sweat. This device embeds sensors for pH, sodium level detection, conductivity [33]. MOPET is a mobile wearable system that oversees a physical fitness activity for better training and motivating users [34].

Tele-monitoring bio-signals using wearable, wireless and mobile devices is nowadays considered as one of the best means to continuously gather and analyze the critical signs from home or a remote location (meaning outside the hospital or clinic). Separately from the benefits that this mobile technology offers, there are also some limitations to this fast evolving technology which carry a potential window of improvement. A common problem with wearable ECG devices is signal quality deterioration in case of body movements during performance of daily life activities. This is particularly called body movement noise and is explained in section 2.3.4 in detail. Also, since the ECG data is being continuously accumulated throughout the day, efficient processing and compression methods are required to appropriate deal with this huge amount of data.

Furthermore, it has been proved that the ECG can be recorded without the use of a gel and hardware and software-based solutions like low pass, high pass, and notch filters can easily be used to free the signal from baseline and motion artefact noise. Apprehensions regarding the harmful effect of surface electrodes on human skin are also to some degree addressed [35] with recommendations for the best electrode placements [36]. Wearable ECG data acquisition and collection has progressed to the extent that many studies have successfully analyzed the performance of leadless

[37] and contactless [38] and ECG monitoring. Hence, this work particularly deals with the signals acquired through the now popular wearabe ECG sensors.

1.4 Problem identification

In order to meet a medical standard and clinically accepted monitoring system, early detection of abnormal conditions, accurate decision support and high quality and real-time patient data acquisition need to be considered. ECG signals acquired using wearable sensors are often a source of inaccurate information due to noise especially signal distortions arising due to body movements of the patient or subject. Hence, designing diagnostic systems specifically for signals acquired using wearable ECG sensors becomes a challenge. The limitations mainly come from the fact that these technical algorithms commonly are data-driven and compute-intensive and hence imply a significant computing overhead, which necessitates the use of high-end hardware systems with high compute capability.

According to [1] wearable ECG signal processing and investigation essentially faces three most important and challenging issues:

- Amplification of signal and its A/C conversion
- Noise elimination
- Feature selection

The quality and effectiveness of the methods used at these steps imply the quality of the overall process of classification and interpretation of ECG signals. Both signal amplification and A/C conversion issues are related to hardware while noise elimination and feature selection (meaning removal of noisy and redundant data plus the use of only optimum and least possible amount of data for processing) are realized through the use of advanced technologies of information processing.

Hence, this work in major domain deals with noise elimination by improving SBMM and in minor domain, with feature reduction/optimization algorithms specifically targeted for cardiovascular disease diagnosis and tested for ECG signals acquired using wearable sensing devices.

1.5 Proposed Solutions

The work proposed in this thesis mainly concerns with the noise elimination and efficient diagnosis of different CVDs particularly targeted for signals acquired using wearable ECG sensors. Particular work includes:

1. Extended Segmented Beat Modulation Method (ESBMM): Segmented Beat Modulation Method (SBMM) as in previously published works [4, 39, 39, 6,

40, 41] although had proven noise elimination and robustness capability, had limited applicability solely normal or sinus rhythm ECG recordings. ESBMM overcomes this limitation and adds a classification (diagnosis) function for ventricular and supraventricular non-sinus or arrhythmia heartbeats keeping the morphological variability intact throughout the recording.

2. GPU-based SBMM (GPU-SBMM): Adapting the original SBMM [4, 39, 39, 6, 40, 41], for modern and fast-processing device hardware, GPU-SBMM is a vectorized and GPU-based implementation particularly tested and proven efficient for the case of sport-related sudden cardiac death in athletes.

3. Discrete cosine transform compressed SBMM (DCT-SBMM): Adapting the original SBMM [4, 39, 39, 6, 40, 41] to the case of long-term and continuous recordings using wearable sensors, DCT-SBMM is a preliminary test performed to check the denoising capability of SBMM in case of compressed ECG signals.

4. Dynamic-template SBMM (Dynamic-SBMM): Adapting the original SBMM [4, 39, 39, 6, 40, 41] where there was only one representative median template generated for the whole ECG record, dynamis-SBMM generates a new template every 20 seconds and hence is able to adapt to changes in HR.

5. Differential Evolution-based feature optimization with Probabilistic Neural Network for heartbeat classification (DE-PNN): This research proposes a DE framework for optimizing/reducing the number of features used for arrhythmia diagnosis and has a wide diagnosing capability for 1 normal and 7 types of arrhythmia heartbeats hence presenting an efficient and accurate solution for cardiovascular health monitoring in wearable sensing scenarios.

6. Recurrence Quantification Analysis (RQA) for body movement analysis (minor domain): In an attempt to understand the dominant body movements affecting signals acquired using wearable sensors, a couple of studies were performed to model body movements using different signals acquired using wearable sensing devices.

1.6 Organization of the thesis document

Chapter 1 — Cardiovascular diseases

The first chapter gives a brief insight into CVDs, presents some world-wide CVD statistics regarding yearly diagnosed cases and rate of mortality. A description of basic methods used for the diagnosis including different acquisition modalities (instruments and signals) and latest computational intelligence based solutions is provided. Furthermore, advantages of now wearable sensing ECG sensors over traditional clinical systems is explained. Finally the chapter concludes by giving a

brief account of the identified problem and proposed solution followed through the rest of this document.

Chapter 2 — The Electrocardiogram

Chapter 2 provides a detailed introductory account of all the concepts regarding ECG signal and the methods used to propose novel solutions to the defined problem. The chapter also attempts to cover all the concepts used in the rest of this document that might be helpful for the reader in understanding the thesis.

Chapter 3 — Segmented Beat Modulation Method

Chapter 3 revises the Segmented Beat Modulation Method (SBMM) and some of the important application areas in which it has been previously used. The chapter includes a discussion on the pros and cons of previously published SBMM algorithm and gives an account of the identified shortcomings that need an extension or improvement.

Chapter 4 — Extended Segmented Beat Modulation Method

Chapter 4 details a solution Extended Segmented Beat Modulation Method (ESBMM) presented as an extended version of SBMM to fight the limitations of SBMM of being applicable to only sinus rhythm and increase the clinical utility of SBMM.

Chapter 5 — Compressed Segmented Beat Modulation Method

Chapter 5 details a solution DCT Compressed Segmented Beat Modulation Method (DCT-SBMM) presented as an extended version of SBMM to work with compressed ECG signals to increase utility of SBMM with long-term recorded data using wearable sensors.

Chapter 6 — GPU-based Segmented Beat Modulation Method

Chapter 6 details a solution GPU-based Segmented Beat Modulation Method (GPU-SBMM) presented as an extended version of SBMM to work with compressed ECG signals to increase utility of SBMM to perform a clinical analysis of sport-related sudden cardiac death application.

Chapter 7 — Dynamic-template Segmented Beat Modulation Method

Chapter 7 details a solution Dynamic Segmented Beat Modulation Method (Dynamic-SBMM) presented as an extended version of SBMM to adapt to changing heart rate and generate the median template anew every 20 seconds to be used during daily life activities.

Chapter 8 — Differential Evolution-based feature optimization of ECG signals

Chapter 8 details a background of evolutionary algorithms in general and differential evolution in specific used in different optimization domain for ECG signal. The proposed solution using differential evolution for feature optimization and probabilistic neural networks for classification for 1 normal and 7 types of cardiac arrhythmia beats using wearable ECG signals.

Chapter 9 — Recurrence Analysis of Human Body Movements

Chapter 9 includes 3 preliminary human movement modelling scenarios attempted to understand the effect of human body movement in general and on the ECG signal acquired using wearable sensors in daily life scenarios.

Chapter 10 — Discussion

Chapter 10 provides a discussion summarizing the identified problem and presented solutions. The advantages and limitations of the proposed solutions are also reported. A brief insight into the future possible extension of the currently developed algorithms is also accounted.

Chapter 2

The Electrocardiogram

ECG signals reflect the electric activities going on in the heart muscle. These activities are the result of multiple interconnected and complex mechanical, electrical and chemical processes occurring simultaneously in heart. The ECG pattern conveys valuable diagnostic information that not only projects a continuous functioning of the heart but also other physiological functions such as blood circulation, respiration and working of the nervous system. For over 100 years the ECG signal has been a subject of interest and has improved in the understanding and quality of heart functions reflected to the sensing devices becoming more modern. The first recording of electrical activities of heart was registered in 1887 by an English physiologist August Waller who used surface electrodes placed on a skin and connected to the capillary electrometer. He was the first to name the realized signal "electrocardiogram". However, W. Einthoven is regarded as the father of electrocardiography who recorded the first ECG in 1902 using a string galvanometer. In 1906 M. Cremer recorded the first esophageal ECG with the help of a special esophageal electrode then referred to as probe [42]. Esophageal ECG was highly developed in the 1970s to be used as a technique helpful in the differentiation of atrial rhythm irregularity. Cremer recorded also the first fetal ECG. In 1924 W. Einthoven received the Nobel Prize for the invention of ECG and its development. Since then there has been a substantial research in the area of ECG. Since the 1940s, ECG has become a routine method in heart diagnostics. There has been a significant development of diagnostic techniques based on ECG analysis (say, exercise test ECG, monitoring of patients in intensive care, high resolution ECG, HRV and heart mapping).

ECG signal is one of the best-recognized biomedical signals. Its high diagnostic capabilities have been demonstrated. In the last decades there has been a significant growth of interest in the development of efficient methods of processing and analysis of ECG signals with intent of the formation of useful diagnostic information. Those pursuits have been realized in parallel with information technologies, especially in the realm of digital signal processing realized both in hardware and software.

2.1 Electrophysiological activity of the heart

Cardiac muscle is made up of two basic types of cells: 1) cardiomyocytes (generate action potentials during the phase of contraction of the heart), and dedicated cells for example bundle of His, purkinje fibers specialized in the generation and transmission of the action potentials. These specialized electrical cells depolarize spontaneously. The sinoatrial node (SA) acts as a pacemaker for the heart and has the highest spontaneous depolarization rate. In normal circumstances, the SA node generates electrical impulses that stimulate the atria to contract. The SA node is positioned in the superior wall of the right atrium, near the opening of the superior vena cava. Another important node in the heart's conduction system is the atrioventricular node (AV), located in the lower atrial septum next to the annulus of the mitral valve, and the bundle of His between the atria and the ventricles. The bundle of His splits into right and left branches at the interventricular septum membrane. The left branch of bundle of His is further divided into an anterior and posterior bundle branches. The Purkinje fibers are the last component in this conduction system interleaved with muscle tissues. The main function of Purkinje fibers is to conduct the electrical impulses directly to both left and right ventricles so that the process of contraction in both ventricles occurs concurrently. Both the Purkinje fibers and AV node have a characteristic of spontaneous depolarization producing impulses called automacity. The Purkinje fibers have an intrinsic spontaneous depolarization capability called ventricular escape rhythm generating around 30 bpm (beats per minute). The cells of the AV node also show a spontaneous depolarization and transfer impulses called junctional escape rhythm at a relatively higher rate i.e. around 40–50 bpm. In normal physiological circumstances the automaticity of the Purkinje fibers and AV node also called the rescue pacemakers is suppressed by the dominant pacemaker activity of the SA node. The electrical conduction system of the heart is shown in Figure−2.1.

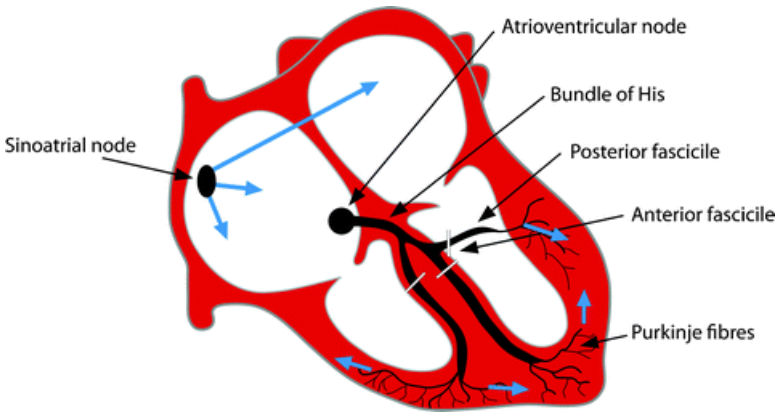

Figure 2.1: The electrical conduction system of the heart [1].

The following sections explain in detail specifically focusing on the electrical events

that occur in the heart that lead to the formation of an ECG simply explained as the "graphical representation of the cardiac electrical activity".

2.1.1 Cardiac cells

The heart's cardiac cells (myocytes) have one of two functions: mechanical (contractile) or electrical (pacemaker). The mechanical cells, also called myocardial cells, create the contractile strength of the myocardium. These contractile cells form the muscular layers of the atrial and ventricular walls and rely on the pacemaker cells to generate the impulse to contract. Pacemaker cells, also called conducting cells or automatic cells, spontaneously produce and conduct electrical impulses without stimulation by a nerve. Cardiac cells have four characteristics that make them conducive to generating and transmitting electrical impulses.

The cardiac myocardial cells interconnect and branch out mechanically through the intercalated disc and electrically through small openings or windows called the gap junctions. During its normal function, the heart constitutes two separate networked functions performed by myocardial cells: the atria and the ventricles. The atrial and ventricular tissues are separated by the central fibrous body or skeleton of the heart. This skeleton is made of dense connective tissue rings surrounding the heart valves, fuse with one another, and also merge with the interventricular septum. This fibrous tissue specifically forms the base to which the heart valves attach, prevent the valves from stretching too much, function as an insertion point for muscle bundles and most importantly act as an electrical insulator to slow down the direct spread of action potential from the atria to the ventricles.

Another property of cardiac cells is called refractoriness, which is the ability to remain unresponsive to a stimulus or to reject an impulse. The refractory period where the heart recovers before responding to additional stimuli is longer than the heart's actual contraction. The length of time for each of the refractory phases varies among individuals and is affected by medications, recreational drugs, electrolyte imbalance, disease, myocardial injury, and myocardial ischemia.

2.1.2 Resting and action potentials

A healthy myocardial cell has a resting membrane potential of approximately ≈90 mV as shown in Figure−2.2. This resting potential is mathematically explained by the Goldman-Hodgkin-Katz equation [43, 44], which uses the parameters; permeability (P) and both the intracellular and extracellular concentration of ions [X], where X is the ion.

$$V_m = \frac{RT}{F} \ln \left(\frac{P_{\mathrm{Na}}[\mathrm{Na}^+]_{\mathrm{out}} + P_{\mathrm{K}}[\mathrm{K}^+]_{\mathrm{out}} + P_{\mathrm{Cl}}[\mathrm{Cl}^-]_{\mathrm{in}}}{P_{\mathrm{Na}}[\mathrm{Na}^+]_{\mathrm{in}} + P_{\mathrm{K}}[\mathrm{K}^+]_{\mathrm{in}} + P_{\mathrm{Cl}}[\mathrm{Cl}^-]_{\mathrm{out}}} \right) \tag{2.1}$$

In the myocardial cell, the resting membrane potential is mainly due to K^+ equilibrium potential. A stimulation factor generally incoming electropositive ions

initiates an action potential and makes the resting potential of ≈90 mV less negative shifting the membrane potential towards a value of approximately ≈60 to ≈70 mV. As the membrane potential reaches this threshold, the voltage-gated sodium (Na^+) channels open. There is a rapid increase in the permeability of the plasma membrane to sodium ions (P_{Na^+}) because the intracellular fluid more electronegative than the extracellular fluid and the Na^+ concentration is higher in the extracellular fluid, Na^+ crosses the cell membrane very fast, typically within a few milliseconds. These fast Na^+ channels automatically inactivate after some time (via inactivation gates) and P_{Na^+} decreases. This 'depolarization' of membrane due to the influx of Na^+ induces the opening of the voltage-gated slow Ca^{2+} channels present within the sarcoplasmic reticulum and sarcolemma which are the storage sites for Ca^{2+}.

Now, in a normal healthy myocardial cell, concentration of intracellular K^+ is much more than extracellular K^+ and extracellular Ca^{2+} is more as compared to intracellular Ca^{2+}. Hence, an increase in the Ca^{2+} permeability ($P_{Ca^{2+}}$) rapidly increases the concentration of intracellular Ca^{2+}. Simultaneously, the K^+ channels close and the permeability of membrane to K^+ ions decreases. For almost 200 to 250 milliseconds, the membrane potential maintains a value of approximately ≈0 mV (i.e., relatively depolarized), as a small efflux of K^+ balances the influx of Ca^{2+}. After this delay where the potential is being balanced and shows no significant change also known as the plateau phase, voltage-gated K^+ channels open. When the K^+ channels open, the K^+ starts moving outward called the efflux of K^+. The opening of these K^+ channels allows for K^+ to diffuse out of the cell with increased permeability (P_{K^+}) due to its concentration gradient. At this same time, Ca^{2+} channels begin to close, and net charge movement is dominated by the outward flux of the positively charged K^+, restoring the negative resting membrane potential to approximately ≈90 mV (Figure−2.2 and this process is called 'repolarization'.

It is important to note here that the time duration is not the same for all of the above-mentioned course of actions occurring in the cardiac myocardial cell. More accurately, fast and slow responses show dissimilar shapes for changing action potentials with respect to different electrical properties in each phase. Generally there are three types of responses produced by the above-mentioned cardiac action potentials which can be differentiated by the absence or presence of instantaneous activity of the pacemaker. Non-pacemaker action potentials being the characteristic of atrial and ventricular myocytes (muscle cells) are termed as "fast response" action

Table 2.1: Typical ion concentrations for a mammalian cardiac muscle cell or myocyte.

Ion	Intracellular concentration (mM)	Extracellular concentration (mM)
Na_+	5-34	140
K_+	104-180	5.45
Ca_{2+}	10-7	3

potentials because of their rapid depolarization. Pacemaker cells typically present in the SA and AV nodes of the heart have a slower rate of depolarization for instantaneous action potentials and are termed as "slow response" action potentials. In the ventricles, the His-Purkinje system consists of myocytes specialized in conduction constitutes a third type of action potential and in contrast to normal atrial and ventricular myocytes (fast response, non-pacemaker cells), these His-Purkinje cells exhibit faster and spontaneous depolarization.

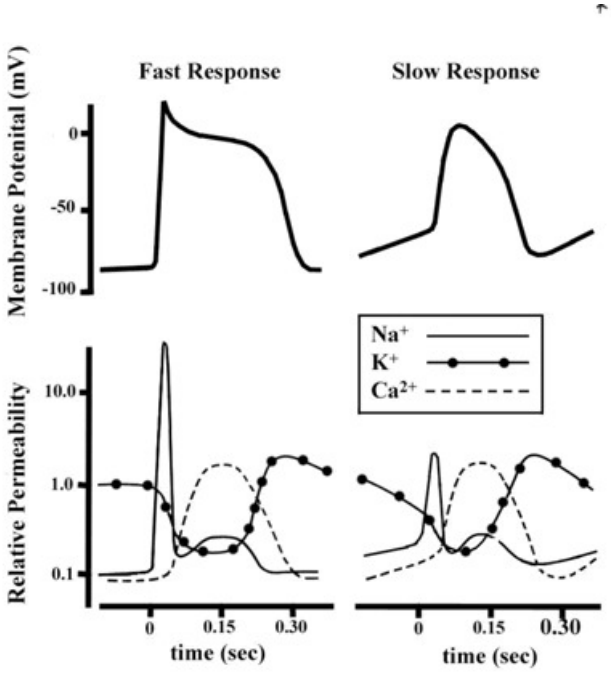

Figure 2.2: The comparative time courses of membrane potentials and ion permeabilities that would typically occur in a fast response (left panel, e.g., atrial and ventricular myocytes) and a slow response cell (right panel, e.g., nodal myocytes) [2].

Inside the heart, myocytes are end to end linked by intercalated disks. Next to the intercalated disks are small window-like openings called gap junctions. These junctions allow ion movements between cells which in turn cause the action potentials in one myocyte to directly spread to the next myocyte as shown in Figure−2.3. In a healthy heart, it takes approximately 30 msec for excitation to fan out between the SA and AV nodes, and the atrial activation takes approximately over 70 to 90 msec.

The speed at which an action or excitation potential propagates through a specific region of cardiac muscle is called relative conduction velocity. This conduction velocity varies significantly within different parts of the heart and has a direct dependency on the relative diameter of region-specific myocyte population. The conduction of action potentials is considerably slow while passing through the AV node, but is quite fast in the bundle branches that are connected through the His bundle. The slow conduction or slow movement of action potentials in the nodal tissue is due to

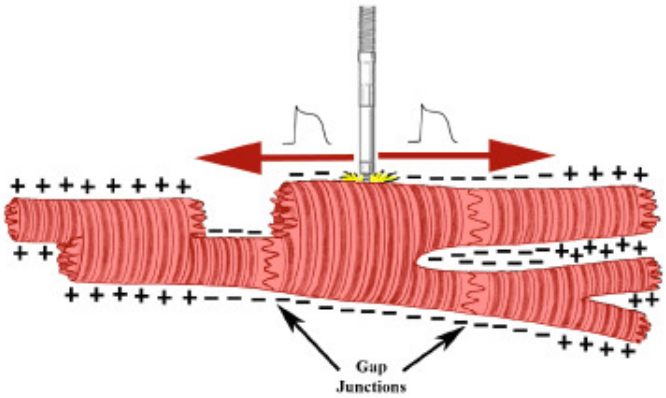

Figure 2.3: Shown are several cardiac myocytes in different states of excitation. The initial depolarization that occurred within the centrally located cell was induced via a pacemaker lead (fixated into the cell). This then resulted in the spread of depolarization of adjacent cells, in both directions, through cell-to-cell conduction via the gap junctions (nexus). Eventually all adjoining cells will depolarize. In other words, action potentials initiated in any of these cells will be conducted from cell to cell in either direction [3].

the: 1) relatively small diameter myocytes in these areas; 2) tortuosity of the cellular pathway; and 3) slower rates of rise of stimulated action potentials. Nevertheless, this delay is essential to allow appropriate time for ventricular depolarization. The next section describes how the progression of these action potentials on cellular level collectively defines the electrical activity of the heart on the organ level and then translates to an ECG pattern.

2.1.3 Electrical events during a normal cardiac cycle

As an electrical impulse leaves the SA node, it spreads across the atrial muscle and produces contraction of the right atrium, travels through the interatrial septum through Bachman's Bundle, and then enters the left atrium. This causes the right and left atria to contract at the same time. The ventricles do not contract because fibrous tissue separates the atrial and ventricular myocardium that only allows the atria to contract. This impulse doesn't flow backward, but instead only in a forward motion, because the cardiac cells are unable to respond to a stimulus immediately after the process of depolarization. The contraction of the atria is the P wave. Since the right atrium is depolarized first, this is indicated by the upswing of the P wave and the left atrium is then the down-stroke of the P wave (Contraction of the right and left atria on ECG tracing). Atrial myocardial tissue and ventricular myocardial tissue is separated by the fibrous septum. The only one point through which the current can move from atria to ventricles in a healthy heart is the AV node. Hence, the impulse travels from the SA node to the AV node. Second electrical event is the

electrical silence.

A soon as the depolarizing impulse is released into Purkinje system, ventricular depolarization starts. The ventricular depolarization occurs in three steps i.e. septal, major and basal ventricular depolarization named according to the area in ventricles being depolarized. First of all septum is depolarized, then left and right major ventricular portions are depolarized from in to out and lastly, basal area is depolarized as shown in Figure−2.4.

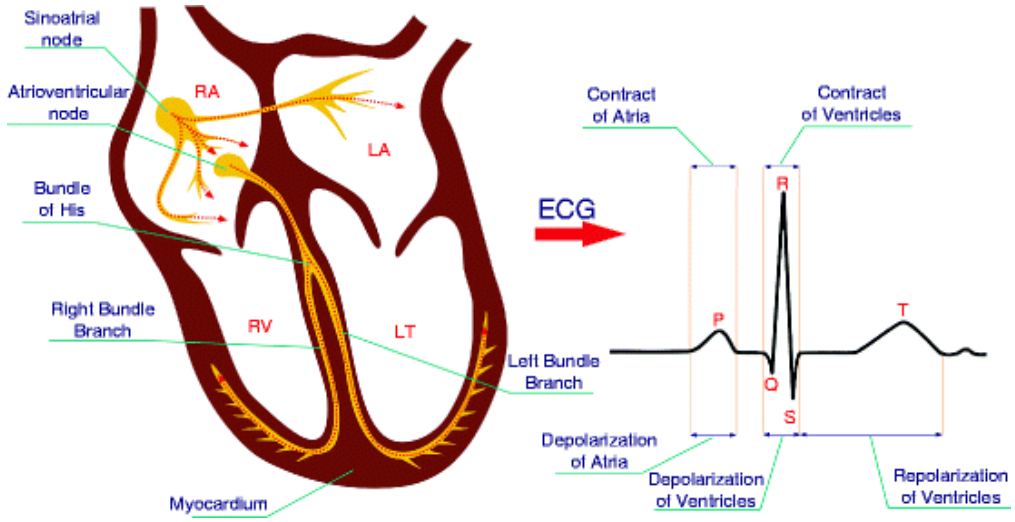

Figure 2.4: Cardiac activity during one cardiac cycle: (a) atrial depolarization, (b) ventricular depolarization, (c) ventricular repolarization, (d) septal ventricular depolarization, (e) major ventricular depolarization and (f) basal ventricular depolarization [1].

Ventricular depolarization (the QRS wave) causes ventricular systole. Atrial diastole or repolarization actually occurs at the same time that the ventricles begin their depolarization process however the strength of its signal is not as strong as the ventricular signal and therefore is "lost" within the QRS waves. The progression of the depolarization through the ventricles begins at the Q wave and continues through to the beginning of the T wave. The mass of the contraction essentially takes place at the end of the QRS during the plateau phase depicted on the EKG as the ST segment. Cardiac cells respond differently than skeletal muscle to stimuli. Skeletal muscles react with a short twinge type response, whereas, cardiac cells act with a longer, sustained type of contraction due to the necessity of pumping blood through the heart chambers. Repolarization of the ventricles, ventricular diastole, is identified on the ECG recording as the T wave.

2.2 Basic ECG features

The successive step of ECG signal analysis is a formation of a feature space that is a collection of descriptors that fully capture the essence of the signal. More precisely,

we are interested in the features that exhibit high discriminatory power, which is of importance to any classification of ECG signals and their interpretation. Those features are mostly present in a time domain; however they could be defined in the frequency domain. It is also possible to extract features of a different nature, which relate with some unconventional features such as those exploiting methods of data approximation, data segmentation, and information granulation. Of paramount importance are the features exhibiting some diagnostic properties. As examples, we can recall here, see Figure−2.4,

- Time intervals between consecutive R points
- Distance PQ, PR, QT
- Amplitudes of P, Q, R, S, T
- Duration of P, R, and T waves
- A location of the center of the ST interval
- A slope of the ST interval.

These features, being so-called primitive features are determined directly from the ECG signal. For diagnostic purposes extracted are also some other features, called derivative features which are constructed based on the primitive ones. For instance:

- Shift of the QRS complex versus baseline – known as offset
- Areas of waves of P, R, and T
- Position of the heart axis
- Corrected distance Qt denoted also as Qt_c, which is determined following the Bazett Equation−(2.2):

$$Qt_c = \frac{Qt}{\sqrt{RR}} \tag{2.2}$$

  where RR stands for a distance between successive R waves.

- A ratio of successive intervals RR_i described as in Equation−(2.3):

$$\partial R = \frac{RR_i}{RR_{i+1}} \tag{2.3}$$

The features of the ECG signal constructed on a basis of a shape of the signal, segments of the signal that repeat in a cyclic fashion that cover a single heart evolution, namely a P-QRS-T complex. Once classified, these complexes along with other parameters of the ECG signal form a basis for further analysis and interpretation.

2.3 Types of noise

Given the nature of ECG with respect to the body function they measure and the mode of acquisition (electrodes or probes) of the recording, there are a number of challenges encountered during their acquisition, processing, and further investigation for multiple purposes. Inherently biomedical signals have typical characteristics such as nonstationarity, noise susceptibility, and variability over time and among different individuals. ECG exhibits all these characteristic properties too. In particular, a highly undesirable aspect of ECG is its high susceptibility to various types of noise inducing phenomenon. The ECG signal in its raw acquired form is always corrupted by some type and amount of noise. The main sources of noise include:

2.3.1 Baseline wander

Baseline Wander is a low-frequency noise having non-linear and non-stationary nature. Baseline wander is a low-frequency noise of around 0.5 to 0.6 Hz. To remove it, a high-pass filter of cut-off frequency 0.5 to 0.6 Hz can be used. The classical methods such as high-pass filtering cannot provide full separation of the signal from low-frequency noise. Baseline wander or baseline drift is the effect where the base axis (x-axis) of a signal appears to 'wander' or move up and down rather than be straight. This causes the entire signal to shift from its normal base. In ECG signal, the baseline wander is caused due to improper electrodes (electrode-skin impedance), patient's movement and breathing (respiration). The frequency content of the baseline wander is in the range of 0.5 Hz. However, increased movement of the body during exercise or stress test increase the frequency content of baseline wander. Since the baseline signal is a low frequency signal therefore Finite Impulse Response (FIR) high-pass zero phase forward-backward filtering with a cut-off frequency of 0.5 Hz to estimate and remove the baseline in the ECG signal can be used [45].

2.3.2 Powerline interference

Powerline interference (PI) are induced by the electromagnetic field generated by power supplied to the measurement system or generated by other medical devices present nearby [46, 47]. The frequency spectrum of the PIs is relatively narrow and centered around the frequency of AC power supply. This noise is relatively easy to filter. For this purpose the band restrictive filters are used with narrow frequency characteristics; the filters could be analog but mostly used are digital. The spectrum of this noise overlaps to a limited extent of the ECG frequencies, meaning that the required methods of noise filtering do not distort the original signal. An efficient way to suppress power noise is to construct registration devices in such a way so that proper shielding and noise elimination is provided. Among the electromagnetic noise we can distinguish noise caused by the power supplies where the amplitude of voltage and current changes with frequency of 50 or 60 Hz. In this case, we are talking

about typical power supply type of noise. The power supply could be a source of sporadic impulse-like noise. It is often caused by turning on high-power devices such as diathermy equipment, CT devices etc. [48, 49].

2.3.3 Electrode motion artifact

Low-frequency noise also called electrode motion artifact is a result of changes in impedance between the electrode and a body surface of the patient. The impedance alters as a result of change in the distance between the source (i.e. heart) and the electrode caused by the movement of the patient including chest movements due to breathing and changes of contact between the body and the electrode, which to a significant extent is caused by the movement of the body of the patient. The low frequency noise is located in the frequency spectrum below 1 Hz. However, in some types of testing scenarios, for example exercise examination of ECG [48, 50] this low-frequency noise includes a far high range of frequencies including and can include components reaching several Hz. In exercise ECG test, the amplitude of low frequency noise also becomes higher demanding the use of more effective techniques for noise cancellation. Similar is the case for wearable ECG systems (i.e. Holter, patch-based, belt-based and wrist-based ECG wearable devices) which are targeted to be used for long-term acquisition and monitoring of ECG signals.

2.3.4 Body movement or muscle artifact

The main cause of muscle noise in ECG is the electrical signals produced during contraction of skeletal muscles, which occur due to the physical movement of the patient or an inapt ambient temperature of the environment and time in which the ECG examination is being carried out. This causes so-called muscle disturbances. Muscle electrical signals are always related with ECG signals. The highest amount of muscle noise is observed in stress tests. In exercise conditions, the noise is caused by intensive muscle contractions during running on a treadmill or the load of the patient caused by cycloergometer. The movement of the patient is present during a long-term recording of ECG signals under normal conditions (dominantly present in wearable Holter, patch-based, belt-based and wrist-based ECG testing). In this case, the level of muscle noise depends quite significantly on a level of activity (movement) of the patient, which could vary within the testing. Muscle noise becomes present in rest tests caused by involuntary contractions of skeletal muscle resulting from the ambient temperature, which could be too low or too high. This phenomenon is particularly undesirable in case of registering microvolt heart potentials, that is micropotentials recorded on the surface of the body, in the esophagus or in the heart ventricles. The main problem arises here because of the overlap of the spectrum of the signal and noise to a significant extent. The spectrum of the signal forms a range of 0.005–150 Hz whereas the noise spectrum covers the range of frequencies from 20 to 80 Hz. They are very difficult to deal with because of the broad spectrum

of frequency of these disturbances, whose frequency overlaps with the frequency of the ECG signal itself [49]. The attempts to filter muscle noise lead to significant distortions of the ECG signal. With the increase of the effectiveness of the muscle noise, the resulting distortions of the signal may result in incorrect classification results produced by medical doctors as well as computerized systems.

2.4 Types of specialized ECG tests

In case of the specialized ECG tests we can offer a classification depending upon a leading ECG parameter, which is subject to analysis in order to detect some irregularities in heart functioning. In this case we identify the following categories of tests:

- Heart micropotentials analysis ˘ high resolution electrocardiography,
- Sinus rhythm variability analysis ˘ HRV analysis,
- Heart rhythm disturbances analysis ˘ arrhythmia analysis,
- Baroreflex examination ˘ BRS (Baroreflex Sensitivity),
- Repolarization analysis ˘ analysis of QT segment duration and dispersion,
- Microvolt T wave variability analysis ˘ alternation of T wave (T-wave afternans TWA).

The specialized ECG tests come with their own specificity which means that the diagnostic information is conveyed in quite limited changes of parameters, either specified in time or frequency domain. The detection of changes in these parameters in a noisy ECG signal becomes a difficult task. Practically, its direct identification realized by a cardiologist is impossible; it can be done based on the registered ECG signal. The required diagnostic information in case of such specialized ECG tests is obtained through running advanced algorithms. In particular, this concerns problems dealing with noise suppression and a precise determination of the basis points.

2.5 Arrhythmia analysis

The objective of the ECG testing is an identification of heart dysfunctions and an identification of their causes. The essence of these testing relies on the assessment of the functioning of the heart. During such testing carried out is an analysis of the changes of some essential cardiac parameters of diagnostic nature. The most generic is the analysis of the heart rhythm disturbances. The rhythm disturbances are associated with abnormalities of action of the stimuli generation system of the heart or with abnormal conduction of these stimuli. In the first case, there are the

heart rhythm disturbances, and in the second one we are concerned with the heart conduction disturbances. [51, 52].

These abnormalities can be classified as follows:

- Irregular rhythms,
- Substitute rhythms,
- Premature stimulations,
- Tachyarhytmies.

These deviations in the conductance of electrical impulses in the heart muscle manifest in so-called heart blocks [53] which block conductance of a depolarization wave. These blocks could concern sinus node, atrioventricular, or main branches of the electrical conduction system of the ventricles. Here we distinguish the following main categories of conduction disturbance [51]:

- Sinus blocks,
- Atrio blocks,
- His bundle branch blocks,
- Hemiblocks (infarct blocks).

In this analysis, an important role is played by the changes in the HRV [54, 55]. Here one analyzes the changes of the time intervals between successive R waves (RR interval). During normal human activities, the length of distances RR varies. The rhythm frequency and the variability of changes in successive heart evolution to a significant extent is reflective of the influence of the autonomic system on electrical activity of the sinus node. The quantitative assessment of the heart rhythm variability is an indirect indicator of the activity of the autonomic system. In recent years one can note an increasing interest in the development of methods of analysis of heart rhythm disturbances [55, 56, 57].

In the next sections, we discuss some specific heart abnormalities that particularly concern the work of this thesis. Ventricular premature contraction, supraventricular, left bundle branch block, right bundle branch block, atrial premature contraction, ventricular escape, ventricular flutter and paced heartbeats.

2.5.1 Premature ventricular contraction

A premature ventricular contraction (PVC) is a relatively common event where the heartbeat is initiated by Purkinje fibers in the ventricles rather than by the sinoatrial node. PVCs may cause no symptoms or may be perceived as a "skipped beat" or felt as palpitations in the chest. A premature ventricular contraction (PVC) is caused by

an ectopic cardiac pacemaker located in the ventricle. PVCs are characterized by premature and bizarrely shaped QRS complexes that are unusually long (typically >120 msec) and appear wide on the electrocardiogram (ECG). These complexes are not preceded by a P wave, and the T wave is usually large and oriented in a direction opposite the major deflection of the QRS.

2.5.2 Supraventricular tachycardia

Supraventricular tachycardia (SVT) is an abnormally fast heart rhythm arising from improper electrical activity in the upper part of the heart. There are four main types: atrial fibrillation, paroxysmal supraventricular tachycardia (PSVT), atrial flutter, and Wolff–Parkinson–White syndrome. They start from either the atria or AV node. They are generally due to one of two mechanisms: re-entry or increased automaticity.

2.5.3 Left bundle branch block

In the case of left bundle branch block (LBBB) condition, activation of the left ventricle of the heart is delayed, which causes the left ventricle to contract later than the right ventricle. The heart rhythm in case of LBBB is supraventricular in origin. The criteria to diagnose a left bundle branch block on the ECG: The QRS duration must be ≥120 ms. There should be a QS or rS complex in lead V1. There should be a notched ('M'-shaped) R wave in lead V6. The T wave should be deflected opposite the terminal deflection of the QRS complex. This is known as appropriate T wave discordance with bundle branch block.

2.5.4 Right bundle branch block

A right bundle branch block (RBBB) represents is a heart block in the right bundle branch of the electrical conduction system. During a right bundle branch block, the right ventricle is not directly activated by impulses travelling through the right bundle branch. The left ventricle however, is still normally activated by the left bundle branch. These impulses are then able to travel through the myocardium of the left ventricle to the right ventricle and depolarize the right ventricle this way. As conduction through the myocardium is slower than conduction through the Bundle of His-Purkinje fibres, the QRS complex is seen to be widened. The QRS complex often shows an extra deflection that reflects the rapid depolarisation of the left ventricle followed by the slower depolarisation of the right ventricle. The criteria to diagnose a right bundle branch block on the electrocardiogram: The heart rhythm must originate above the ventricles (i.e., sinoatrial node, atria or atrioventricular node) to activate the conduction system at the correct point. The QRS duration must be more than 100 ms (incomplete block) or more than 120 ms (complete block). There should be a terminal R wave in lead V1 (often called "R prime," and denoted by R, rR', rsR', rSR', or qR). There must be a prolonged S wave in leads I and

V6 (sometimes referred to as a "slurred" S wave). The T wave should be deflected opposite the terminal deflection of the QRS complex. This is known as appropriate T wave discordance with bundle branch block.

2.5.5 Premature atrial contraction

Premature atrial contractions (PACs), also known as atrial premature complexes (APC) or atrial premature beats (APB), are a common cardiac dysrhythmia characterized by premature heartbeats originating in the atria. While the sinoatrial node typically regulates the heartbeat during normal sinus rhythm, PACs occur when another region of the atria depolarizes before the sinoatrial node and thus triggers a premature heartbeat. PACs are often completely asymptomatic and may be noted only with Holter monitoring, but occasionally they can be perceived as a skipped beat or a jolt in the chest. On an ECG, PACs are characterized by an abnormally shaped P wave. Since the premature beat initiates outside the sinoatrial node, the associated P wave appears different from those seen in normal sinus rhythm. Typically, the atrial impulse propagates normally through the atrioventricular node and into the cardiac ventricles, resulting in a normal, narrow QRS complex. However, if the atrial beat is premature enough, it may reach the atrioventricular node during its refractory period, in which case it will not be conducted to the ventricle and there will be no QRS complex following the P wave.

2.5.6 Ventricular escape

An escape beat can be considered a form of ectopic pacemaker activity that is unveiled by lack of other pacemakers to stimulate the ventricles. Ventricular escape beats occur when the rate of electrical impulse reaching the ventricles falls below the base rate of SA (approximately 70 bpm on average) or AV (approximately 40–60 bpm) node determined by the rate of spontaneous depolarisation of ventricular pacemaker cells.Ventricular contraction rate is thus reduced by 15–40 beats per minute. An escape beat usually occurs 2-–3 seconds after an electrical impulse has failed to reach the ventricles. On the ECG waveform, the QRS portion of the electrocardiogram is broader as the impulse cannot travel quickly via the normal electrical conduction system. Ventricular escape beats differ from ventricular extrasystoles (or premature ventricular contractions), which are spontaneous electrical discharges of the ventricles. These are not preceded by a pause; on the contrary they are often followed by a compensatory pause.

2.5.7 Ventricular flutter

Ventricular flutter is an arrhythmia, more specifically a tachycardia affecting the ventricles with a rate over 250-350 bpm, and one of the most indiscernible. It is characterized on the ECG by a sinusoidal waveform without clear definition of the

QRS and T waves. It has been considered as a possible transition stage between ventricular tachycardia and fibrillation, and is a critically unstable arrhythmia that can result in sudden cardiac death.

2.5.8 Paced

A pacemaker is indicated when electrical impulse conduction or formation is dangerously disturbed. The pacemaker rhythm can easily be recognized on the ECG. It shows pacemaker spikes: vertical signals that represent the electrical activity of the pacemaker. These vertical spikes are of short duration, usually 2 ms. Specifically in atrial pacing, the spike precedes the p wave and in ventricular pacing the spike precedes the QRS complex. Also in ventricular pacing, ST segments and T waves are discordant with the QRS complex i.e. the major terminal portion of the QRS complex is located on the opposite side of the baseline from the ST segment and T wave. Bipolar leads result in a much smaller amplitude pacing spike than unipolar leads.

Chapter 3

Segmented Beat Modulation Method

SBMM [58, 4] was proposed in 2014 as a template-based filtering technique to clean noisy ECG signals (SBMM algorithm has also been patented in 2014). Template-based techniques usually do not reproduce beat-to-beat heart-rate variability. Instead SBMM, thanks to its modulation procedure that prolongs the template for short beats and shortens the template for long beats, is able to adjust for heart-rate variability. SBMM has been tested for robustness and ability to extract clean ECG signal [39] from recordings affected by low, medium and high levels of noise of various kinds. The following sections present a detailed current account of SBMM technique along with a study conducted on the algorithm robustness in the presence of noise. SBMM has been successfully applied in multiple application areas, i.e. 1) Fetal electrocardiography, 2) Surface electromyography and 3) ECG derived respiration signal extraction [6, 40, 41]. In these applications, some variations of the algorithm have been performed to adapt it to the specific problem. Section 1.4 identifies some limitations of SBMM to improve the applicability of the algorithm.

3.1 Methodology

The basic flowchart of SBMM along with a standard template method (STM) is depicted in Figure−3.2. The algorithm is based on the practical observation that, in first approximation, the QRS complex duration is independent of the instantaneous HR, whereas the duration of all other ECG waves linearly varies with it [59]. Specifically, the QRS duration is independent of the preceding RR interval, but the duration of the other waves is proportional to it. Under this assumption, each CC can be divided into two segments, the QRS and the TUP as shown in Figure−3.1. The QRS segment is identified $\pm\Delta$t ms around the R-peak, while the TUP segment is identified within Δt ms after the R-peak and Δt ms before the subsequent R-peak. Each CC is characterized by its own amplitude and duration. However, the duration of all QRS segments is the same in all CCs (twice Δt), whereas the duration of the TUP segments is CC-dependent (difference between CC duration and QRS duration).

According to SBMM procedure, the R-peak sequence containing the location of the R-peaks within the noisy ECG is used to identify all CCs and to compute the median RR interval (mRR). Before computing mCC, all CCs are modulated in order

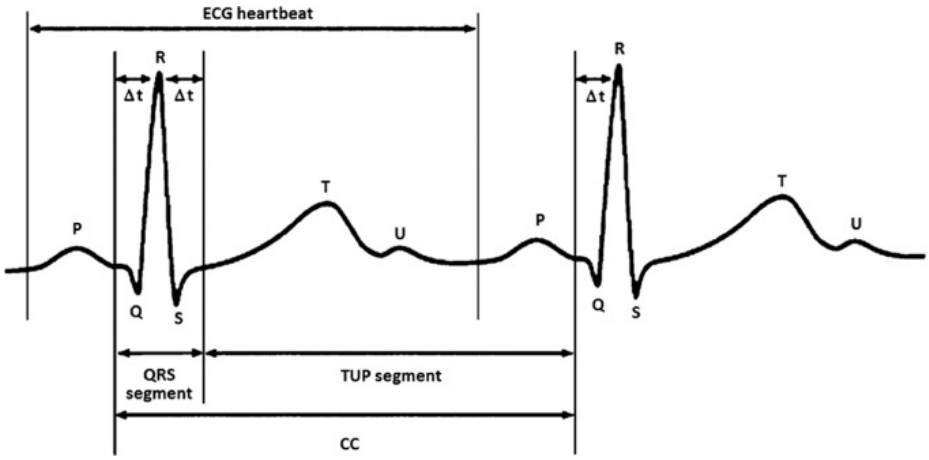

Figure 3.1: CC segmentation rules for SBMM [4].

to have their length equal to mRR. However, since the QRS segments are supposed to have constant duration, the modulation process interests only the TUP segments and is performed by linear stretching or compression. Eventually, the modulated mCC is obtained as the median of all CCs reconstructed using the original QRS segments and the modulated TUP segments. The modulated mCC provides a clean template of all CC in the noisy ECG. Before concatenating N modulated mCCs to get the clean ECG at the output of SBMM procedure, the TUP segment of mCC is demodulated (by compression or stretching) to have its duration equal to the TUP-segment duration of the corresponding CC in the noisy ECG; then CCs are reconstructed and optimization processes, involving cross-correlation maximization and distance minimization between reconstructed and original CCs, are performed in order to compensate for possible small inter-beat, nonlinear HR variations of the CC waveforms.

3.1.1 Validation study

To check the correctness of the STM and SBMM algorithms, a simulation study was performed assuming ideal conditions i.e. input ECG recordings not affected by noise. For this purpose Matlab ECG signal generator was used generate 6 ECG recordings each of 60 s duration characterized by a median HR of 75 bpm; median CC (mRR) duration was set to 800 ms. The amplitudes different ECG characteristic waves were set as: P: 0.20 mV; Q: 0.15 mV; R: 1.6 mV; S: 0.25 mV; and T: 0.40 mV. For each beat the latter values were linearly varied proportionally to the previous RR interval. Since this simulation study assumes an ideal no noise condition and a linear HRV both of which are not reflective of real signals, another clinical study was conducted using real ECG recordings affected by multiple types and levels of noise factors. For this purpose, 18 two-lead ECG recordings acquired using Holter monitor from healthy subjects displaying no significant arrhythmic conditions ere taken from the "MIT–BIH Normal Sinus Rhythm Database" on the Physionet (www.physionet.org)

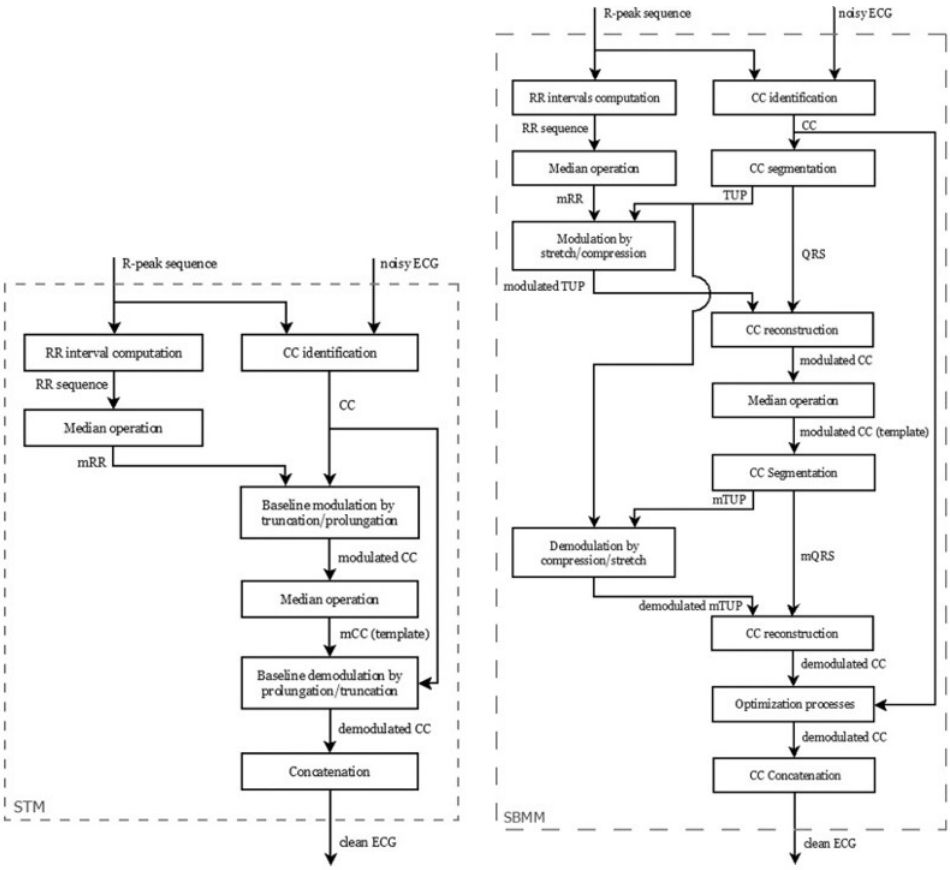

Figure 3.2: Flowchart of the STM (left panel), and SBMM (right panel) [4].

[60]. All ECG recordings were characterized by a HR ranging from 63 bpm to 110 bmp, and by a HRV (measured as RR-interval standard deviation) ranging from 15 ms to 78 ms. The initial noise necessarily present in the input ECGs was minimized by pre-filtering (0.5–35 Hz band-pass filtering and baseline estimation and removal by a 3^{rd}-order spline interpolation). Then, three real noise recordings containing BW, EMA and MA from the Physionet "MIT–BIH Noise Stress Test Database" [61, 60] and one sinusoidal signal with frequency of 50 Hz mimicking PI were added to each input pre-filtered ECG recording. Low to high levels of noise were reflected by multiplying each noise recording with a gain ranging from 0 (no noise) to 1 with increasing intervals of 0.25. Strength of SBMM in comparison to STM to provide a noise-free ECG estimated from an input noisy recording was evaluated by comparing estimated ECGs with input reference ECGs (i.e. simulated ECGs for the simulation study and pre-filtered real ECGs for the clinical study). Although STM does not include CC segmentation in QRS and TUP segments in its algorithm, such segmentation was performed for both methods in order to make their comparison possible. For each ECG lead two different errors were evaluated, namely ϵQRS and ϵTUP, respectively relative to the QRS segment and the TUP segment representing the error values between input and output corresponding ECG signal points.

3.1.2 Results and Discussion

Both SBMM and STM are template-based methods, which rely on the construction of the template-beat to be concatenated to obtain the clean estimated ECG. If BW, EMA, MA and PI can be considered independent noises because they are generated by independent sources (also confirmed by computation of correlations which came out to be very close to zero), they may not be perfectly zero-mean in the time window of the analyzed ECG recording. To compensate for that, both STM and SBMM have been designed here not to perform a coherent averaging [62] computation but, rather, a coherent median computation (coherent average and coherent median converge in the presence of perfectly zero-mean interferences). Different from STM and any other template-based technique, SBMM requires the segmentation of each CC into two segments, the QRS segment and the TUP segment, which are supposed to be respectively independent and proportional to the preceding RR interval [59].

The distinctive modulation and demodulation actions executed by compressing and stretching the segmented TUP part of the CC allows the adaptation or update of each CC estimate by SBMM to its original duration, and makes SBMM robust to HRV, which is a unique capability of SBMM compared to other template-based ECG denoising methods. To validate the goodness of SBMM in estimating clean ECG recordings, input tracings affected by HRV and/or noise were tested and compared to that of STM in simulated as well as clinical settings. In simulated tracings characterized by various levels of HRV, duration of QRS segment was fixed, while duration of TUP segment was linearly varied with the preceding RR interval (i.e. instantaneous HR). Both SBMM and STM produced QRS segment estimates perfectly. However, TUP segments were estimated with no errors by SBMM, and with errors directly proportional to HRV by STM. Although the simulation study demonstrates superiority of SBMM with respect to other template-based techniques in estimating ECG affected by HRV, its optimal performance is due to the fact that simulated data were ideal, that is characterized by a TUP segment linearly varying with instant HR and not affected by noise.

Secondly, the input ECGs were corrupted with multiple levels of noise (no noise to high) were added to the prefiltered tracings before submitting them to SBMM and STM specifically BW, EMA, MA and PI. Results relative to clean ECG estimation from clinical recordings with no added noise show that, differently from that obtained for the simulation study, QRS and TUP errors were always greater than zero. This mainly occurred for two reasons: although prefiltered, clinical ECGs are never perfectly clean; and linear dependency of TUP-segment duration on instant HR is only a first-order approximation of a physiologic relationship, which may also be characterized by higher−order components and other kinds of dependencies. Results also indicate that TUP errors tend to increase with HRV even though such dependency is stronger when computed using STM than SBMM thanks to the modulation/demodulation process performed by stretching/compression characterizing

the latter method. In the presence of noise, estimation of both the QRS segment and the TUP segment by SBMM was usually superior to that by STM for all noise types and levels. Indeed, SBMM not only includes the unique HRV regulation method for the TUP segments, but also performs some optimization procedure that are not included in STM. Also observed and reported in the study, estimation errors in the QRS segment by both methods were usually greater than those relative to the TUP segment, since waveforms included in the QRS segment are characterized by comparatively a high amplitude and frequency components than those in the TUP segment. The results obtained in the presence of noise show that the use of median for the template computation allows for a good reduction of all kinds of noise, even though a not exactly zero-mean. However it is to be noted that template-based techniques, including STM and SBMM, can be applied only if the R-peak positions are known. In most clinical cases in which they are used, this condition is easily satisfied. In the common cases in which the QRS-complex amplitude is higher than noise (good SNR), specifically designed algorithms can be applied to localize the R peaks (such as the popular Pan-Tompkins's technique [63]). In contrast to the other template-based techniques, SBMM provides better clean ECG estimation from noisy recordings, being also able to reproduce physiological ECG variability. These improvements are due to ECG segmentation into QRS segments and TUP segments, and successive modulation/demodulation processes (involving stretching and compression) of the former segments, which are performed in order to adaptively adjust each estimate beat to the original beat morphology and duration.

3.2 Applications

3.2.1 Separation of fetal and maternal ECG

The fetal ECG (FECG) reflects the electrophysiological activity of the fetal heart. Using FECG waveform analysis, abnormalities during fetal development, such as fetal distress and intrauterine hypoxia, can be diagnosed. Currently, there are two ways to obtain a FECG. One is the direct: invasive scalp electrode method, which can directly measure the pure FECG signal by placing the electrode on fetus's head as shown in Figure−3.3 (panel a). However, it can only detect FECG signal during birth, and because it is invasive it may cause harm to the mother and the fetus. Another method is the indirect: non-invasive abdominal electrode method as shown in Figure−3.3 (panel b) in which signals from the abdominal body surface are collected by placing an electrode patch in the abdomen of the mother, which allows for long-term monitoring during pregnancy. However, the signals from the maternal abdominal surface are very complex, containing not only maternal ECG (MECG) and weak FECG signals, but also the mother's respiratory noise, frequency interference, and other signals [64, 65]. In particular, the magnitude of the MECG detected in the abdomen is about 2–10 times that of the FECG [66], which makes the extraction of the FECG difficult. Therefore, it is necessary to develop a non-invasive method that can extract the FECG effectively.

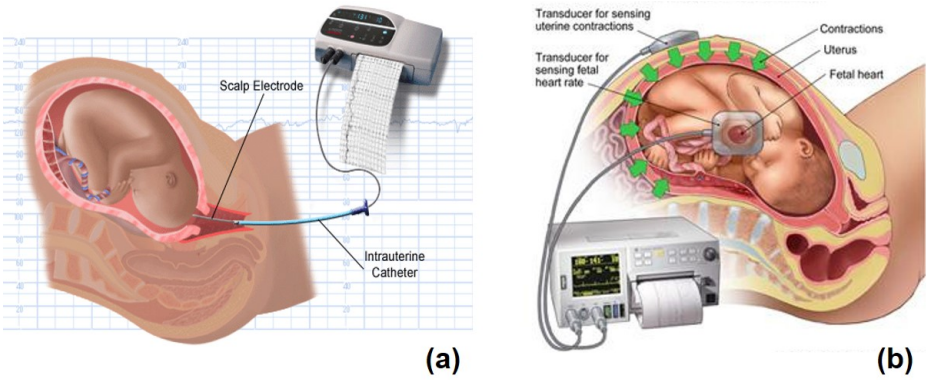

Figure 3.3: FECG acquisition modalities, direct (left panel) and indirect or abdominal (right panel). Figure reused from [5].

This study evaluated SBMM suitability to denoise indirect abdominable ECG recordings (IREC) in order to obtain an indirect FECG (IFECG) characterized by a signal quality at least comparable to that of direct FECG (DFECG), the latter being considered as the gold standard for FECG. Given the acquisition modalities, direct recording (DREC) is substantially a noisy version of DFECG, whereas IREC, besides IFECG, also contains maternal electrocardiogram (MECG) and other noises. Noise affecting DREC and IREC is a mixture of interferences that can or cannot have a physiological origin. It can be decomposed in low-frequency noise, high-

frequency noise and in-band noise. The low (<0.5 Hz) and high (>45 Hz) frequency components do not contain any significant amount of ECG (both FECG and MECG) easily removed by linear filtering. The in-band noise has frequency components that overlap to the ECG ones (i.e. $0.5 - 45$ Hz). As a result, DREC and IREC can be mathematically modeled as follows:

$$DREC = DFECG + DN \tag{3.1}$$

$$IREC = IFECG + MECG + IN \tag{3.2}$$

where DN and IN are the in-band noise components affecting DREC and IREC, respectively. DFECG and IFECG were extracted from DREC and IREC, respectively, by application of SBMM. Reference fetal R-peak positions and DREC were submitted to SBMM, which provides DFECG as output. DN was obtained by subtracting DFECG from DREC as hown in Figure−3.4 (left panel).

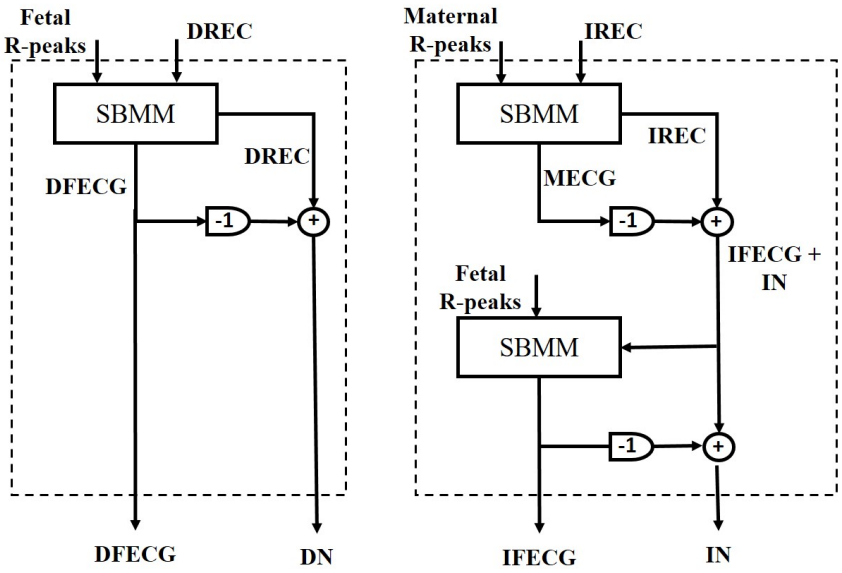

Figure 3.4: Block diagram of the procedure to extract DFECG and IFECG from DREC (left panel) and from a single channel of IREC (right panel), respectively, by means of SBMM [6]

SBMM was also used to extract an IFECG signal from each IREC channel (Figure−3.4 (right panel), panel b). Being MECG the highest amplitude component in IREC, maternal R peaks were obtained by applying the Pan-Tompkins algorithm [63] to IREC. Then, maternal R-peak positions and IREC were submitted to SBMM in order to get MECG. Successively, MECG was subtracted from IREC to obtain a noisy version of IFECG (IFECG+IN) which, together with fetal R-peak positions (which were the same used for DFECG extraction), was submitted to SBMM. Eventually, SBMM provided IFECG as output, whereas IN was obtained by subtraction. The

validation data consisted of 5 records 60 s long (sampling rate: 1000 Hz) from 5 different pregnant women during labor, which occurred within the 38th-41st week of gestation acquired by means of the KOMPOREL system. Each record was constituted by a direct recording (DREC) and a 4-channel indirect recording (IREC) simultaneously acquired. DREC was carried out with a spiral electrode on the fetal head; instead, IREC was obtained by placing 4 electrodes around the navel, a reference electrode above the pubic symphysis and a common mode reference electrode (with active-ground signal) on the left leg. All recordings are part of the "Abdominal and Direct Fetal Electrocardiogram Database" [67] of PhysioNet (www.physionet.org) [60]. Reference R-peak positions are also available with the database. SNR was used to relatively quantify the level of noise affecting a signal, in our case DFECG and IFECG, respectively affected by DN and IN. Direct SNR (DSNR) and indirect SNR (ISNR) were obtained as Equation−3.3 and Equation−3.4 respectively as:

$$DSNR = 10log_{10}\frac{DFECG\ amplitude}{DN\ amplitude} \tag{3.3}$$

$$ISNR = 10log_{10}\frac{IFECG\ amplitude}{IN\ amplitude} \tag{3.4}$$

DFECG and IFECG are pseudo-periodic signals, their amplitudes were computed as mean of the maximum-minus-minimum values over the beats. Instead, being DN and IN close to Gaussian stochastic signals, their amplitudes were computed as 4 times standard deviation [68, 40]. All amplitude values were computed over the entire length of the study records (60 s). ISNR was computed twice, once after MECG subtraction from DREC (ISNR1) and one after IFECG denoising (ISNR2). Thus, ISNR2 actually describes the quality of the final IFECG tracing obtained from DREC using the SBMM. Association between DFECG and IFECG (which represent the same electrophysiologic phenomenon, i.e. electrical activity of the fetal heart) was evaluated using the Pearson's correlation coefficient (ρ).

SBMM application to record 1 is depicted in Figure−3.5, where simultaneously acquired DREC and IREC (channel 1) are represented together with all their components. Generalizing, for all records DFECG was always characterized by amplitude higher than that characterizing IFECG (104 [89;157] μV) vs. 22 [16, 28] μV, P=$7.66{\cdot}10^{-4}$), independently of the channel. Median DSNR was significantly greater than median ISNR1. At the end of SBMM processing, however, the noise level affecting IFECG was mostly removed so that median DSNR was significantly lower than median ISNR2. Correlation between DFECG and IFECG was found to be typically high and significant (ρ=0.78 [0.75;0.83], P<10^{-208}) indicating that both signals consist of equivalent morphological content which in-turn shows the goodness of SBMM performance in extracting DFECG and IFECG from the clinically acquired noisy DREC and IREC signals. In addition, at the end of the SBMM procedure, ISNR2 was lower than DSNR, indicating that extracted IFECG was characterized by

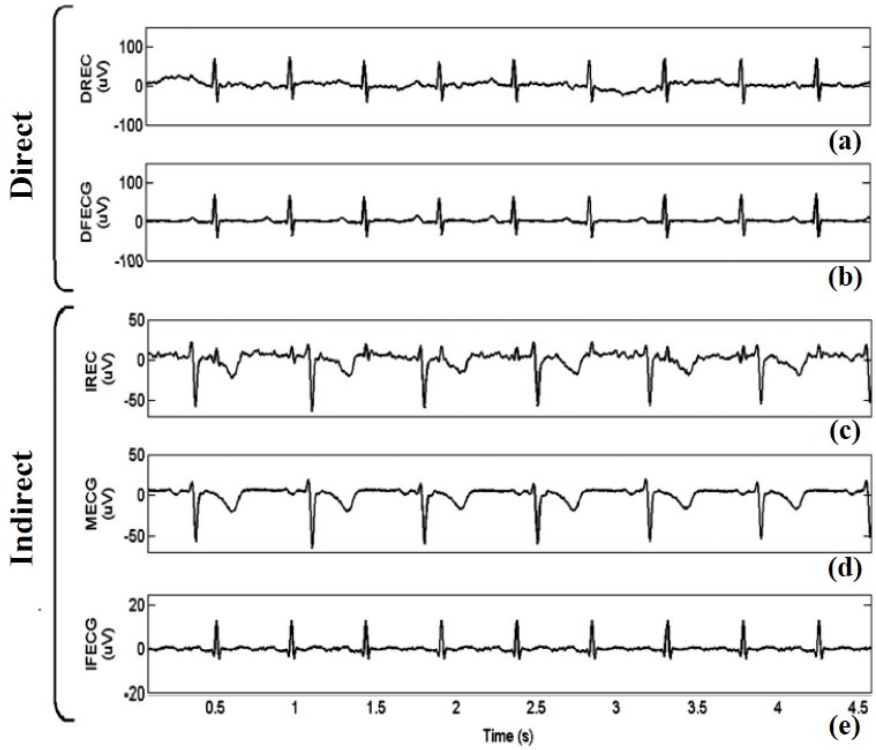

Figure 3.5: Representative 4.5 s of simultaneously acquired DREC and IREC (channel 1), together with all their components individually plotted (DFECG amplitude: 104 μV; and IFECG amplitude: 18 μV).

a better signal quality than DFECG. The finding that ISNR2 was higher than DSNR indicated that IFECG, extracted using SBMM, has better quality than DFECG. Thus, SBMM can be used to obtain clean, potentially clinically useful IFECG also when DFECG is not available.

IFECG estimation by SBMM is obtained after MECG estimation and subtraction from IREC. Without the modulation/demodulation procedure, MECG is represents an ECG signal with fixed HR, hence some misalignments may occur in the repolarization TUP segment non-representative of actual physiological conditions, and causing significant morphological disruptions in the resulting IFECG signal obtained by subtraction as shown in Figure−3.6 (panel a). Inclusion of the modulation/demodulation procedure tracks the maternal repolarization variability and adapts the final reconstructed IFECG to it. This process reduces the artefacts strongly as shown in Figure−3.6 (panel b). Conclusively, when SBMM is applied for filtering fetal tracings (direct or indirect) from noise, it performs better than the other template-based techniques, since it is the only one able to track variations in fetal repolarization variability.

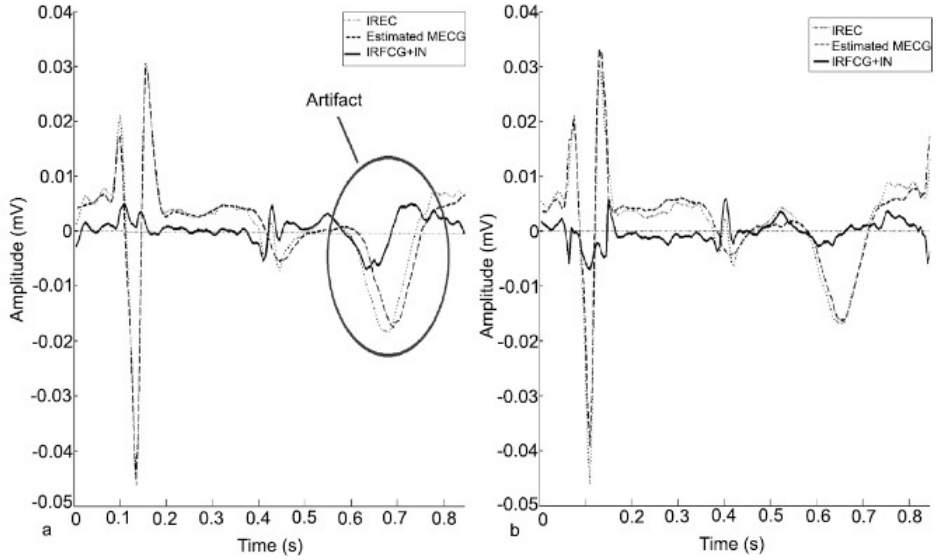

Figure 3.6: Example of a beat of the IFECG + IN (solid line) overlapped to estimated MECG (bold dotted line) and IREC (dotted line) obtained without (panel a) and with (panel b) the modulation/demodulation process [6]

3.2.2 Surface electromyography

Surface electromyography (SEMG) is a noninvasive technique used to measure the electrical activity of muscles during activation. SEMG differs from the standard needle electromyography (NEMG) and fine-wire electromyography (FWEMG) with respect to technical requirements and electrical properties. Unlike NEMG and FWEMG, SEMG electrodes record from a wide area of muscle territory, have a comparatively narrow frequency range (20-500 Hz band), have low signal resolution, and are high susceptibility to movement artifact. SEMG electrodes typically are approximately 10 mm in diameter and are passive (i.e., they are simple conductive surfaces which perform better and worse in the case of low and high skin resistance respectively). They can, however, be active, incorporating preamplifier electronics that lessen the need for low skin resistance and improve the signal-to-noise ratio. Due to the non-invasive nature of SEMG, it finds clinical utility in the diagnosis of kinesiologic analysis of movement disorders; for differentiating types of tremors, myoclonus, and dystonia; for evaluating gait and posture disturbances; and for evaluating psychophysical measures of reaction and movement time [69]. SEMG can record both voluntary and involuntary muscle activity in addition to externally stimulated muscle action potentials such as motor evoked potentials after central or peripheral nerve stimulation. SEMG is recorded by attaching the electrodes above the surface of the skin, has a high repeatability and permits a prolonged monitoring of muscle activity from multiple sites simultaneously [70]. Figure−3.7 shows a diagram of the usual sites of measurement of muscle activity on the front and back of human body using SEMG as follows:

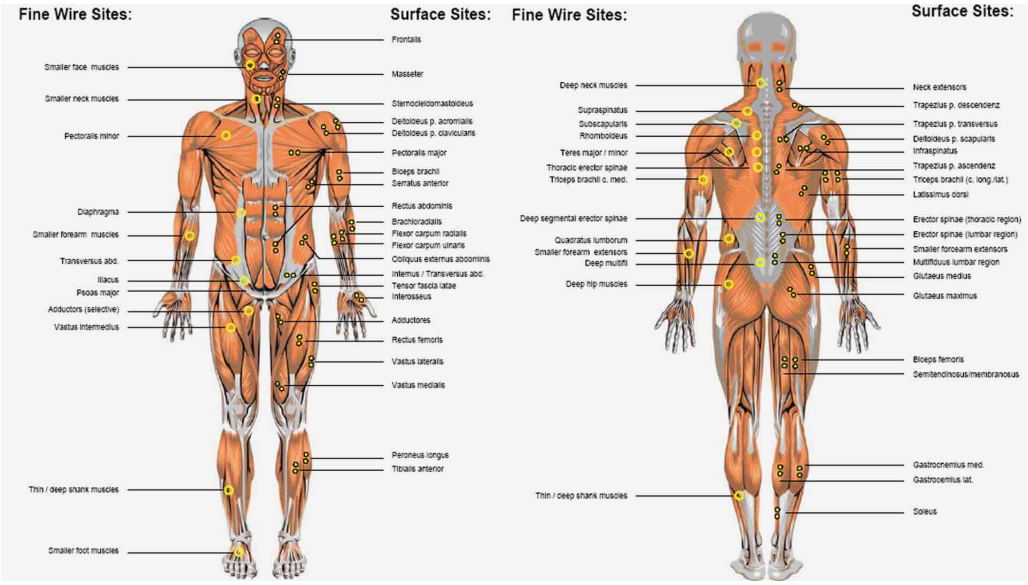

Figure 3.7: Recommended differential electrode placement sites for both FWEMG and SEMG; body front (left panel) and back (right panel) [7].

Besides SEMG of the muscle of interest, the electrodes placed on the skin also record interfering noise signals such as PI, EMA, MA and ECG. ECG interference is particularly high when the SEMG electrodes are positioned on the head and thoracic muscles [71] (i.e. placement of electrodes is close to the position of heart) and tends to decrease going towards the limbs. In this case ECG acts as an active noise component in SEMG recordings. The SEMG power content is included between 5 Hz and 450 Hz The ECG power content is included between 0.05 Hz and 100 Hz [72], with most components falling within 35-50 Hz. Consequently, SEMG and ECG components overlap in the 5-50 Hz range [73]. To provide a reliable interpretation of the muscular activities, SEMG signals must be filtered in order to enhance the SNR. Among the many solutions proposed in literature are adaptive filtering [74, 75, 76, 77], independent component analysis [78, 79, 80, 81], wavelet transform [82, 83], nonlinear filters [84] and most commonly used high-pass linear filtering. However, the choice about the correct high-pass cut-off frequency is controversial. All the frequency domain techniques for SEMG filtering estimate SEMG spectra with possible losses in the low frequency band. Indeed, low-frequency band is generally addressed to MA and ECG interference without any further investigation on the possibility of SEMG having significant spectral content.To avoid this limitation, time domain technique, such as the template-based ones, may be applied. Two studies are reported here; Study-1, to evaluate the low frequency components (below 20 Hz) of (thoracic) SEMG signals, in order to assess the correctness of the LF procedure usually applied to such signals to remove ECG components and, Study-2, to evaluate SEMG frequency content to understand if low-frequency spectral content is negligible or, on the contrary, represents a significant SEMG portion potentially providing

relevant clinical information.

Spectral analysis of low-frequency EMG components

Isometric recordings (IREC) acquired using five muscles (sternocleidomastoideus, erectores spinae at L4, rectus abdominis, rectus femoris and tibialis anterior) are modelled as the superimposition of SEMG, which is the signal of interest, and other corrupting signals, mainly ECG and instrumentation noise. Under the assumption of using modern electronic technology being substantially immune to instrumental noise that integrates power-line notch filters, IREC can be modeled as the summation of SEMG and ECG:

$$IREC = SEMG + ECG \tag{3.5}$$

The filtering procedure proposed here for deleting ECG components from IREC is SBMM-based. In this work, it was innovatively applied to get a clean SEMG from IREC (Figure−3.8). Precisely, at first IREC was treated as an ECG recording affected by SEMG (which initially serves as noise) and thus submitted to SBMM to estimate ECG (ECG_SBMM). If IREC does not include ECG, ECG_SBMM is a zero-constant signal. Once obtained, ECG_SBMM can be subtracted from IREC in order to estimate SEMG (SEMG_SBMM, the signal of interest):

$$SEMG\_SBMM = IREC - ECG\_SBMM \tag{3.6}$$

Use of SBMM in electromyographic applications is possible only if an additional ECG (AECG), is simultaneously acquired to IREC. Thus, ECG as in Equation−3.5 and AECG are two morphologically-different but simultaneously-recorded representations of the cardiac electrical activity, and thus are characterized by the same R-peaks. AECG is used for identification of R-peaks position, needed to SBMM for ECG_SBMM evaluation.

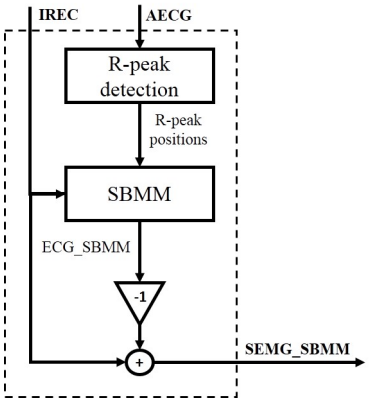

Figure 3.8: SBMM based procedure to get the surface SEMG from IREC by ECG interference subtraction.

Two studies were conducted to validate the proposed method: (1) simulation: To simulate an isometric contraction, the simulated SEMG (SimSEMG) was synthesized as in Ref. [29] as a bandlimited (0–150 Hz) stochastic process with zeromean Gaussian distribution (mean: 0.00 mV, standard deviation: 0.20 mV; amplitude: 0.80 mV, that is four times standard deviation) as indicated in [68]. Sampling frequency was 1000 Hz. The electrocardiographic pattern of simulated ECG (SimECG) contains the P wave, the QRS complex and the T wave, in order to simulate a physiological cardiac behavior was obtained as a 40-fold concatenation of a clean, 750 ms long real beat [30]. They were summed to get a simulated IREC (SimIREC):

$$SimIREC = SimSEMG + SimECG \tag{3.7}$$

The electrophysiological study involved real SEMG tracings of isometric contractions 10 young healthy subjects who were asked to perform a movement analogous to that performed during the Functional-Reach test [85]. This movement allows to get isometric contractions of both upper and lower body muscles among which sternocleidomastoideus, erectores spinae at L4, rectus abdominis, rectus femoris and tibialis anterior. SNR, defined as in Equation−(3.8), was used to quantify the amount ECG interference affecting SimIREC and IREC:

$$SNR = 10 \cdot log_{10}(\frac{\sigma^2_{signal}}{\sigma^2_{noise}}) \tag{3.8}$$

Here, “signal” and “noise” represent the SEMG and the ECG components, respectively. When not known, “noise” was estimated using SBMM. Spectral analysis was performed by computing the normalized Fourier power spectral density (PSD(f), with f being frequency), estimated via Welch’s method (windows length: 1 s). The median frequency (MdnF) was computed together with the percent amount of power (PSD%) in f1<f≤f2 band. Thus, PSD(0-450) represents the total power, since 0 Hz and 450 Hz are the lowest frequency and the highest frequency characterizing SEMG spectrum, respectively. Two bands were considered: the low-frequency band, defined for f1=0 Hz and f2=30 Hz; and the main-frequency band, defined for f1=30 Hz and f2=450 Hz.

In both the simulation and real data studies, SBMM was able to remove the ECG interference from SEMG without distorting the SEMG spectrum. In case of simulated data, IREC remains unaltered in case of absence of interference (SNR of SEMG_SBMM equal to in all cases). In addition, filtering does not significantly alter SEMG spectrum. Indeed, SEMG_SBMM MdnF was always equal to SimSEMG MdnF (that is 120 Hz). In addition, SEMG_SBMM and SimSEMG PSD% distributions in low- and main-frequency bands differed 2% at most. For the pysiological study, MdnF (over all subjects and muscles) was 74 Hz. Median PSD%(0,30) was 18%, indicating that almost a fifth of spectral content falls in the low-frequency band, and thus should not be neglected. The 18% low frequency component cannot be

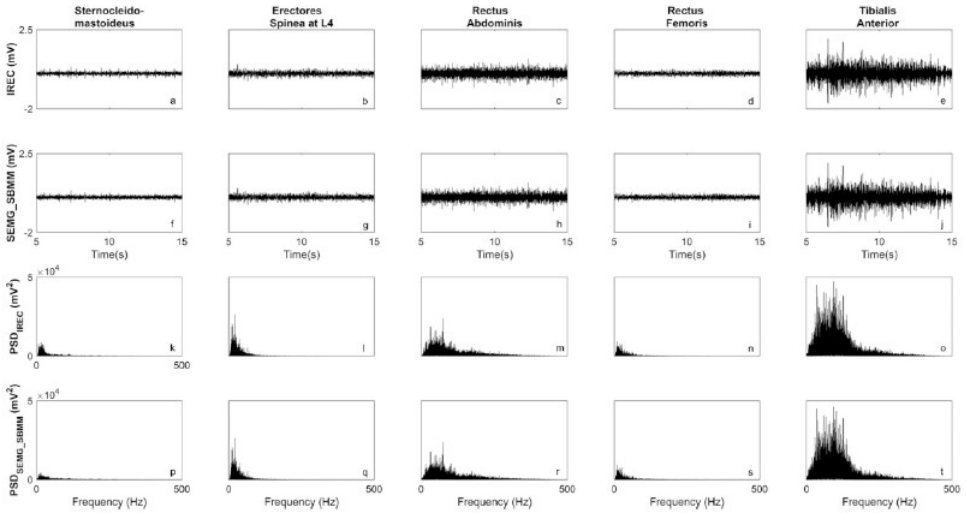

Figure 3.9: Qualitative representation of signals involved in the electrophysiological study in both time domain (panels a to j) and frequency domain (panels k to t). IREC represents the original acquisition during an isometric muscular contraction, which was submitted to SBMM based filtering procedure to get a clean SEMG estimation (SEMG_SBMM). PSD of IREC (PSDIREC; panels k to o) and SEMG_SBMM (PSDSEMG_SBMM; panels p to t) were obtained by Fourier transform.

addressed to ECG interference and/or motion artifacts, so SEMG filtering procedures should avoid canceling or distorting the SEMG low-frequency band not to limit subsequent SEMG scope and applications finalized to evaluate clinical content of this band.

Comparison with linear filtering

SEMG (corrupted with ECG) and standalone ECG signals acquired simultaneously using a wireless device (8-channel BTS POCKET SEMG 300 system with sampling rate: 1000 Hz) during an isometric recording (subject moving from rest to raising a 1 kg load in order to have an isometric contraction of the arm muscles.) and represented by REC1 and REC2. REC1 was recorded by placing an electrode over the left rectus abdominis and REC2 was recorded by placing another electrode over the left clavicle. Considering the motion artefacts and powerline interference negligible since the signals were acquired using a wireless sensor, REC1 could be modeled as a superimposition of a clean SEMG signal and an ECG signal, and REC2 as ECG as mathematically represented in Equation−(3.9) and (3.10):

$$REC1 = SEMG + ECG \tag{3.9}$$

$$REC2 = ECG \tag{3.10}$$

To obtain clean SEMG, REC1 was submitted to two filtering procedures were applied to REC1: one based on the SBMM, and the other based on linear filtering (LF) SBMM and LF, the latter being the standard one and a comparison for the frequency components deleted and retained by both procedures is performed. Initially SBMM was applied to estimate the ECG component (ECG_SBMM) included in REC1 (thus, SEMG is initially considered as noise affecting ECG). The Pan-Tompkins R-peak detection algorithm [63] was applied to REC2 in order to have the R-peak positions to be used by SBMM to filter REC1. Successively, a filtered SEMG signal (SEMG_SBMM) as in Equation−(3.11) was obtained by subtraction: Thus, SBMM application does not alter the frequency spectrum of SEMG and ECG, but simply separates the components of the two physiological signals overlapped in REC1.

$$SEMG_{SBMM} = REC1 - ECG_{SBMM} \tag{3.11}$$

Afterwards, linear filtering (LF) was performed using a high-pass filter implemented as a 2^{nd}-order bidirectional Butterworth filter. Once fed with REC, the filter provided a filtered SEMG signal (SEMGLF) as output. Since 20 Hz is included in both SEMG and ECG spectra, these result modified by the LF procedure.

Frequency analysis were performed by evaluating the PSD, estimated of REC1, SEMG_SBMM and SEMG_LF in the 0-450 Hz frequency range. A 20 Hz threshold frequency divided the spectrum in two parts, the part within before 20 the threshold frequency (within 0 to 20 Hz) and the part after it (within 20 to 450 Hz). Accordingly, two parameters were defined, respectively representing the amount of power spectra below low-frequency ratio (LFR) and over high frequency ratio (HFR) 20 Hz. To obtain SEMG_SBMM, SBMM extracted ECG_SBMM from REC1 using the R-peak locations detected in REC2. SEMG_LF is obtained after performing the LF procedure to REC1. SEMG_LF spectral parameters (LFR=9% and HFR=91%) seem to indicate a strong reduction of the ECG components but this finding is a direct consequence of the filtering procedure. The findings suggest that SBMM does not alter the frequency content of the signals involved, since it is based on the morphological reconstruction of the noise. Instead, the second filtering procedure is LF and consists in the application of a 20 Hz high-pass filter to REC1 in order to remove ECG. This procedure alters the spectra of both SEMG and ECG signals, since these extend from 5 Hz to 450 Hz and from 0.5 Hz to 50 Hz, respectively. Both visual and quantitative (through spectral parameters and SNR) evaluation of the results indicate that SBMM eliminate the ECG component from REC1 better than LF. In addition, after filtering, SEMG showed a significant amount of PSD (up to 20%) in the low-frequency range, power that is typically eliminated by LF, and that according to literature [86] represents the firing rates of the active motor units. Hence in conclusion we can say that SEMG has significant spectral components below 20 Hz, which however are typically eliminated by linear filtering applied to avoid ECG interferences. The SBMM is an alternative filtering procedure that eliminates the

ECG component from SEMG acquisitions without altering its power spectra. Thus, SBMM represents a promising tool to be used in future studies finalized to evaluate the clinical utility of the 5-20 Hz band in SEMG studies.

3.2.3 Electrocardiogram-derived respiration

Respiration rate and variability are indicators of changes in health condition. In chronic disease management, it is highly desirable to use wearable devices in order to minimize invasiveness and maximize comfort. However, not all wearable devices integrate sensors for direct acquisition of respiratory (DAR) signal. In these cases, the breathing extraction can be done through indirect methods, typically from the ECG called electrocardiogram-derived respiration (EDR) signal. Indeed, effects of breathing on ECG modulation depend on respiratory characteristics of subjects (e.g. chest or abdominal breathing), on the position of the heart and the relevance of its rotation [87].

In this study 2-channel ECG (ECG−I and ECG−II) and DAR signal simultaneously acquired were used from [88, 60]. Both ECG−I and ECG−II were processed with a SBMM based procedure [4, 58, 39] to derive respiration signals (EDR−I and EDR−II, respectively). Specifically, the procedure involved three steps as shown in Figure−3.10: prefiltering (35 Hz lowpass 3^{rd} order, bilinear Butterworth filter), SBMM application and respiration signal derivation. Then, both filtered ECG and R-peak sequence detected by [63] were given as input to SBMM. Output of SBMM was a clean ECG not affected by respiration. Consequently, EDR could be derived by subtraction.

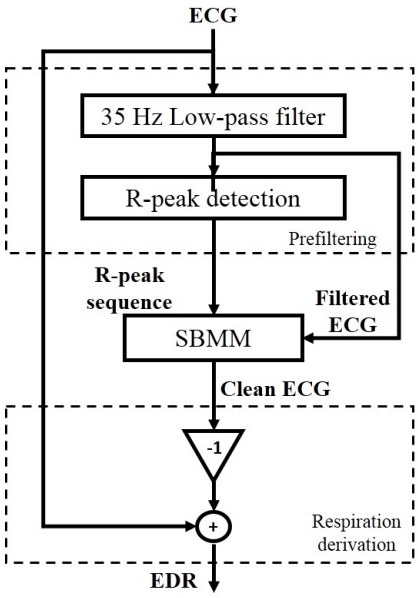

Figure 3.10: SBMM-based procedure for EDR computation.

EDR−I and EDR−II, respectively obtained by applying ECG−I and ECG−II

to the SBMM-based procedure, were both compared to DAR in terms of spectral analysis. The fast Fourier transform (FFT) of each 12000 sample (200Hz·60 s) signal was computed over 16384 (214) sample points, reached by zero-padding. Respiratory frequency (RF) was identified as the frequency at which the magnitude spectrum of the fast Fourier transform had a maximum in the respiratory frequency range, that is 0.07-1.00 Hz. If the spectrum had more than one peak, the peak frequency nearest to 0.20 Hz was taken as RF, being 0.20 Hz the average RF in adults. Accuracy in RF identification was evaluated as signed differences (Δ) between RF values from DAR and EDR signals.

An example of application of the SBMM-based procedure to real clinical data is depicted in Figure−**??** that shows DAR and corresponding EDR−I and EDR−II relative to record b010. As it can be seen, EDR signals are in general smoother that DAR signal; phases may be concordant, as in the present case, or opposite. Typically, respiration is a corrupting factor affecting ECG. SBMM was fond to be able to extract a clean version of ECG so that respiration can be derived by subtraction.

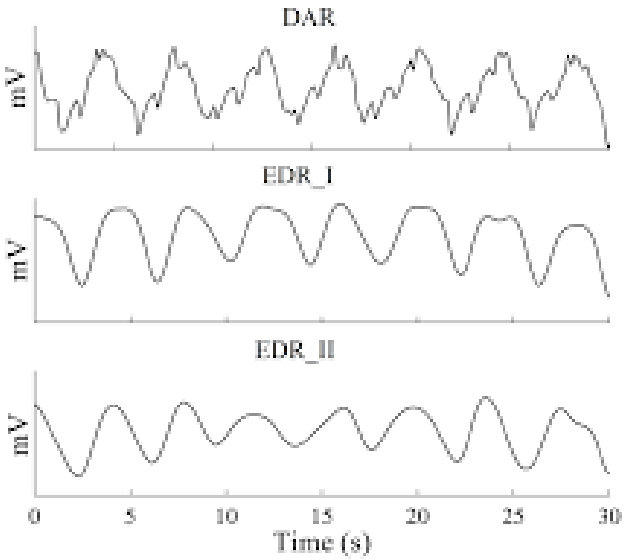

Figure 3.11: DAR, EDR−I and EDR−II signals (30 s windows) relative to record 'b010'.

SBMM works properly only if correct R-peak sequence is provided; thus, reported results have to be interpreted under the hypothesis of correct R-peak localization (which is generally not particularly challenging). The SBMM-based procedure proposed here belongs to the latter class, and offers the possibility to choose the most convenient lead. Still, some single-lead methods, specially used during sleep studies, are bound to use some specific leads due to the electrodes placement. Since there is no extra sensor required for EDR extraction, SBMM-based procedure is also useful for long-term, possibly real-time monitoring, for example by wearable sensor or smartphone applications driving cloud computations. Future studies will

evaluate the proposed SBMM-based technique to larger populations, possibly affected by respiratory problems. Multilead ECG recordings are also desirable to evaluate if, among the 12 standard leads, some are optimal for EDR extraction and FR identification. The proposed procedure, based on SBMM, is as a promising tool for EDR estimation and RF identification from a single lead ECG.

3.3 Limitations

The main limitation of SBMM, presented in this study, is that it assumes all ECG beats to be sinus (this also explains why clinical ECG tracings from healthy subjects were used here). If few ectopic beats are present they will not appear in the estimated ECG since only one template for the most frequent beat kind is computed. Future research will be aimed at improving this first version of SBMM in order to include also no-sinus beat morphology, making accurate ECG estimations possible from noisy recordings of patients with cardiac pathology.

Also in the current studies, SBMM was applied to short term recordings i.e. 60 s long in case of FECG extraction, 60 s in case of EMG denoising, 1 minute in case of EDR extraction because the aim was the evaluation of a denoising technique for FECG, EMG and EDR applications and not the continuous monitoring, which is a general scenario for wearable sensing. To account for the physiological variability SBMM needs to be adapted to changing HR which is suggested for future work.

Additionally, since modern hardware for wearable devices is evolving towards GPU-based processing, and long-term ECG data acquisitions require a good storage capacity which is typically achieved through data compression, SBMM's utility is limited to computationally intensive and short-term data processing. These are some of the limitations solved by this work and explained in detail in the next chapter.

Chapter 4

Extended Segmented Beat Modulation Method

As identified in Chapter 3, there are numerous areas where SBMM needs improvement or adaptation to increase its usability targeting specific applications such as non-sinus beats or arrhythmia identification and denoising, adaptation to wearable ECG sensing scenarios for continuous and long-term monitoring of cardiovascular conditions. This following sections include all the novel modifications and/or additions made to SBMM algorithm in order to overcome the limitations of previously published works [4, 39, 58, 6, 41, 40], and increase its usability to arrhythmia detection and denoising using modern hardware platforms like wearable sensors.

4.1 Proposed Extended Segmented Beat Modulation Method

The Extended Segmented Beat Modulation Method (ESBMM) was proposed to overcome the SBMM's main limitation of being applicable only in case of the normal sinus rhythm. The ESBMM is based on a different CC segmentation from the SBMM (Figure−4.2) and performs the following four steps (Figure−4.1): (1) a CC identification and segmentation step, in which each CC is segmented into PQRS and TU segments (instead of QRS and TUP segments as done in the SBMM); (2) a feature-extraction step, in which each CC is characterized in terms of temporal, morphological, and spectral features; (3) a classification step, based on a CNN, in which beats are classified as normal (N), supra-ventricular (S), and ventricular (V); and (4) a denoising step. A clean ECG estimate is obtained at the output to retain the heart rate and morphological variability of the input ECG. The proposed method was tested on the well-known MIT–BIH arrhythmia database [89] and evaluated under two performance criteria: (1) classification for N, S, or V beat classes according to the patient-based assessment; and (2) denoising reporting signal-to-noise ratios for the ECG recordings in the database evaluated on the basis of noise cancellation assessment criteria. Details of the proposed procedure are reported below.

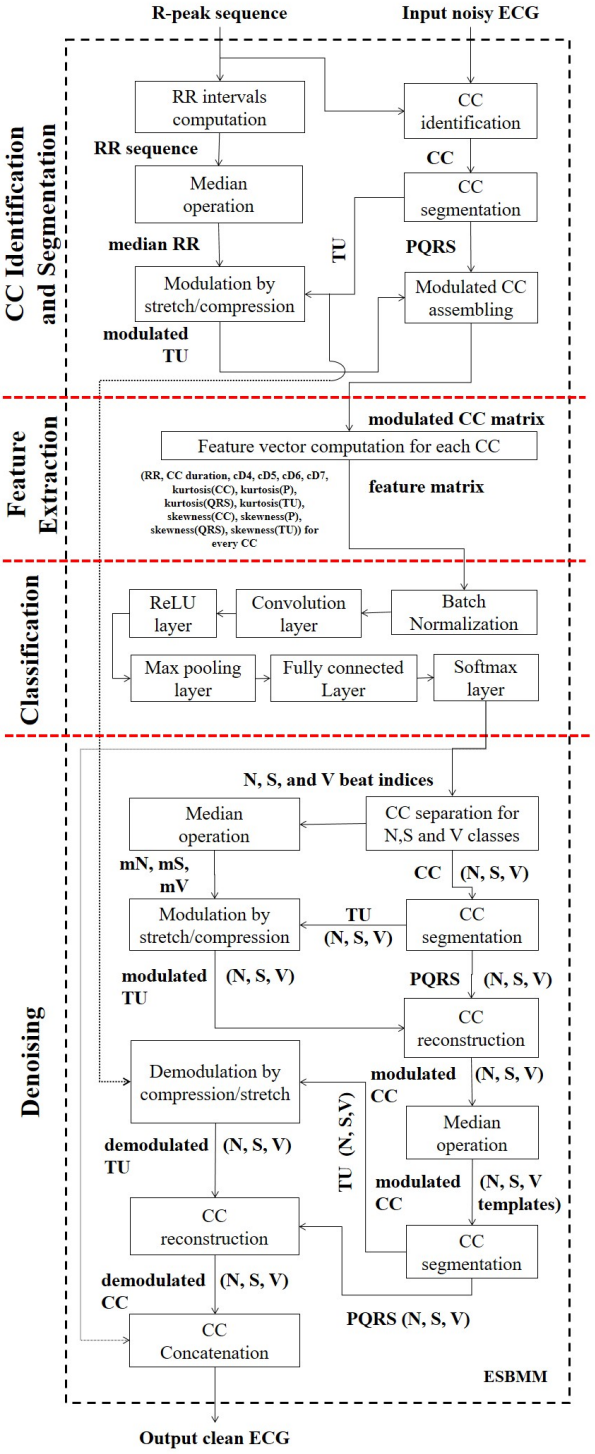

Figure 4.1: Flow chart of the ESBMM algorithm.

4.1.1 Preprocessing

In the preprocessing stage, power and low-frequency interference is removed from the raw ECG signal using a $6^{th}-$order bidirectional Butterworth band-pass filter with lower and upper cut-off frequencies of 0.5 Hz and 40 Hz, respectively. The baseline is computed as a cubic spline interpolation of fiducial points, placed 90 ms before R-peak position and subtracted from the bandpass-filtered signal.

4.1.2 CC identification and segmentation

According to the ESBMM, the CC onset fiducial mark is assumed at Δt_1 before each R-peak position, and the CC offset as Δt_1 before the succeeding R-peak position (typically, $\Delta t_1 = 250$ ms) as shown in Figure−4.2. All CCs are then segmented into a PQRS segment (from Δt_1 before the R-peak position until Δt_2 after the R-peak position; typically, $\Delta t_2 = 40$ ms) and TU segment (from Δt_2 after the R-peak position until the end of CC). The TU segments are then modulated (stretched or compressed) to match the median TU length calculated over lengths of all TU segments (CC duration $-$ $(\Delta t_1 + \Delta t_2)$). The CCs are then reconstructed by concatenating PQRS and modulated TU segments. The result is a batch consisting of all CCs of equal length.

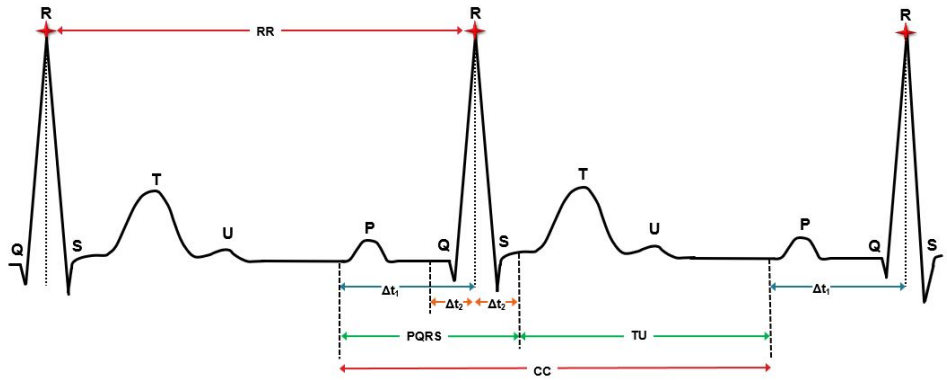

Figure 4.2: CC with its PQRS and TU segments, and associated RR interval according to ESBMM.

Figure−4.3 shows examples of CC waveforms for beats classified as N, S, and V, respectively.

4.1.3 Feature extraction

For each CC, a feature vector was computed. The feature vector was constructed using the following: features related to temporal intervals, features obtained by applying discrete wavelet transform to the modulated CC, and statistical features. The features related to temporal intervals are RR interval and CC duration. The features based on the 'Daubechies 4' wavelet transform of the modulated CC are obtained using

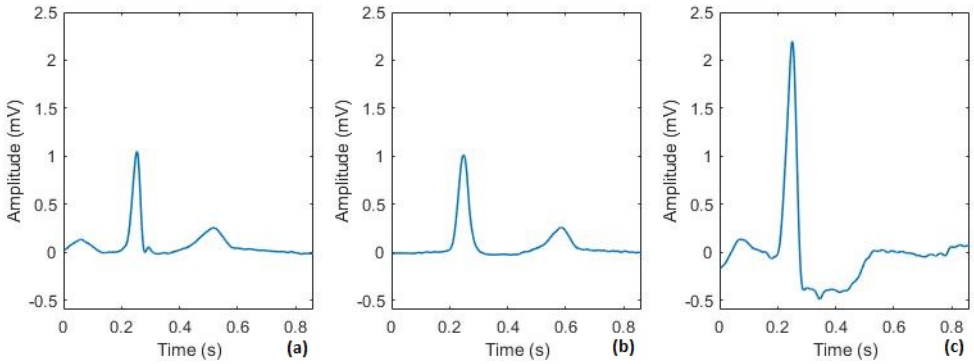

Figure 4.3: Examples of CC waveforms for beats classified as N; (panel **a**), S; (panel **b**) and V; (panel **c**).

decomposed wavelet coefficients at detail levels 4 to 7 (cD4, cD5, cD6, and cD7) [90]. The statistical features are kurtosis (4th order statistics) and skewness (3rd order statistics) calculated as in Equations (4.1) and (4.2), respectively, of the entire CC, and of P (onset: Δt_1 ms before the R-peak position, offset: Δt_2 ms before the R-peak position; Figure−4.2), QRS (onset: Δt_2 ms before and after the R-peak position; Figure−4.2), and TU (onset: Δt_2 ms after the R-peak position, offset: Δt_2 ms before the next consecutive R-peak position; Figure−4.2) waves taken from the modulated CC since they represent the morphological distortion of the entire CC and of P, QRS, and TU waves, respectively.

$$\text{kurtosis} \;=\; \frac{\sum_{i=1}^{N}(x_i-\bar{x})^4/N}{std^4} \tag{4.1}$$

$$\text{skewness} \;=\; \frac{\sum_{i=1}^{N}(x_i-\bar{x})^3/N}{std^3} \tag{4.2}$$

where $\bar{x}$ is the mean, std is the standard deviation, and N is the number of data points. The final feature vector now becomes the RR interval, CC duration, cD4, cD5, cD6, cD7, kurtosis (CC), kurtosis (P), kurtosis (QRS), kurtosis (TU), skewness (CC), skewness (P), skewness (QRS), and skewness (TU).

4.1.4 Convolutional neural network classification

The convolutional neural network (CNN) classifier input consists of the number of parameters equal to the number of features extracted in the previous step and the number of samples equal to the number of beats in the ECG recording currently being processed. The output consists of three beat classes: N, S and V beat classes, respectively. Synthetic data are used to overcome the imbalance in the number of ECG heartbeats in the three classes according to the synthetic minority oversampling technique [91]. N class, in this case, is the majority class, hence, the number of the CCs in S and V classes is increased to match the number of CCs in the N

class. The architecture of the implemented CNN is as follows: the input feature vector, batch normalization layer, convolution layer (kernel size: 3, filters: 16), fully connected layer (number of neurons: 16), fully connected layer (number of neurons: 3), and output SoftMax layer. True AAMI beat labels were used as references during training.

4.1.5 Denoising

Beats classified as N, S, and V were used to create three templates, one for each class. For each class, the median beat duration, the median PQRS duration, and the median TU duration are computed using the RR-intervals of all beats belonging to the same class. Each CC of each beat is then segmented into PQRS and TU segments. The TU segment of each beat is modulated (stretched/compressed) to match the median TU duration of its class. All CCs of all beats belonging to the same class are now characterized by the same length, and the template of that class can be obtain mediating all these beats. Finally, each noisy beat of noisy ECG is replaced by the demodulated (compressed/stretched) template of corresponding class.

4.2 Validation study

4.2.1 Clinical data

The data used for testing the classification and denoising efficiency of the proposed algorithm were taken from the MIT–BIH arrhythmia database developed by Massachusetts Institute of Technology (MIT) and Boston's s Beth Israel Hospital (BIH) in 1987 and available as open source on Physionet [89, 60]. Only limb lead II (as in [92]) of the 35 ECG recordings (ID 100, 101, 105, 106, 108, 109, 113, 114, 116, 118, 119, 123, 124, 200, 201, 202, 203, 205, 207, 208, 209, 210, 213, 214, 215, 217, 219, 220, 222, 223, 228, 231, 232, 233, 234) out of the 48 available ones were used here, since the remaining 13 were single beat-class recordings for which the proposed ESBMM simplifies into the SBMM. The 35 ECG recordings used were approximately 30 min long and were acquired from 35 subjects, 19 men (53 to 89 years old) and 16 women (23 to 89 years old). Approximately 60% of these recordings were obtained from inpatients. Recording numbers 100–124, with some numbers missing, include a variety of waveforms and artifacts that an arrhythmia detector might encounter in routine clinical use. Furthermore, recording numbers 200–234, again with some numbers missing, include a variety of rare but clinically important phenomena such as complex ventricular, junctional, supraventricular arrhythmias and conduction abnormalities. Each recording is supported by an annotation file made available by the MIT–BIH arrhythmia database, providing the positions of R-peaks and corresponding label for each heartbeat compiled by clinical experts [89, 60]. From each ECG recording, ECG windows containing 30 consecutive beats were consecutively extracted to be analyzed from the ESBMM. A division of the dataset was used to

train (60%) and test (40%) the ESBMM in the classification step of the methodology. True AAMI beat labels were used as references. ESBMM performance was evaluated on a PC workstation with two Intel(R) Core (TM) 3.40 GHz (CG8250) processors and 12 GB of RAM. Detail of the MIT–BIH database is provided in Table−4.1.

Table 4.1: Association for the Advancement of Medical Instrumentation (AAMI) to MIT–BIH annotation mapping detail.

AAMI	MIT–BIH	Beat Description
N	N or .	Normal beat
	L	Left bundle branch block
	R	Right bundle branch block
	e	Atrial escape beat
	j	Nodal (junctional) escape beat
S	S	Supraventricular premature beat
	A	Atrial premature beat
	a	Aberrated atrial premature beat
	J	Nodal (junctional) premature beat
V	V	Premature ventricular contraction
	E	Ventricular escape beat
	!	Ventricular flutter wave

4.2.2 Classification

The ESBMM performance in classifying heart beats into the three N, S, and V classes was performed in terms of overall accuracy (Acc) and individual positive predictive value of each class (PP(N), PP(S), and PP(V), respectively) as computed in Equation (9.12), (8.6), (4.5) and (4.6), respectively:

$$Acc = \frac{TN + TS + TV}{TN + FN + TS + FS + TV + FV} \quad , \tag{4.3}$$

$$PP(N) = \frac{TN}{TN + FN} \quad , \tag{4.4}$$

$$PP(S) = \frac{TS}{TS + FS} \quad , \tag{4.5}$$

$$PP(V) = \frac{TV}{TV + FV} \quad , \tag{4.6}$$

where, TN, TS, and TV represent correctly classified (true) N, S, and V beats, respectively, and FN, FS, and FP represent wrongly classified (false) N, S, and V beats, respectively.

4.2.3 Denoising

ESBMM performance in ECG denoising was assessed in terms of signal-to-noise improvement (SNR_{imp}) as given in Equation−(9.13), where SNR_{in} and SNR_{out}

are the signal-to-noise ratio (in dB) of the ECGs at ESBMM input and output, respectively, and are defined as in Equations−(9.14) and (4.9):

$$SNR_{imp} = SNR_{out} - SNR_{in} \quad , \tag{4.7}$$

$$SNR_{in} = 20 \times log(\frac{PeaktoPeakECG_{in}}{4 \times std(ECG_{in})}) \quad , \tag{4.8}$$

$$SNR_{out} = 20 \times log(\frac{PeaktoPeakECG_{out}}{4 \times std(ECG_{out})}) \quad , \tag{4.9}$$

where $PeakToPeakECG_{in,out}$ is an ECG signal-measure representing a median over maximum minus minimum amplitudes of all ECG beats and $std(ECG_{in,out})$ is a noise-measure representing standard deviation of $ECG_{in,out}$ respectively. Normality of the SNR_{imp} value over the 35 ECG recordings was evaluated using the Lilliefors test. Non-normal distributions were described in term of median (50^{th} percentile) and its $[25 - -75^{th}]$ percentiles range, and compared using the rank sum test. A median SNR_{imp} value statistically greater than zero (p-value < 0.05) indicates a significant improvement in signal quality, and thus a good denoising performance of the ESBMM.

4.3 Achieved results

4.3.1 Classification

The proposed algorithm took approximately 273 min (approx. 4.5 h) to process all 35 ECG recordings. Table−8.1 represents data split into training and testing subsets, and the data split was carried out according to beat annotations provided with the dataset. A 60:40 division ratio of the total dataset into training and testing datasets led to the distribution of beats over the N, S, and V classes as reported in Table 8.1.

Table 4.2: Number of beats per beat-class and datasets.

Dataset/Class	**N**	**S**	**V**	**Total**
Training	41,020	1646	4057	46,723
Testing	27,346	1097	2704	31,147
Total	68,366	2743	6761	77,870

Confusion matrices relative to beat classification as N, S, and V for the training, testing and total datasets are reported in Table 4.3. Overall, more than 90% of the total beats were correctly classified. Values of Acc, PP(N), PP(S), and PP(V) for the testing, training, and total datasets are reported in Table−4.4.

Recording numbers 108, 114, 118, 124, 200, 201, 202, 205, 207, 210, 213, 215, 219, 223, 228, 233, and 234 each have N, S, and V beats. Recording numbers 100, 101,

Table 4.3: Confusion matrices relative to beat classifications (normal (N), supraventricular (S), and ventricular) for the training, testing, and total datasets.

	True/Predicted	N	S	V	Total
Training	**N**	39,205	765	1050	41,020
	S	15	1604	27	1646
	V	202	342	3513	4057
	Total	39,422	2711	4590	46,723
Testing	**N**	25,388	722	1236	27,346
	S	51	1019	27	1097
	V	391	198	2115	2704
	Total	25,830	1939	3378	31,147
Total	**N**	64,603	1487	2276	68,366
	S	66	2623	54	2743
	V	593	523	5645	6761
	Total	65,262	4633	7975	77,870

Table 4.4: Values of overall accuracy (Acc), PP(N), PP(S), and PP(V) for the testing, training, and total datasets.

Dataset	**Acc**	**PP(N)**	**PP(S)**	**PP(V)**
	(%)	(%)	(%)	(%)
Training	94.86	85.57	97.44	86.59
Testing	91.57	92.84	92.89	78.21
Overall	93.58	94.49	95.62	83.49

113, 209, 220, 222, 231, and 232 each have N and S beats. Recording numbers 105, 106, 109, 116, 119, 123, 203, 208, 214, 217 contain N and V each. Recording number 102, 103, 104, 107, 111, 112, 115, 117, 121, 122, 212, 221, and 230 have no or single abnormal beat instances.

4.3.2 Denoising

SNR_{imp} distribution was not normal; its median value was 0.99 [0.15;2.66] dB, which was significantly higher than 0 ($p < 0.05$). Figure−4.4 shows, as an example, a noisy section of recording number 105 with ECG_{in} and ECG_{out} computed using the proposed ESBMM algorithm; for this recording SNR_{imp} was 6.08 dB.

4.4 Robustness to noise evaluation

In order to verify the ESBMM ability to properly classify beats and denoise ECG signals in noisy conditions, we performed the following evaluation: from each of the 35 selected recordings of the MIT database, we selected, if present, a 5-min ECG segment with at least 3 N, 3 S,and 3 V beat instances. This selection criterion was introduced to have a balanced number of beats in each class despite the reduction in ECG length.

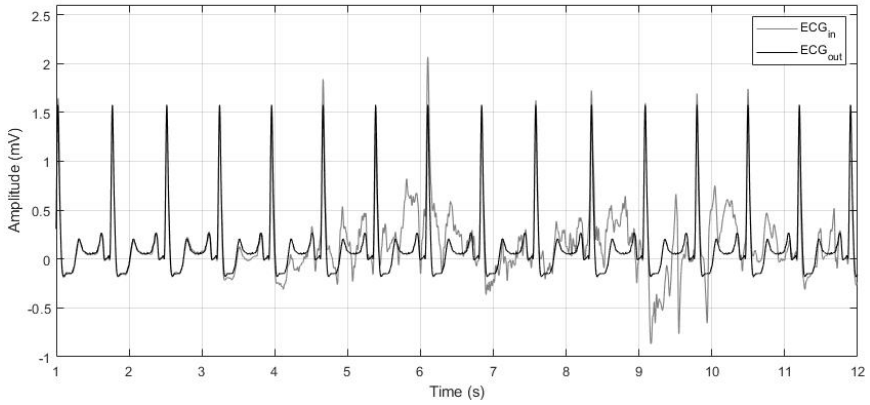

Figure 4.4: As an example, the figure depicts an electrocardiogram (ECG) window from recording number 105 at the input (ECG_{in}) and at the output (ECG_{out}) of the extended segmented beat modulation method (ESBMM).

Successively, three different noise types typically affecting the ECG were added, which are baseline wander, muscle activity, and electrode motion artifacts. All noise signals were taken from the MIT–BIH Noise Stress Test database [61] also available on Physionet and consist of real noise recordings acquired through ECG electrodes located on the limbs to make the amplitude of the ECG component negligible (and thus not visible) with respect to that of the noise. Both clean and corrupted versions of each ECG segment were eventually submitted to the ESBMM in order to evaluate its robustness to noise in terms of Acc, PP(N),PP(S), PP(V), and SNR_{imp}.

Overall, 33 5-min ECG segments were found to satisfy the criteria for the evaluation of the ESBMM robustness to noise. The results relative to this evaluation are reported in Table−4.5. Regarding classification, Acc and PP(N) were only slightly affected by noise; PP(S) decreased significantly only in the presence of electrode motion artifacts; and PP(V) was affected by all types of noise even though it remained at least at 60%. Eventually, SNR_{imp} was less than 2 dB in the absence of noise but increased in the presence of noise until exceeding 5 dB in the presence of electrode motion artifacts. Figure−4.5 shows, as an example, a 10 s section of recording number 202 with ECG_{in} corrupted by: (a) no additional noise; (b) baseline wander; (c) muscle activity; and (d) electrode motion and the respective ECG_{out} computed using the proposed ESBMM algorithm.

4.5 Discussion on achieved results

The current work proposes the ESBMM as an extended and improved version of the existing SBMM, which is able to denoise ECG tracings characterized by sinus as well as nonsinus rhythm. This feature makes the ESBMM applicable in many more applications than the SBMM. The main differences between the ESBMM and SBMM

Table 4.5: Values of Acc, PP(N), PP(S), PP(V), and SNR_{imp} for selected 5-minute ECG segments corrupted by various types of noise.

Noise type	**Acc** (%)	**PP(N)** (%)	**PP(S)** (%)	**PP(V)** (%)	$\boldsymbol{SNR_{imp}}$ **(dB)**
No additional noise	93.38	96.48	76.33	78.60	1.71 [0.46; 2.97]
Baseline wander	91.36	95.88	75.44	62.33	2.67 [1.76; 3.57]
Muscle activity	91.52	96.45	73.11	60.00	3.86 [3.01; 4.68]
Electrode motion artifacts	91.11	95.85	52.88	65.43	5.02 [3.30; 6.71]

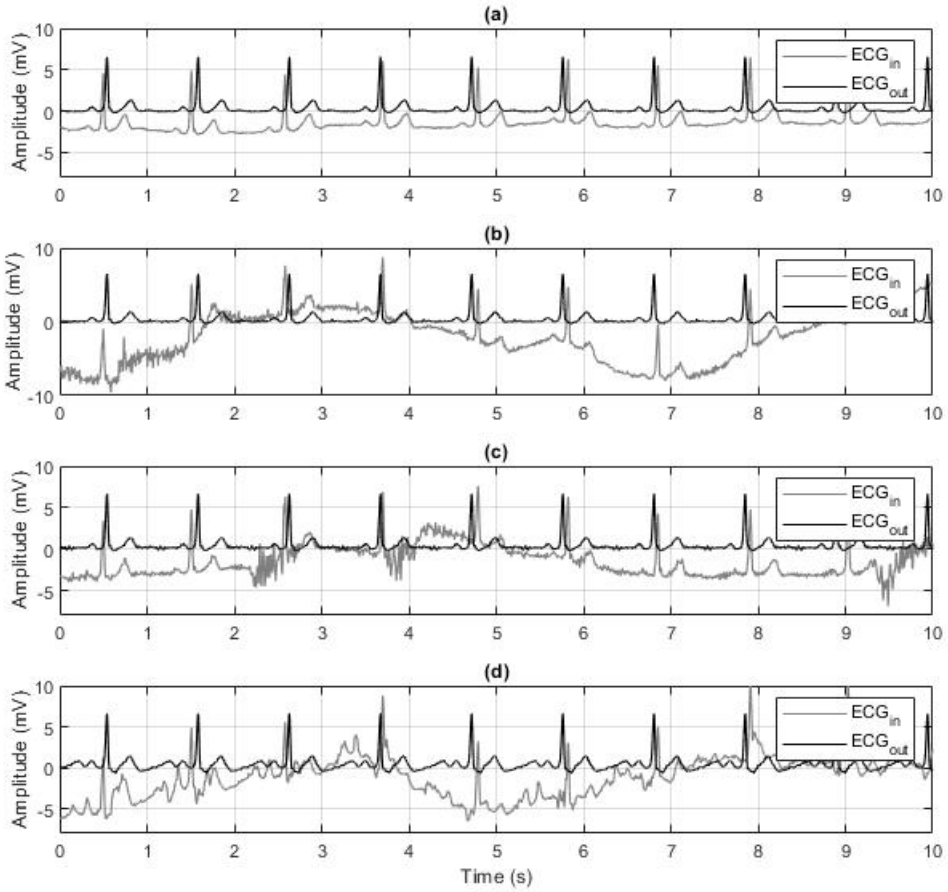

Figure 4.5: As an example, the figure depicts an ECG window from recording number 202 at the input (ECG_{in}) and at the output of the extended segmented beat modulation method (ESBMM). In panel (**a**), ECG_{in} was not corrupted by additional noise. Differently, in panels (**b**–**d**), ECG_{in} was corrupted by baseline wander, muscle activity, and electrode motion artifacts, respectively.

consist in a different segmentation of the cardiac cycle and in the insertion of a procedure for beat classification. According to the ESBMM, each cardiac cycle is still

segmented into two segments, but the first (i.e., the PQRS segment) includes the P wave and the QRS complex, while the second (i.e., TUP segment) includes the T and U waves, respectively. Differently, according to the SBMM, the first segment (i.e., the QRS segment) includes only the QRS complex, while the second (i.e., the TUP segment) includes the T wave, the U wave, and the P wave of the successive cardiac beat. The reason for including the P wave in the same segment in which the QRS complex is present relies on the fact that the P wave and QRS complex both represent the same electric phenomenon, which is depolarization, though of the atria and ventricles, respectively. Consequently, they can be hypothesized to show a similar dependency of instantaneous heart rate. Moreover, evaluation of P-wave presence and morphology is fundamental for a beat classification (all supraventricular arrhythmias show abnormalities at P-wave level). Taking into account that the electrical activity of a cardiac beat starts with the P wave, when classifying a cardiac beat, its P wave has to be present in the segments representing it and not in the segments representing the previous one.

Beat classification relies on features related to temporal intervals (RR interval and CC duration), features obtained applying discrete wavelet transform to the modulated CC (cD4 to cD7), and statistical features (kurtosis and skewness). Since in each ECG recordings, after modulation of all TUPs, each CC is equal in length, the number of wavelet decomposed coefficients is the same for all beats. Asl et al. [90] reported that the representative and distinct components for each type of heartbeat can be found in the detail information at level 4 to 7.

Hence, only the wavelet coefficients at detail levels 4 to 7 (i.e., cD4, cD5, cD6, and cD7, respectively) were used here as features for morphological classification. Zhang et al. [93] proved that the RR interval is a highly distinguishing factor for the separation of N and S beats, hence each CC had an associated RR-interval feature. The skewness and kurtosis are effective in estimating shape distortion of any signal compared to Gaussian distribution. They were well able to distinguish between V and other beats since the major difference of V beats with other types of beats is the shape [94]. Hence, the kurtosis of CC and skewness of CC were considered.

Beat classification was performed using a convolutional neural network which receives several temporal and morphological ECG features as input. Some of them were standard (such as the RR interval); others were obtained by analyzing the ECG signal using the discrete wavelet transform and by computation of higher order statistics. Several techniques have been previously proposed for classification of cardiac arrhythmic beats in the past years [92, 93, 95, 96, 97, 98, 99, 100]. Table−4.6 proposes a comparison of the results obtained with the ESBMM against other methods that were tested on the same database. De Chazal et al. [101] used a simple feature set based on heartbeat and RR intervals plus wave morphology. Zhang et al. [93] presented a one-versus-one feature reduction strategy focusing on the disease-specific features supporting the traditional support vector machine binary classifier. Eventually, Chen et al. [92] proposed a combination of projected

and dynamic features for arrhythmia classification and a support vector machine classifier to cluster heartbeats. As can be seen from Table 4.6, all methods were able to reliably classify N and V beats, but only the ESBMM was also able to reliably classify S beats. The numbers of false positives in V beats seems to be quite high. This effect could be due to the presence of bundle branch block beats in the class N, that could be erroneously classified in class V. Future studies will evaluate the possibility of including the bundle branch block beats in an additional fourth class, in order to solve this limitation of our approach.

Table 4.6: Beat classification performances over the MIT–BIH.

Method	**%Acc**	**%PP(N)**	**%PP(S)**	**%PP(V)**
ESBMM	91.5	92.8	95.6	83.4
deChazal [101]	81.9	99.2	38.5	81.9
Zhang [93]	86.7	99.0	36.0	92.8
Chen [92]	93.1	95.4	38.4	85.1

The ESBMM is a template-based method for ECG denoising. It operates in short-term ECG. In case of long-term ECG, it is applied to short ECG windows recursively extracted from the long recording. This design choice allows one to maintain physiological ECG variability (time and amplitude) by significantly reducing the level of noise. However, thanks to the beat classification procedure, three templates (instead of one, as for the SBMM) are computed, one for each beat class (N, S, and V). Each template is obtained by performing the median computation over all beats belonging to a class, an operation which is known to reduce noise and to provide the most likely morphology in a class of beats. In order to perform the median operator, all CC needs to be modulated to have the same length. Indeed, the hypothesis behind the procedure is that each beat of a class is a slight modification of a class specific morphology (best represented by the median, i.e., the template). Thus, the beat modulation is only an intermediate step to obtain a denoised template for each class. Template waveforms are then concatenated, demodulated, and adjusted in order to provide an output clean ECG tracing characterized by the same beat-to-beat heart-rate variability characterizing the input noisy ECG.

The ESBMM's ability to denoise ECG tracings is confirmed by the statistically significant improvement of the signal-to-noise ratio that, on average, was 0.99 dB, with peaks of up to 6.08 dB. The median limited improvement in the MIT–BIH arrhythmia database is not due to the fact that the ESBMM's denoising ability is limited, but, rather, to the low level of noise affecting the recordings. The MIT–BIH arrhythmia database was chosen because it allowed us to evaluate the performance of the ESBMM in beat classification, which is the main novelty of the ESBMM with respect to the SBMM. However, the ESBMM's robustness to corrupting factors such as baseline wanders, muscle activity, and electrode motion artifacts was also evaluated. The results confirm the ability of the method to estimate good quality

ECG recordings in the presence of typical noises affecting the ECG, especially for the N class, analogous to what was previously observed for the SBMM [4, 58]. Indeed, since in an ECG recording, the number of N beats is generally much higher than the number of S and V beats, the template of class N is typically much cleaner than the templates of class S and V. Consequently, PP(N) is much less affected by the presence of noise than PP(S) and PP(V).

4.6 Contributions

This chapter presented the main novel mechanism added to a previously published version of SBMM algorithm as ESBMM, GPU-SBMM, DCT-SBMM and dynamic-template SBMM. The main contributions of this work is summarized as:

- A new ECG segmentation procedure that separates repolarization waveforms from depolarization waveforms;
- A proposed feature vector composed of spectral, RR interval, and higher-order statistical features;
- A CNN to classify cardiac beats into N, S, and V classes;
- A denoising algorithm designed to separately construct median templates for N, S, and V beats and reconstruct the original ECG recording including arrhythmic beats to match the original beat duration and morphology.
- A GPU based vector implementation of SBMM which is faster, applicable to wearable sensing hardware and tested for ECG signals acquired during sports and training;
- A preliminary test using DCT compression at various levels and trade-off assessment against signal quality improvement for data acquired by wearable sensors in long-term ECG signal acquisitions.
- HR adaptation of SBMM to make it applicable for long-term ECG signal processing as factually the HR and HRV does not remain constant over time and is an important factor in diagnosing heart abnormalities.

Chapter 5

Compressed Segmented Beat Modulation Method

5.1 Long-term and continuous CVD monitoring

Continuous and long-term ECG monitoring has nowadays become critical for the identification and analysis of unforeseen abnormality markers that may occur at instances other than during the standardized ECG test. With the increase in the usage of online ECG processing and wearable sensing applications there is a need for increased storage capacity to store and transmit lengthy ECG recordings, offline and over the cloud for continuous monitoring by the clinicians [102, 103, 104, 105]. Additionally, the transmission of large amount of ECG data consumes a great deal of energy and reduces the battery life of both the wearable device and the processing firmware [103]. ECG signals acquired in the raw form are usually corrupted with unwanted noises such as muscle activity, electrode artifacts, line interference, and respiration [104]. A proper characterization of waveform morphologies is required regarding both the accuracy and content of information extracted from a recording, which, in turn, requires retaining the amplitude and phase information in order to keep the clinically relevant features with high noise attenuation. Equally important, ECG compression techniques are desirable due to the huge amounts of digital data generated by ECG monitoring devices, Holters and wearables. DCT [106] is a transformational compression approach which expresses an input signal in terms of a sum of cosine functions having different frequencies and has been used for audio [107] and image compression to reduce the data transmission bandwidth and storage size on disk. Also, DCT has been combined with DWT and other data reduction schemes to maximize the level of biomedical signal compression specifically ECG signals [108].

This algorithm presented a procedure comprising of both compression and denoising using DCT and then test the noise cancellation capability by simultaneously processing the uncompressed and compressed but somewhat distorted signal through SBMM. The results are reported as a trade-off between the SNR and compression ratio (CR) and it is shown that a suitable parameter selection for both leads to a good SNR with less distortion so as not to lose clinically important information while

reducing data size on disk.

5.2 Discrete Cosine Transform compression model

Data consisted of 122 out of 168 two-channel recordings from the "MIT-BIH ECG Compression Test Database" [61, 60] of approximately 20 seconds each sampled at 250 Hz with signal voltage range of ±10 mV primarily bandpass-filtered from 0.1 to 100Hz. Data were scrutinized on the basis of heart rate between 50 and 100 beats per minute and used as raw input data. This scrutiny is applied because the recording strips include a wide variety of ventricular, atrioventricular junctional and complex atrial arrhythmic beats as well as distortions due to conduction abnormalities and other noise sources and SBMM is a beat-based algorithm yet proven applicable to only normal sinus rhythm (NSR) beats [4, 58, 39]. The number of NSR records obtained after mean heart rate thresholding is consistent with the number of NSR records reported by [109] for the same database. All 20 second ECG records used for the evaluation of currently proposed algorithm were recorded through a Holter monitor, which is a challenge since the signal quality degradation is higher due to the analog recording process and allows testing the capacity of a compressor to preserve the subtle features of the ECG needed for accurate diagnosis.

The first step involves retaining useful ECG frequency band using a bidirectional $3^{rd}-$order Butterworth band-pass filter with cut-off frequency range of 0.5Hz to 40Hz. Baseline was computed as a cubic spline interpolation of fiducial points, placed 90 milliseconds before R-peaks, and subtracted from the ECG. The second step after preprocessing is the computation of DCT for the uncompressed noisy ECG record $x_{uc}(n)$, with n ∈ [0, N-1], using Equation−(5.1):

$$X_{uc}(k) \triangleq \begin{cases} \sum_{n=0}^{N-1} 2x_{uc}(n) \cos \frac{\pi k}{2N} (2n+1), & k \in [0, N-1] \\ 0, & else \end{cases} \tag{5.1}$$

$X_{uc}(k)$ being a series of cosine frequency components of the uncompressed and noise-corrupted ECG record arranged in descending order. Next, we calculated the least number 'M' of coefficients (with M<N) from the DCT sequence obtained in Equation−9.12 that represents a predefined E% (99, 95 and 90) in $x_{uc}(n)$, with E%, calculated in Equation−(5.2):

$$\%E = \frac{\sum_{k=0}^{M-1} |X_C(k)|^2}{\sum_{k=0}^{N-1} |X_{UC}(k)|^2} \times 100 \tag{5.2}$$

The reconstruction of the signal was then performed using these selected 'M' DCT coefficients in the inverse DCT as in Equation−(5.3):

$$x_c(n) \triangleq \begin{cases} \frac{1}{M} \sum_{k=0}^{M-1} w(k) X_c(k) \cos \frac{\pi k}{2M} (2n+1) & n \in [0, M-1] \\ 0 & else \end{cases} \tag{5.3}$$

where $x_c(n)$ is quantized to be stored into 6, 8 and 10 number of bits (the original

signal comprising 12-bit storage).

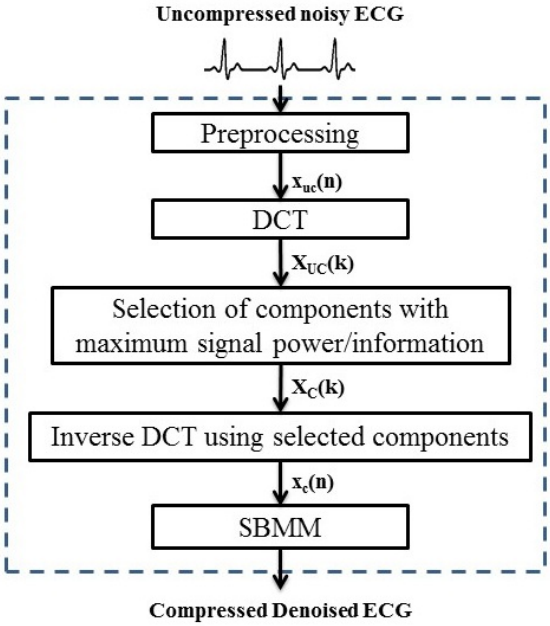

Figure 5.1: Flowchart of DCT-SBMM

R-peak positions are detected again from $x_c(n)$. Then, $x_c(n)$ plus recalculated R-peak positions are used to identify all cardiac cycles (CC) assuming the start of CC fiducial mark as 80 milliseconds before each R-peak. Each CC is then segmented into QRS (80 millisecond fiducial mark before and after each R-peak) and TUP (80 millisecond after each R-peak to 80 milliseconds before the next consecutive R-peak) segments. After CC segmentation, a resampling of TUP segments is performed to match the TUP length of median CC of all beats in a single recording. A median operation is performed over all the equal-length CCs to compute a representative beat. Finally, a representative ECG record is constructed using repetitions of median CC. Finally, the compressed noisy segmented CC are resampled back to their original lengths to retain the beat-to-beat morphological variability to obtain a compressed noise-free ECG signal. Figure−5.1 shows flow diagram for the proposed DCT-compressed SBMM (DCT-SBMM). For evaluating the performance of DCT-SBMM, SNR was computed in both $x_{uc}(n)$ and $x_c(n)$ by using SBMM for noise computation as in [4]. CR was calculated in terms of number of bits required to store data in uncompressed and compressed signal as in Equation−(5.4):

$$CR = \frac{Number\ of\ bits\ in\ x_{uc}(n)}{Number\ of\ bits\ in\ x_c(n)} \tag{5.4}$$

Differences between SNR before and after DCT-SBMM processing have been evaluated by using paired Student's t-test with two-sided significance level set at 5% ($p < 0.05$). Values are reported as mean ± standard deviation over the 122 records,

unless otherwise specified.

5.3 Compression vs. denoising trade-off

Average number of DCT coefficients respectively needed for the 99, 95 and 90 % energy levels were 270, 141 and 86, which constitute 5.3, 2.7 and 1.7 % of the total number of calculated DCT coefficients used for reconstruction of $x_c(n)$.

Table−5.1 shows the SNR values obtained before and after DCT-SBMM processing of ECG records. The algorithm was tested using variation in parameters CR and E% of $x_c(n)$. The SNR of $x_c(n)$ not significantly decreased by 0.925, 0.974 and 1.31 dBs as compared to that of $x_{uc}(n)$ when used E% was 99% represented by 1.7% of total number of DCT coefficients with compression ratios 1.2 (10-bit), 1.5 (8-bit) and 2 (6-bit) respectively. Instead, on the tests conducted for E% of 95% and 90%, there was a significant reduction in number of DCT coefficients used for reconstruction. Specifically, the SNR of $x_c(n)$ significantly decreased by 2.570, 2.595 and 2.781 dBs as compared to that of $x_{uc}(n)$ when used E% was 95% represented by 2.7% of total number of DCT coefficients with compression ratios 1.2 (10-bit), 1.5 (8-bit) and 2 (6-bit) respectively. The SNR of $x_c(n)$ significantly decreased by 4.057, 4.063 and 4.186 dBs as compared to that of $x_{uc}(n)$ when used E% was 95% represented by 5.3% of total number of DCT coefficients with CRs 1.2 (10-bit), 1.5 (8-bit) and 2 (6-bit) respectively.

Table 5.1: Performance Metrics

SNR Uncompressed	SNR Compressed			
	%E	CR = 1.2	CR = 1.5	CR = 2
6.80±5.59	99	5.87±3.81	5.82±3.81	5.49±3.74
	95	4.23±4.25[1]	4.20±4.22[1]	4.02 ±4.10[1]
	90	2.74±5.09[1]	2.73±5.05[1]	2.61±4.85[1]

Figure−5.2 shows a plot of 10 seconds of an example record '12713_03' from the processed database. Figure−5.2 (a) is compressed with respect to the uncompressed signal before SBMM quantized to 6 bits, hence shows the amount of distortion that occurs due to DCT compression and quantization. Figure−5.2 (b) shows the uncompressed/original signal processed through SBMM and the denoised output. Figure−5.2 (c) shows the compressed/reconstructed signal processed through SBMM and the denoised output. Figure−5.2 (d) shows the uncompressed, denoised signal compared with compressed, denoised signal obtained after processed through SBMM.

5.4 Discussion on achieved results

The DCT-SBMM algorithm proposed in the present study represents an extension of the previously published SBMM [4, 39]; specifically, it represents an initial study

for usage of DCT-SBMM in ambulatory and long-term monitoring conditions using compressed sensing. An average SNR of 5.49 and 4.56 dBs is observed with an average overall decline of 0.99 (14.5%) and 1.68 (37.9%) dBs as compared to the uncompressed signal for 99 and 95% energy levels representing processing with minimum signal distortion when quantized at 6 bits for signal storage providing maximum compression advantage. At 90% energy level, SNR for the processed signal has dropped to below an acceptable level i.e on average 2.69 dBs, showing a 4.11 (60%) dBs decline as compared to the uncompressed signal, hence even if the number of bits are reduced, the signal is too distorted or too noisy to provide any useful information. A trade-off is observed between SNR and CR produced by DCT-SBMM. At 99% reconstructed/compressed power signal, least SNR reduction is reported as compared to uncompressed signal. Similarly, at 90% power signal, highest reduction in SNR is observed which is not required since the CR is too high and signals are distorted. As a consequence, it is suggested to use a 95% power signal with 8 and 6-bit storage to get less storage capacity yet producing a good SNR output having lost least amount of useful information in the compression process.

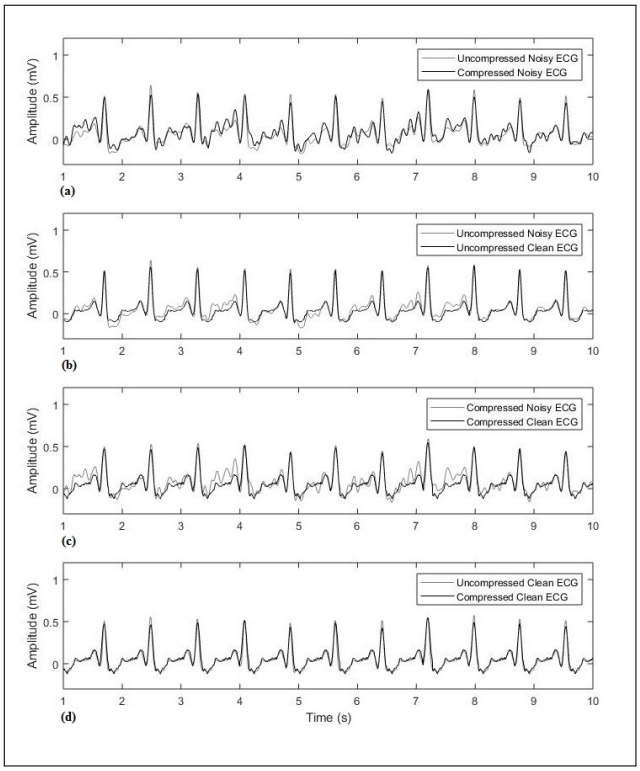

Figure 5.2: shows, as an example, 10 seconds of ECG record '12713_03' from "MIT-BIH ECG Compression Test Database": (a) uncompressed vs compressed noisy input, (b) noisy vs clean signal for uncompressed (c) noisy vs clean signal for compressed input before and after SBMM processing, and (d) uncompressed (12-bit) vs compressed (6-bit) denoised output.

A comparatively high standard deviation in all calculations is observed due to

the analog recording process of the used database making the compression testing more stringent than necessary [109] and occurrence of different kinds of abnormal beats in about 10% of the records processed. Moreover, it is observed that for too noisy input records, peak detection becomes difficult and results in some additional but wrong peaks, which again is a limitation in producing high SNR values whilst keeping useful signal information intact.

From Figure−5.2, it is visible that the compressed ECG signal is quite distorted and in some cases of very noisy signals there are small noisy peaks enhanced after compression. Figure−5.2 (b) and (c) shows that the input in uncompressed and compressed form are quite different due to distortion but the denoised or clean signal obtained in both cases has a somewhat similar morphology and no critically important and distinguishing features are lost. It is visibly clear from Figure−5.2 (d) that SBMM produces almost the same output for both uncompressed and compressed ECG, while providing an advantage of 50% reduction (CR=2) in storage size. The presented DCT-SBMM proves to be efficient in terms of both compression and denoising and hence is applicable to ambulatory, online and wearable sensing applications to be used for long-term and continuous monitoring of patient ECG by the clinicians. The best compromise between signal denoising and signal compression is obtained by maintaining 95% energy with a quantization 6-bit data storage.

Chapter 6

GPU-based Segmented Beat Modulation Method

6.1 Sport-related sudden cardiac death

Sport-related sudden cardiac death (SRSCD) occurs in the presence of underlying cardiovascular diseases, some of which may be identified by processing ECG recordings acquired during training (TECG), eventually using wearable devices [110]. According to data, the probability of the ECG to detect underlying cardiovascular abnormalities that could place the athlete at risk of SRSCD is superior to that of physical examination and history [111, 112]. However, TECGs in the acquired raw form are affected by several additional noise factors such as electrode motion artefacts, muscular artefacts emanating from intense and regular physical activities like running, walking, gym training etc. that can make the signal of interest clinically useless [113]. Additionally, the transmission of large amount of TECG data consumes a great deal of energy and reduces the battery life of both the wearable device and the processing platform [114]. To extend battery life, high-end processing platforms are required to have in-time identification and alert generation for prevention of SRSCD. The SBMM [4, 58] provides a template-based ECG filter with physiological heart-rate and morphological variability. The highly parallelizable and independent nature of data processing with SBMM makes it suitable to be implemented on high performance computing programming structures and platforms. A CPU based approach uses single instruction single data (SISD) programming structure executing one program statement operating on one data stream at a time. Whereas, GPU architecture is characterized by single instruction multiple data (SIMD) feature [115], which allows operations on multiple data points simultaneously. GPU provides a high-performance hardware platform for faster simulations. Thus, in this work, GPU-based SBMM (GPU-SBMM) is implemented as performance improved version of the previously proposed SBMM (which is originally CPU-based) for the denoising of TECG data.

6.2 GPU-based vectorization model

GPU-SBMM was implemented in MATLAB using Parallel Computing Toolbox built-in functions. GPU-SBMM takes as input the noisy TECG signal, the R-peak positions vector and some initial settings (TECG sampling frequency and gain). Each cardiac cycle, which in GPU-SBMM can be processed independently from the others, was segmented into QRS and TUP segments. After the segmentation of cardiac cycles into QRS and TUP segments, a resampling of TUP segments is performed to match the TUP length of median CC (mCC) of all beats in a single recording. A peak correction is applied to identify and correct falsely detected peaks. Finally, GPU-SBMM performs a filtering procedure that reconstructs a clean TECG signal from the one corrupted by noise recording. All the for-loops for segmentation, modulation, correlation optimization and reconstruction steps are implemented as vectorized cell array. The computed clean TECG from the GPU processor is then sent back to CPU using 'gather()' function. The distribution of workload for GPU-SBMM is shown in Figure−6.1.

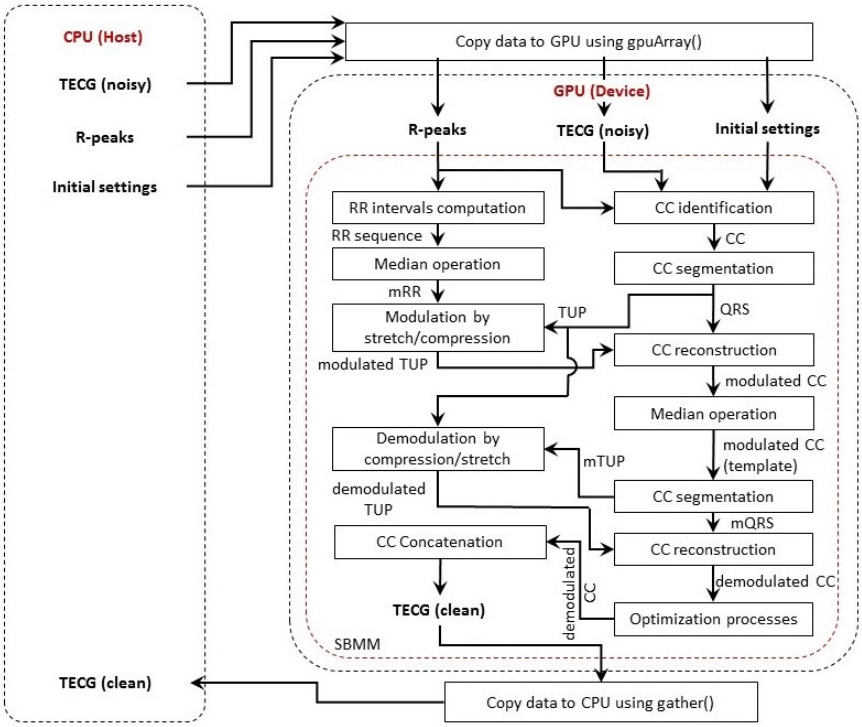

Figure 6.1: Distribution of workload for GPU-based segmented-beat modulation method.

Single-channel TECG recordings (sampling frequency: 256 Hz) from 8 subjects (3 male, 5 female), aged 22-32 years (mean 26.5±5.5 years) were used. Measurements were taken using a wearable ECG monitoring device Actiwave (CamNtech, Cambridge, UK) placed on the chest while participants were asked to perform one or more

exercise tasks (walk, run, low-resistance bike (LRB) and high-resistance bike (HRB)) characterized by low HR for walking to high HR for running, LRB and HRB exercises.

Data were taken from the "Wrists PPG During Exercise" database by Physionet [116] All TECG recordings were band-pass filtered through a bidirectional $3^{rd}-$order Butterworth filter with cut-off frequencies of 0.5Hz and 40Hz. After that, the baseline was removed. Baseline was computed as a cubic spline interpolation of fiducial points, placed 90ms before R-peaks. Annotations of the reference TECG R-peak positions were provided in the Physionet database. The mean HR and HRV (measured as RR-interval standard deviation) was 104±25 bpm and 54±26 ms, respectively. All GPU experiments were performed on NVIDIA GeForce GT 740M processing machine with compute capability 3.5 based on the Kepler architecture and 64GB GPU memory with bandwidth of 173 GB/s. All CPU experiments were performed on Intel® Core i5 with 2 cores and an operating frequency of 1.8 GHz. To quantify the reliability of the GPU-SBMM in reducing the level of noise affecting the TECG signals, the SNR expressed in decibel (dB) was computed before (noisy) and after (clean) GPU-SBMM processing according to eq−6.1:

$$SNR(dB) = 10\log_{10}[(\frac{A_{Signal}}{A_{Noise}})^2] \tag{6.1}$$

where A_{Signal} (mV) is the signal amplitude and A_{Noise} (mV) is the noise amplitude. Amplitudes of TECGs being close to deterministic (pseudo-periodic) signals, were computed as mean of the maximum-minus-minimum values over the beats. Whereas, amplitudes of noise signals being close to Gaussian stochastic signals were computed as 4 times standard deviation [40]. All amplitude values were computed over the entire length of the study records. For each TECG signal, GPU-SBMM runtime ($t_{GPU-SBMM}$, s) was computed. Moreover, each TECG signal was processed with the sequential SBMM implementation [4] and the SBMM runtime (t_{SBMM}, s) was computed. To show the effect on performance after GPU resource enhancement, speedup factor (Speedup(x)), defined by Amdahl's law [117] as an improvement in the speed of execution of a task on two computing architectures with different resources, was computed for each TECG signal using eq−6.2:

$$Speedup(x) = \frac{t_{SBMM}}{t_{GPU-SBMM}} \tag{6.2}$$

Differences between SNR before and after GPU-SBMM processing have been evaluated by using a paired Student's t-test. Values are reported as mean±standard deviation, unless otherwise specified. The two-sided significance level was set at 5% ($p<0.05$).

6.3 Speedup and signal-to-noise ratio assessment

An example of the TECG signal recorded during exercise before and after GPU-SBMM processing is shown in Figure−6.2 (panel a). SNR values for each activity before and after GPUSBMM processing are given in Table−6.1. Mean SNR values computed for all noisy TECG and clean TECG signals were 1±5 dB and 19±5 dB, respectively; a significant increase ($p < 10^{-12}$) in SNR was observed after GPU-SBMM processing. Stratifying for each exercise task, a significant increase in SNR was also found Table−6.1. The calculated SBMM and GPU-SBMM runtimes are shown in Figure−6.2 (panel b).

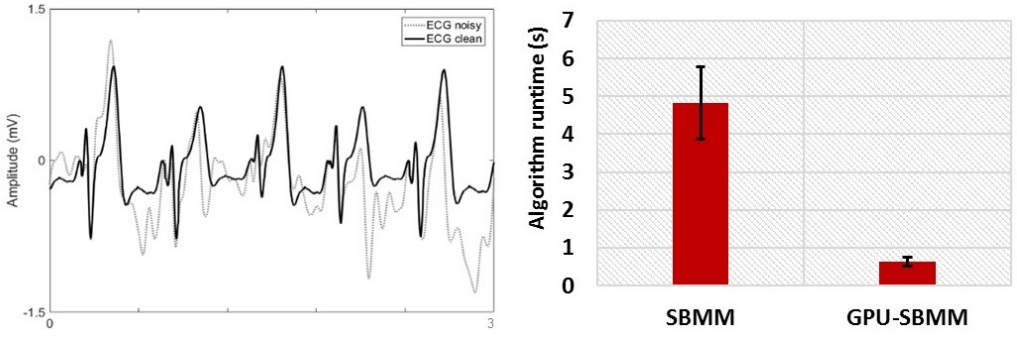

(a) (b)

Figure 6.2: Results achieved for GPU-SBMM a) TECG plotted for the exercise task High Resistance Bike for duration of 3 seconds, b) Runtime for CPU-based SBMM and GPU-based SBMM on NVIDIA GeForce GT 740 processor.

Table 6.1: Comparative evaluation of SNR by activity.

Exercise tasks	No. of TECGs	Before SNR (dB)	After SNR (dB)
Walk	6	-2±3	18±5
Run	5	1±7	20±7
Low Resistance Bike	5	3±5	20±5
High Resistance Bike	3	3±6	20±6

6.4 Discussion on achieved results

The GPU implementation reduces the runtime of the noise reduction algorithm from 4.82 s to 0.63 s. Hence, the speedup achieved is 7.67 times higher than that of the CPU-based SBMM implementation. Improvement in SNR showed that GPU-SBMM is an effective and fast method for removal of exercise-induced noise factors in the TECG data. Comparative testing showed that the average speedup achieved for the four training activities is 7.67x. Offloading the heavy part of computation to the GPU processor which can either be a mobile platform or a desktop, the performance of

the algorithm is increased. This allows an effective processing and analysis of TECG signals measured from wearable sensors through innovative software applications for the prevention of SRSCD [110]. For future recommendation, full benefits of parallelism for GPU-SBMM might be seen when used with big data (larger datasets or online ECG data processing). Moreover, a high denoising efficiency with TECGs makes GPU-SBMM a useful method for a wearable ECG sensing apparatus/setting. GPU-SBMM is an efficient and accurate algorithm for filtering TECG, typically affected by high level of noise. Thus, it represents a potentially useful tool to fight SRSCD.

Chapter 7

Dynamic-template Segmented Beat Modulation Method

7.1 Design variables for wearable ECG sensing devices

The wearable sensors can be diagnostic tools for self-monitoring important physiological signals at home. This type of sensors such as inertial sensors, cameras and medical devices are having great success in Ambient Assisted Living (AAL) applications [118]. Among these, wearable electrocardiogram sensing devices are essential for continuous and automatic monitoring of the heart. ECG signals acquired from wearable devices are particularly corrupted by baseline wander, power line interference and motion artifacts. Moreover, there exist a number of variations due to sensor-type such as placement (wrist, chest, other), electrode type (wet, dry) and coupling (AC, DC) etc. A large number of ECG datasets are available today [Physionet, AHA], most of which are clinical ECG data. Unfortunately, none of these datasets focus on wearable ECG applications, that is to say, no special attention has been paid to the unique conditions in wearable ECG computers, such as interference or electrode type, placement, and coupling. Therefore, a dataset focusing on the wearable applications will be highly significant for analyzing the various signal characteristics, guiding design decisions for a wearable system. This dataset also provides the opportunity to the algorithm researchers to consider real-world data in their algorithm design and evaluation. This work includes using SBMM filtering for wearable ECG sensors specifically using motion artifact induced noise data from [119]. The dataset represents real-world signals and noise which makes it unique and also challenging to identify and remove corrupted signal features. The results are presented in terms of SNR improvement as done in [120]. Hence the utility of SBMM is tested in terms of denoising ECGs acquired by wearable sensors contaminated by various motion artifacts.

7.2 Heart-rate adaptation model

All ECG records were pre-processed by applying a bidirectional 3rd-order band-pass Butterworth filter with cut-off frequencies of 0.5Hz and 40Hz. R-peaks were calculated using standard peak detection algorithm. Further, baseline was approximated by

cubic spline interpolation of fiducial points placed 90ms before R-peaks.

For mathematical understanding for signal processing algorithm, we denote the noisy input ECG signal by ecg_{noisy} and the output clean ECG signal obtained after filtering ecg_{clean}. R-peak positions r_p are detected from ecg_{noisy} using Pan-tompkin's peak detector. r_p is then used to calculate number of beats per minute, in other words HR and then divided by 3 to get number of beats per 20 seconds. Then, r_p are used to identify all CCs assuming the start of CC fiducial mark as 80 milliseconds before each R-peak. ecg_{noisy} is then divided into segments containing number of beats per 20 second. The number of sections according to eq. (7.1):

$$\#sections(n) = \frac{Total\ number\ of\ beats}{Number\ of\ beats\ in\ 20\ seconds} \tag{7.1}$$

$ecg_{noisy}(i)$ is section-wise processing of each 20 second portion of ecg_{noisy}, where: i = 1, .., n. Each CC from $ecg_{noisy}(i)$ is then segmented into QRS (80 millisecond fiducial mark before and after each R-peak) and TUP (80 millisecond after each R-peak to 80 milliseconds before the next consecutive R-peak) segments. After CC segmentation, a resampling of TUP segments is performed to match the TUP length of median CC of all beats in a single recording. A median operation is performed over all the equal-length CCs to compute a representative beat. Finally, a representative ECG record is constructed using repetitions of median CC. Finally, the input noisy segmented CC are resampled back to their original lengths to retain the beat-to-beat morphological variability to obtain a clean noise-free ECG signal $ecg_{clean}(i)$. In the end all 20 second sections are concatenated to get ecg_{clean}. Figure−7.1 shows flow diagram for the proposed dynamic-template SBMM.

7.3 Validation study for motion artifact corrupted data

Data [119] was acquired using a customized patch-based bio-sensor device which includes an MSP430 microcontroller, and a TI ADS1299 AFE with very low input-referred noise to maintain the original signal to the utmost possibility. 5 subjects, 2 coupling methods and 7 activities making a total of 70 ECG records with duration 90 to 210 seconds each were used for testing the proposed algorithm. Sampling rate was set to 488 Hz and 24-bit resolution was used for minimum quantization error. The simulated data includes recorded 8 activities related to motion artifacts and patch-based wearable device: 1) drinking coffee; 2) typing the keyboard; 3) pressing and releasing the signal electrode; 4-5) walking at 1 and 3 mph; 6-7) running at 5 and 7 mph. The mean HR and HRV was measured as RR-interval standard deviation for all activities and is reported in Table−7.1.

The robustness of the proposed algorithm is assessed in terms of SNR improvement assuming high (-5 dB), medium (0 dB) and low (5 dB) levels of input noise following

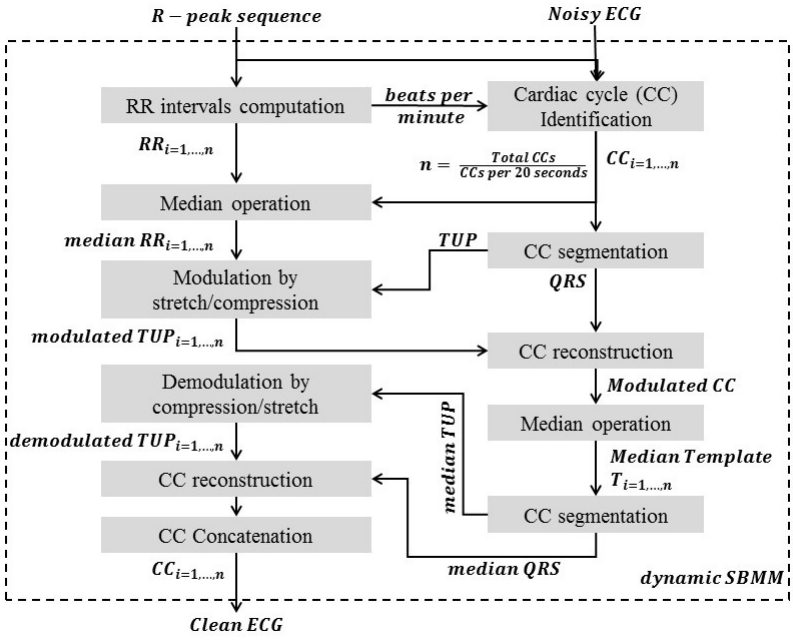

Figure 7.1: Flow Diagram of the proposed dynamic-template SBMM

Table 7.1: Mean HR over 5 subjects stratified for 7 activities

Activities	**Coupling method**	
	DC	***AC***
Drinking coffee	83.4 (0.12)	104.6 (0.16)
Typing keyboard	98 (0.12)	99.6 (0.10)
Pressing and releasing signal electrode	91 (0.13)	95.2 (0.17)
Walking at 1 mph	88.4 (0.08)	87.4 (0.08)
Walking at 3 mph	104.2 (0.13)	95.2 (0.09)
Running at 5 mph	127.6 (0.19)	124.2 (0.18)
Running at 7 mph	132.4 (0.19)	134 (0.23)

[120] calculated as in Equations−(7.2) and (7.3):

$$SNR_{imp}(dB) = SNR_{out} - SNR_{in} \tag{7.2}$$

$$SNR_{out} - SNR_{in} = 10log(\frac{\sum_i |x_n(i) - x(i)|^2}{\sum_i |x_d(i) - x(i)|^2}) \tag{7.3}$$

Differences between SNR before and after dynamic-template SBMM processing have been evaluated by using an SNR improvement criteria. Values are reported as average (max), unless otherwise specified. The values represent average SNR improvement calculated over all 5 subjects for all figures reported.

7.4 Discussion on achieved results

SNR improvement values are reported assuming input values of -5dB, 0dB and 5 dB which represent a high, medium and low amount of input noise subtracted from output SNR obtained after dynamic-template SBMM filtering. Mean and maximum improvement SNR computed for all ECG records is reported in Table−7.2 (DC coupling) and Table−7.3 (AC coupling) stratified with respect to all activities. Highest mean SNR_{imp} is observed for the subjects drinking coffee i.e 8.19 dBs. The mean SNR_{imp} values decrease as the level of activity increases. The mean SNR_{imp} is observed to be particularly low while pressing and releasing the signal electrode due to increase in movement not from the body but sensing device. Lowest mean SNR_{imp} is observed for running at both 5 and 7 mph due to high amount of motion noise. Input noisy and output clean ECG signals for all 7 simulated activities are shown in Figure−7.2.

The present study presents dynamic-template SBMM as an improved version of SBMM considering motion artifacts induced during different daily life activities. The analysis done using -5, 0 and 5 dBs of input noise show that the highest level of denoising is achieved when the level of input noise is high (-5dB), good noise cancellation when the input signal is assumed to contain an average level of noise and least SNR improvement when the level of noise is low. For AC and DC coupling cases, the algorithm shows a good enough denoising for high level of input noise (-5dB) but shows a poor signal denoising in case of medium (0dB) and low (5dB) levels of input noise. The activity-wise analysis for the proposed algorithm shows a good SNR improvement for activities 1-5 but for the activities highly disrupting the input signal i.e walking at relatively high speed (3 mph), running both at 5 and 7 mph, the reconstructed signal shows a negation of noise as well as useful signal.

Table 7.2: Performance evaluation of proposed algorithm. Values show SNR improvement in Decibels in case of DC coupling

Activities	**SNR Improvement, dBs**		
	DC (Subject 1 - Subject 5)		
Input SNR, dBs	**-5**	**0**	**5**
Drinking coffee	8.19 (18.94)	3.19 (13.91)	-1.80 (8.94)
Typing keyboard	3.14 (5.68)	-1.85 (0.71)	-6.85 (-4.28)
Pressing electrode	1.53 (10.41)	-3.42 (5.41)	-8.46 (0.44)
Walking at 1 mph	2.67 (7.52)	-2.32 (2.52)	-7.32 (-2.47)
Walking at 3 mph	-0.14 (4.25)	-5.14 (-0.74)	-10.14 (-5.71)
Running at 5 mph	-2.52 (-0.19)	-7.52 (5.19)	-12.41 (-10.12)
Running at 7 mph	-2.74 (-0.20)	-7.71 (-5.23)	-12.74 (-10.38)

We can conclude that the dynamic-template SBMM algorithm proves to be efficient in terms of improvement in SNR and hence is applicable to wearable sensing for ambulatory and online ECG monitoring in IoT health-care applications.

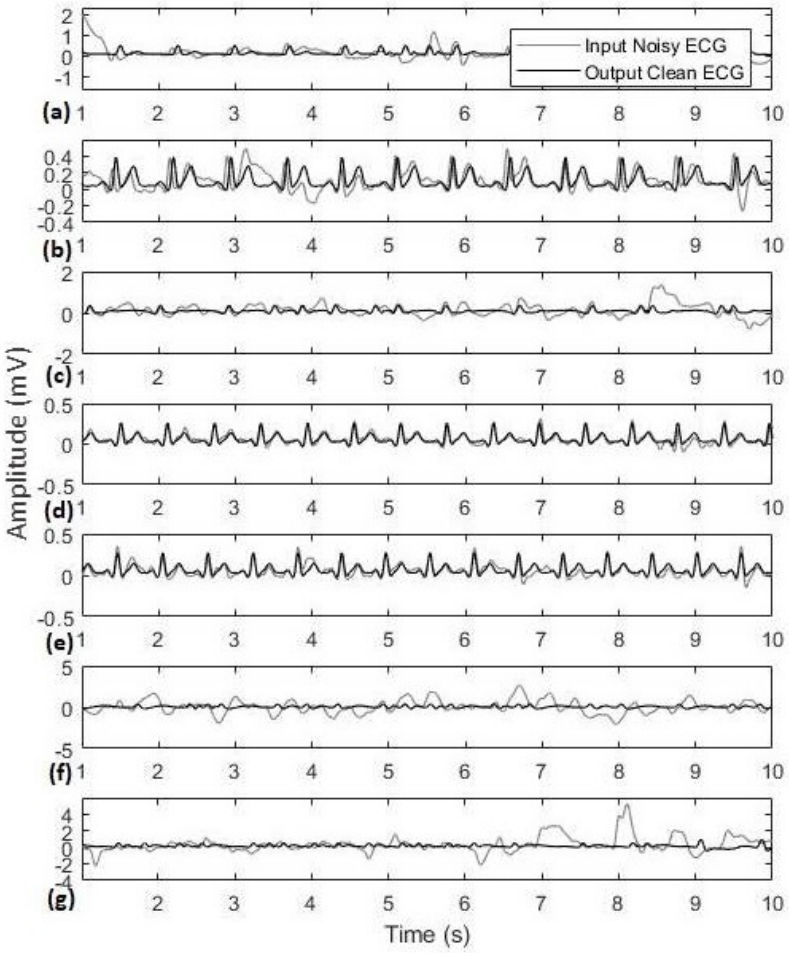

Figure 7.2: Noisy and dynamic-template SBMM filtered ECG 10 second records for a) drinking coffee, b) typing keyboard, c) pressing and releasing electrode, d) walking at 1 mph, e) walking at 3 mph, f) running at 5 mph and g) running at 7 mph for Subject 1 using patch-based wearable ECG sensor with DC coupling

Table 7.3: Performance evaluation of proposed algorithm. Values show SNR improvement in Decibels in case of AC coupling

Activities	**SNR Improvement, dBs**		
	AC (Subject 1 - Subject 5)		
Input SNR, dBs	**-5**	**0**	**5**
Drinking coffee	0.21 (8.77)	-4.78 (3.72)	-9.78 (-1.22)
Typing keyboard	3.67 (8.27)	-1.32 (3.25)	-6.32 (-1.71)
Pressing electrode	-2.34 (1.33)	-7.37 (-3.66)	-12.37 (-8.66)
Walking at 1 mph	8.16 (14.51)	3.16 (9.53)	-1.83 (4.59)
Walking at 3 mph	5.06 (11.70)	0.06 (6.72)	-4.93 (1.70)
Running at 5 mph	-3.55 (1.93)	-8.62 (-3.06)	-13.31 (-8.06)
Running at 7 mph	-6.24 (-0.62)	-11.47 (-5.69)	-16.24 (-10.81)

Chapter 8

Differential Evolution-based feature optimization of ECG signals

8.1 Overview of the problem

Computer-aided ECG arrhythmia diagnosis (CAD) systems are popular nowadays that use intelligent techniques for the development of smart healthcare monitoring platforms. ECG signals acquired in raw form suffer from multiple noise factors such as PI, EMA and MA. There is still a need to remove the redundant/corrupted data points or features that survive a generalized preprocessing procedure. A CAD ECG arrhythmia classification system usually involves a feature extraction process in which a set of features is calculated for each individual heartbeat (the type of features used might be hand-crafted, statistical, morphological or spectral etc.) and classifier construction to learn the features and classify incoming heartbeats. Using all the features calculated in the feature extraction step and a multi-layered classifier not only introduces heavy computational cost but also affects classifier performance due to the presence of redundant/corrupted features. Latest systems deploy a feature reduction/optimization step before classification to remove all unnecessary features. This also allows the use of a single layered or a computationally less intensive learning algorithm for classification. Therefore, to extract sufficient features and reduce their dimensions for classifiers to achieve optimal classification results is the primary task in the design of latest ECG arrhythmia classification systems.

Particularly DE has been used in a multitude of CAD-based ECG applications, for example optimization of extended Kalman smoother parameters for efficient noise reduction especially for real muscle artifact noise [121], P and T wave detection and delineation of ECG signal [122], extraction of fetal ECG from single channel abdominal ECG signal using DE optimized extended Kalman smoother [123], extensive usage of DE to optimize the different neural network architectures for ECG signal classification like extreme learning machines [124], Gaussian process models [125], optimizing voting mechanism for ensemble [126], Naive Bayes [127] etc.

8.2 Latest CAD arrhythmia systems

In the latest competitive research, novel features and various classifiers have been utilized for ECG beat classification tasks. Sayantan et al. [128] feature representation of ECG is learnt using Gaussian-Bernoulli deep belief network followed by a linear support vector machine (SVM) training in the consecutive phase. Elhaj et al. [129] investigated principal components of discrete wavelet transform coefficients and higher order statistics. Afkhami et al. [130] used parameters of Gaussian mixture modeling together with skewness, kurtosis and 5^{th} moment and applied an ensemble of decision trees to classify the heartbeats using class-oriented scheme. Liu et al [131] improved the dictionary learning algorithm for vector quantization of ECG. Shen et al [132] used wavelet transform-based coefficients, signal amplitude and interval parameters. A new classifier, which integrates k-means clustering, one-against-one SVMs, and a modified majority voting mechanism, is proposed to further improve the recognition rate for extremely similar classes. Qin et al. [133] developed wavelet multi-resolution analysis to extract time-frequency domain features and applied one-versus-one support vector machine to characterize six types of ECG beats. Zhai [134] and Acharaya et al. [54] used a CNN classifier. Oh et al. [135] used CNN and LSTM in combination to propose a refined classification method. Generated synthetic data to overcome imbalance problem. Accuracy of 94.03% and 93.47% with and without noise removal respectively.

Recently, researchers have presented different feature reduction methods to reduce input dimensions of ECG signals for neural classifiers. To name a few latest, Zhang et. al [136] extracted statistical features applying combined method of frequency analysis and Shannon entropy and used information gain criterion to select 10 highly effective features to obtain a good classification on five types of heartbeats. Yildrim et. al [137] implemented a convolutional auto-encoder based nonlinear compression structure to reduce the feature size of arrhythmic beats. Tuncer et. al [138] applied neighborhood component analysis feature reduction technique to obtain 64, 128 and 256 features from a 3072 feature vector size. Wang et al [139] proposed effective ECG arrhythmia classification scheme consisting of a feature reduction method combining principal component analysis with linear discriminant analysis. Alonso-Atienza et al. [140] used a filter-type feature selection procedure was proposed to analyze the relevance of the computed parameters. Chen and Yu [141] applied nonlinear correlation-based filters, calculated feature–feature correlation to remove redundant features prior to the feature selection process based on feature–class correlation. Asl et al. [90] The proposed feature reduction scheme based on generalized discriminant analysis. Haseena et al. [142, 143] used a fuzzy C-mean (FCM) clustered PNN for the discrimination of eight types of ECG beats. The performance has been compared with FCM clustered multi layered feed forward network trained with back propagation algorithm. Important parameters are extracted from each ECG beat and feature reduction has been carried out using FCM clustering. Polato et al. [144] used

principal component analysis. Genetic algorithms have also been applied recently for the optimization of ECG heartbeat features [126, 145, 146, 147] and proved to be advantageous in improving the time-cost value in heartbeat classification methods.

Furthermore, existing multi-class learning approaches mainly focus on exploiting label correlations to facilitate the learning process. However, an intrinsic characteristic of multi-label learning, i.e., class-imbalance [148] has not been well studied [149, **?**, 150]. Matthew's correlation coefficient (MCC) was first used by B.W. Matthews for the performance assessment of protein secondary structure prediction [151]. Since then it has become a widely used performance measure in biomedical research. MCC and Area Under ROC Curve (AUC) have been chosen as the elective metric in the US FDA-led initiative MAQC-II that aims to reach a consensus on the best practices for development and validation of predictive models for personalized medicine [152].

8.3 Differential Evolution

In evolutionary computation, Differential Evolution (DE) [153, 8] is a method that optimizes a problem by iteratively trying to improve a candidate solution with regard to a given measure of quality. Such methods are commonly known as metaheuristics as they make few or no assumptions about the problem being optimized and can search very large spaces of candidate solutions. However, metaheuristics such as DE do not guarantee an optimal solution is ever found. A basic variant of the DE algorithm works by having a population of candidate solutions (called agents). These agents are moved around in the search-space by using simple mathematical formulae to combine the positions of existing agents from the population. If the new position of an agent is an improvement then it is accepted and forms part of the population, otherwise the new position is simply discarded. The process is repeated and by doing so it is hoped, but not guaranteed, that a satisfactory solution will eventually be discovered. The main steps regarding DE design for feature selection are shown in Figure−8.1 and explained as under:

Representation of individuals

It is very important to choose an appropriate representation that adequately describes the type and size of the search space consisting of the set of all possible solutions. Particularly in case of feature selection and optimization problems, the chromosome is an indirect representation of a solution (called genotype) and a decoding process is needed to obtain the solution (called phenotype). This genotype binary population chromosome most is the set $0, 1$. However, many other individual representations include real-valued [154], permutations [155] etc. according to the nature of the optimization problem. Another key parameter is the length of the chromosomes. Their length could be fixed or variable and again is problem dependent. For the purposes of this document, we will assume a binary coded population individual

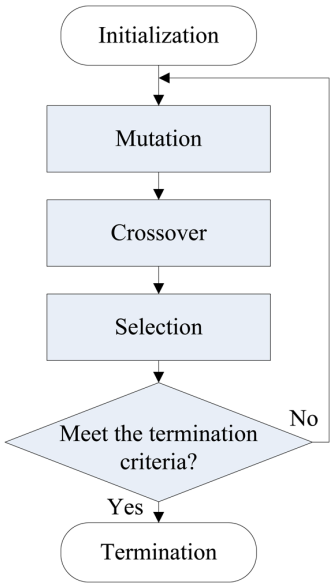

Figure 8.1: Basic architecture of Differential evolution [8].

representation and a fixed length $n \epsilon N$ for all the individuals in the search space.

Population of individuals

An EA executes an iterative process that improves a population of individuals with increasing number of generations. A population structure P(t) is defined to keep the current population of those individuals at time t ('t' represents the iteration number). P(t+1) might then represent the evolved population achieved in the next iteration.

Fitness Function

The stimulus of evolution means survival of the fittest individuals. To evaluate the fitness in this scenario, a measurement parameter should be designed. The fitness function assigns to each individual a real positive value that is used for the selection mechanism (next item) to guide the search in forthcoming iterations.

Selection

The selection procedure imposes a bias to the search process toward regions of high-quality solutions. The purpose of this step is to select the fittest individuals that will take part in the next phase.

Crossover and mutation

The crossover operation generates an offspring from the selected set of parents. Both crossover and mutation promote the investigation of the search space by creating offspring which inherit good genetic material from their parents. Thus, these operators

are expected to create, on average, individuals with higher quality with respect to their parents. A classical example of a crossover operator for binary chromosomes called 1–point crossover. The offspring inherits the first k bits from the first parent and the last nk bits from the second one. For example, given the crossover point $k = 3$ and two possible parents P1 and P2 as in Equations−(8.1) and (8.2), then the offspring P_{off} is produced as a result of crossover X_c as in Equation−(8.3):

$$P1 = (0\ 0\ 1\ |0\ 1\ 0\ 1\ 1\ 1),\ and \tag{8.1}$$

$$P2 = (1\ 0\ 0\ |1\ 1\ 1\ 0\ 1\ 0) \tag{8.2}$$

$$X_c(P1, P2) = P_{off} = (0\ 0\ 1\ |1\ 1\ 1\ 0\ 1\ 0) \tag{8.3}$$

Let l = 4 be the random location generated and P_{off} the individual then a bit-flip at location 4 produces mutation as in Equation−(8.4):

$$X_m(P_{off}) = (0\ 0\ 1\ |\mathbf{0}\ 1\ 1\ 0\ 1\ 0) \tag{8.4}$$

Termination

A termination condition specifies either that the fitness has reached its optimum value and is stagnant for a specified number consecutive iterations or that the maximum iteration count has reached. In this case, the optimum fitness value and the corresponding population individual that produced the optimum fitness is returned and the optimization process is terminated.

8.4 Probabilistic Neural Network

A probabilistic neural network (PNN) [9, 156] is a feedforward neural network, which is widely used in classification and pattern recognition problems. In the PNN algorithm, the parent probability distribution function (PDF) of each class is approximated by a Parzen window and a non-parametric function. Then, using PDF of each class, the class probability of a new input data is estimated and Bayes' rule is then employed to allocate the class with highest posterior probability to new input data. By this method, the probability of misclassification is minimized [157]. This type of artificial neural network was derived from the Bayesian network and a statistical algorithm called Kernel Fisher discriminant analysis [158]. In a PNN, the operations are organized into a multilayered feedforward network with four layers as shown in Figure−8.2:

1. Input layer: Each neuron in the input layer represents a predictor variable. The range of values is standardized by subtracting the median and dividing by

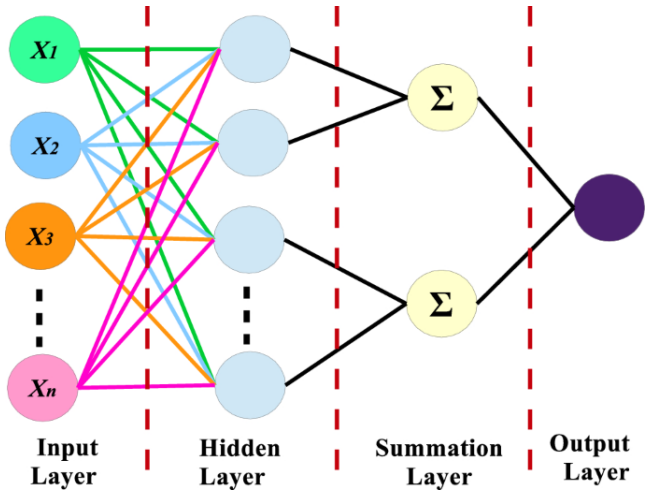

Figure 8.2: Basic architecture of PNN [9].

the interquartile range. Then the input neurons feed the values to each of the neurons in the hidden layer.

2. Hidden (Pattern) layer: This layer contains one neuron for each case in the training data set. It stores the values of the predictor variables for the case along with the target value. A hidden neuron computes the Euclidean distance of the test case from the neuron's center point and then applies the radial basis function kernel function using the sigma values.

3. Summation layer: For PNN there is one pattern neuron for each category of the target variable. The actual target category of each training case is stored with each hidden neuron; the weighted value coming out of a hidden neuron is fed only to the pattern neuron that corresponds to the hidden neuron's category. The pattern neurons add the values for the class they represent.

4. Output layer: The output layer compares the weighted votes for each target category accumulated in the pattern layer and uses the largest vote to predict the target category.

There are several advantages using PNN [156] such as the less number of layers and simpler computational structure makes PNNs much faster and accurate than multilayer networks. PNNs are relatively insensitive to outliers, generate accurate predicted target probability scores.

8.5 DE feature optimization design challenges

Differential evolution belongs to the group of evolutionary algorithms (EA) or evolutionary computation (EC) optimization techniques [159, 160, 161], inspired by the philosophies of evolution for optimal solution search and natural selection within

specific system constraints and present a viable solution to finding the best feature combination that optimizes a defined performance measure. Generally, an initial population is randomly created, called chromosomes. This population spanning the possible solution space will evolve, by means of an iterative process called generations. The performance of each individual is evaluated by using a "fitness function" which can be defined as a positive performance or a negative error function. In case of fitness function being defined as a performance parameter, a maximization of fitness function is carried out. In case of the fitness function being defined as a cost or error function, a minimization of fitness function is desired. The better solution represents how much a possible solution represented by the chromosome is good solution for the given problem. A new generation is produced by applying mutation and crossover operators, with specific mutation and crossover probabilities, respectively, on selected individuals presenting low values on their cost functions or high values for the performance functions. Convergence and robustness properties of EAs have been widely studied in the literature [159]. These properties depend on:

1. an appropriate individual chromosome coding,
2. an accurate problem-specific characterization of the fitness (performance or cost) function, and
3. adequate definition of genetic operators and selection method for crossover and mutation processes.

8.6 DE-PNN solution

This research models a metaheuristic search algorithm Differential Evolution (DE) to optimize direct ECG beat morphological features to maximize MCC for 8 arrhythmia beat classes having imbalanced and uncorrelated class distributions. The algorithm is tuned to find an optimum reduced combination of features that performs better as compared to all features. Classification using PNN is performed with optimum and all features to show the difference. Using PNN for classifying abnormal heartbeats using reduced direct signal features skips the computation of secondary features, produces higher classification performance due to removal of unnecessary features and faster due to reduced features and less time-consuming learning algorithm. The proposed methodology as graphically shown in Figure−**??** is explained in four steps; 1) preprocessing, 2) feature extraction and normalization, 3) DE feature optimization, and 4) Disease-based PNN classification as following:

8.6.1 Preprocessing

In the preprocessing stage, power and low-frequency components are removed from the raw ECG signal by using a 6^{th}-order bidirectional Butterworth band-pass filter

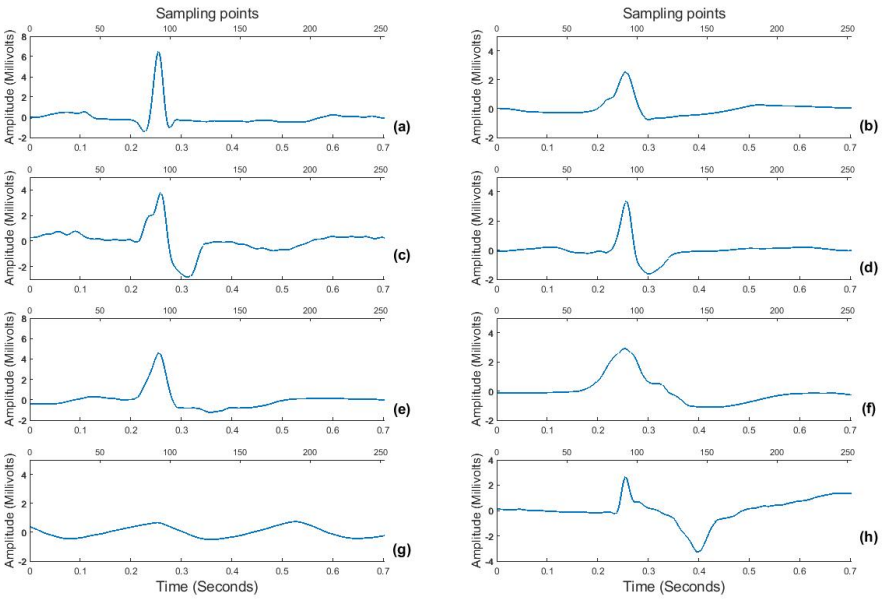

Figure 8.3: Sample beats for eight ECG beat classes: (a) NORM, (b) LBBB, (c) RBBB, (d) PVC, (e) PAC, (f) VESC, (g) VFLT and (h) PACE.

with lower and upper cut-off frequencies of 0.5 and 40 Hz respectively. Baseline is computed as a cubic spline interpolation of fiducial points placed 90 milliseconds before R-peak positions as an approximation for baseline PR-segment and subtracted from the bandpass-filtered signal.

8.6.2 Feature extraction and normalization

Using the R-peak positions provided with each record, a heartbeat sample is identified as having onset 250 ms before each R-peak position to 450 milliseconds after each R-peak position. This definition makes each heartbeat consist of 253 sampling points and ensures that the important characteristic points of ECG like P, Q, R, S and T waves are included [162]. The signal amplitude biases in the waveforms of the ECG beat samples are inconsistent due to instrumental and human errors. Hence, we utilize the Z-score method to reduce the above-mentioned differences in each ECG beat sample. Through the Z-score method, the mean value of each ECG sample is first subtracted from each ECG sample to eliminate the offset effect, and then divided by its standard deviation [139]. This procedure results in a normalized ECG beat sample with zero mean and unity standard deviation. Figure−8.3 shows samples for all 8 ECG beat classes used in this research.

8.6.3 DE Feature optimization

The mathematical model followed for feature optimization using DE to find the minimum number of features that result in maximum classification performance is

explained as follows.

Population Initiation

An initial population matrix $\mathbf{P}$ is generated as in Equation−8.5 to represent the possible solution/optimization space consisting of n_p number of binary row vectors $\mathbf{p}$ called population individuals each of length n_f (number of features in heartbeat samples in this case 200 as mentioned in subsection 8.6.2).

$$\mathbf{P}_{n_c,n_f} = \begin{bmatrix} \mathbf{p}_1 \\ \mathbf{p}_2 \\ . \\ . \\ \mathbf{p}_i \\ . \\ . \\ \mathbf{p}_{n_p-1} \\ \mathbf{p}_{n_p} \end{bmatrix} = \begin{bmatrix} p_{1,1} & p_{1,2} & . & . & . & p_{1,n_f} \\ p_{2,1} & p_{2,2} & . & . & . & p_{2,n_f} \\ . & . & . & & . & . \\ . & . & . & & . & . \\ p_{i,1} & p_{i,2} & . & p_{i,j} & . & p_{i,n_f} \\ . & . & . & & . & . \\ . & . & & . & . & . \\ p_{n_p-1,1} & p_{n_p-1,2} & . & . & . & p_{n_p-1,n_f} \\ p_{n_p,1} & p_{n_p,2} & . & . & . & p_{n_p,n_f} \end{bmatrix} \tag{8.5}$$

where, $p_{i,j}$ represents bit value at j^{th} feature position in i^{th} population individual. Here $j = 1$ to n_f and $i = 1$ to n_p. 1's and 0's in each population individual represent the selected and non-selected features respectively. $p_{i,j}$ for $\mathbf{p}_1$ to $\mathbf{p}_{n_{p-1}}$ are generated setting probability equal to 0.5 for a bit being 0 or 1 to inherently achieve at least 50% feature reduction. The last row population individual $\mathbf{p}_{n_p}$ is set to $\mathbf{p}_{all}$ and is defined as a population individual representing an 'All-feature' set in the optimization space. This tunes the DE optimization process to find a final subset of optimized and reduced features that achieves even better fitness than the all feature set and is mathematically represented in Equation−8.6.

$$\boldsymbol{p}_{n_p} = \boldsymbol{p}_{all} = \begin{bmatrix} 1 & 1 & 1 & . & . & . & 1 \end{bmatrix}_{1\ x\ n_f} \tag{8.6}$$

The number of individuals n_p is chosen as 50 so that it is large enough to avoid stagnancy and small enough to avoid excessive computing time [163, 164].

Fitness evaluation

The fitness function *fit* in this case is modelled as the k-category Matthew's correlation coefficient (MCC) [151, 165] mathematically expressed as Equation−8.7 considering one versus rest strategy taking all 8 classes one by one as positive (P) and the rest of 7 classes as negative class (N). All feature subsets represented by $\mathbf{p}$ in $\mathbf{P}$ are selected from the dataset and individually trained using PNN as explained in section 8.6.4

and *fit* is calculated on the testing subset.

$$MCC_k = \frac{TP \cdot TN + FP \cdot FN}{\sqrt{(TP+FP)(TP+FN)(TN+FP)(TN+FN)}} \tag{8.7}$$

Here, TP = number of samples for which positive class was correctly identified, TN = number of samples for which negative class was correctly identified, FP = number of samples for which positive class was wrongly identified and FN = number of samples for which negative class was wrongly identified and k denotes the number of classes and $k = 8$ for the current problem. Hence, FP and FN represent misclassifications or error made by the classification algorithm. Mean calculated over MCC individually for 8 classes is modelled as *fit*. A maximization of *fit* is carried out to find the optimum combination of features. Maximization of the defined fitness function is carried out using maximum 200 generations.

$$fit = mean(MCC_k) \tag{8.8}$$

Crossover

Randomly selecting two different individuals $\mathbf{p}_{i1}$ and $\mathbf{p}_{i2}$ from $\mathbf{P}$, a 1-point crossover is performed where, $i1, i2$ are randomly generated index values between 1 to n_f with crossover probability ($CR = 0.8$). The population individual $\mathbf{v}_i$ obtained after the crossover operation is called an offspring. Similarly, an offspring vector is created corresponding to every row in $\mathbf{P}$ to create a trial population matrix $\mathbf{V}$.

Mutation

A bit-flip is performed with mutation probability ($MR = 0.2$) for all $\mathbf{v}_i$'s in $\mathbf{V}$. Hence, currently there exists a parent population $\mathbf{P}^G$ and an offspring population $\mathbf{V}^{G+1}$ (after crossover and mutation) both of size n_p x n_f.

Selection

Fitness function *fit* for each individual in the $\mathbf{V}$ is calculated using Equation−8.8. Applying the current-to-best strategy, if $\mathbf{v}_i$ shows a higher *fit* value than the corresponding $\mathbf{p}_i$, then $\mathbf{p}_i$ in the $\mathbf{P}$ is replaced with $\mathbf{v}_i$. Otherwise, the $\mathbf{p}_i$ retains its position. This comparison and replacement process is repeated for every ($\mathbf{p}_i$, $\mathbf{v}_i$) pair an evolved version of $\mathbf{P}$ is obtained at the end of the generation. This process evolves and accumulates better individuals until the maximum number of generations i.e. 200 is reached. After looping through all generations every individual in the $\mathbf{P}$ is replaced with the best possible candidate i.e having highest *fit* value. $\mathbf{p}_{sel}$ with best *fit* in the end $\mathbf{P}$ is selected as the optimum feature subset with 1's representing the selected features out of total n_f.

Termination

The process terminates if the maximum number of given generations 200 is reached or *fit* becomes stagnant for a consecutive 20 generations. For every new generation, a new $\mathbf{V}$ is generated using the updated $\mathbf{P}$. Hence, crossover and mutation occur in every generation.

Table 8.1: DE control parameters summary

Parameter	Value
Population size	50
Population type	Binary bits
Crossover	1-point crossover
Mutation	Uniform
Selection scheme	Current-to-best
Population individual length	253
Maximum number of generations	200
Crossover probability	0.8
Mutation probability	0.2

8.6.4 Disease-based PNN classification

Training and testing subsets composed of optimized subset of features $\mathbf{p}_{sel}$ obtained in the last step are now extracted from complete training and testing subsets and can now be used to classify unseen beats using PNN [9]. The PNN consists of an input layer, a pattern layer, a summation layer, and a output layer. This architecture is illustrated in Figure−**??**(Step 4). The neurons of the input layer convey the input features $\mathbf{x} = [x_1, x_2, ..x_j, .., x_{n_s}]^T$ to the neurons of the pattern layer directly, where n_s represents the number of optimized features in $\mathbf{p}_{sel}$ and $n_s <= n_f$.

In the pattern layer, the output of the neuron $\mathbf{x}_{ko}$ is calculated by the Gaussian function given in Equation−8.9 with the input pattern vector $\mathbf{x}$ conveyed from the input layer:

$$g_{ki}(\boldsymbol{x}) = \frac{1}{\sqrt{(2\pi\sigma^2)^{n_f}}} \exp(-\frac{\|\boldsymbol{x} - \boldsymbol{x_{ki}}\|^2}{2\sigma^2}) \tag{8.9}$$

where x_{ki} is the neuron vector, σ is the spread (standard deviation) parameter for the Gaussian and n_s is the dimension of the pattern vector $\mathbf{x}$. $\|\boldsymbol{x} - \boldsymbol{x_{ki}}\|$ is the Euclidean distance (square root of the sum of squared differences) between x and x_{ki} .The summation layer neurons calculate the maximum likelihood of the pattern vector $\mathbf{x}$ being classified into class k by averaging the output of all pattern layer neurons that belong to the same class as in eq−8.10.

$$s_k(\boldsymbol{x}) = \frac{1}{(\sqrt{(2\pi\sigma^2)^{n_b}}} \frac{1}{n_k} \sum_{1}^{n_k} \exp(-\frac{\|\boldsymbol{x} - \boldsymbol{x_{ki}}\|^2}{2\sigma^2}) \tag{8.10}$$

where n_k is the total number of the samples in class k. The neuron in the decision layer determines the class belongingness of the pattern $\mathbf{x}$ by Equation−8.11 in accordance with Bayes's decision rule under the following assumption: the loss function associated with misclassification for each class is the same, and the a priori probability function of each class is the same.

$$c(\boldsymbol{x}) = max(p_k(\boldsymbol{x})) \tag{8.11}$$

Where k denotes the number of classes in the training samples and $c(x)$ is the estimated class of the pattern $\mathbf{x}$. In this paper, the output of the PNN is represented as the Lb of the eight types of ECG beats (i.e., NORM, LBBB, RBBB, PVC, APC, VESC, VFLT and PACE are labeled as '1', '2', '3', '4', '5', '6', '7', and '8', respectively).

8.7 Performance Evaluation

ECG data for this study belongs to "MIT−BIH arrhythmia database" developed in 1987 and available as open source on Physionet (https://physionet.org) [89, 60]. The database consists of 48 two-channel ambulatory ECG records, each of approximately 30 minutes duration digitized at a sampling rate of 360 Hz acquired from 47 subjects out of which 25 subjects were men aged 32 to 89 years, and 22 were women aged 23 to 89 years (2 records came from the same subject). Each record has simultaneous recordings from 2 leads, MLII and V5. For the purpose of testing a wearable ECG sensing scenario which mostly uses single-lead for acquisition [166], this work uses ECG signal from only the MLII lead. Each record is supported by an annotation file providing the R-peak positions and corresponding beat labels (Lb). Hence for this research, 107800 heartbeats are used having corresponding labels for 8 classes i.e. normal (NORM), left bundle branch block (LBBB), right bundle branch block (RBBB), premature ventricular contraction (PVC), atrial premature contraction (PAC), ventricular escape (VESC), ventricular flutter wave (VFLT) and paced (PACE) beat. The selected 8 classes include less frequent but clinically significant arrhythmic beats too to prove the validity of the proposed algorithm.

Out of the 108700 beat samples, 50% were selected as the training subset and remaining 50% as the testing subset. Table−8.2 summarizes the details of the constructed dataset regarding the number of samples in each class used to test the proposed algorithm.

Classification metrics; Matthew's correlation coefficient (MCC), accuracy (Acc), sensitivity (Sen), specificity (Spe) and F-score ($F1$) are reported according to Equations−(8.7), (8.12), (8.13), (8.14) and (8.15) with *fit* modelled as MCC and compared using *fit* as Acc, $F1$, AUC separately. All the definitions mentioned below follow a one-versus-rest strategy [167]. Each classification measure is calculated for each of the eight classes (taking one class as positive and all the rest as negative)

and then averaged to represent mean classification measure. The PNN classification was performed for *All features* set (as gold standard) and *Optimized features* subset obtained after DE. Hence, all measures are reported for both *All features* and *Optimized features* cases to present a comparison between classification improvement and feature reduction achieved using the proposed method. Here, TP, TN, FP and FN follow the same definition as mentioned in section 8.6.3.

$$Acc = \frac{TP + TN}{TP + TN + FP + FN} \tag{8.12}$$

$$Sen = \frac{TP}{TP + FN} \tag{8.13}$$

$$Spe = \frac{TN}{TN + FP} \tag{8.14}$$

$$F1 = \frac{2 \cdot TP}{2 \cdot TP + FP + FN} \tag{8.15}$$

Table 8.2: MIT-BIH data selection details

Beat class	Training	Testing	Total
NORM	36907	36907	73814
LBBB	4031	4031	8062
RBBB	4533	4533	9066
PVC	3363	3363	6726
PAC	1270	1271	2541
VESC	53	53	106
VFLT	236	236	472
PACE	3506	3507	7013
Total	53899	53901	107800

8.8 Results and discussion

Table−8.3 shows a comparison of the proposed DE-PNN algorithm with the selected 'All feature' standard. The confusion matrices for both are reported in Table−9.2. The optimized features which result in the maximum *MCC* is plotted in Figure−8.4. The average number of generations by which the optimization is achieved was 78±12 (10 trials). After an average 78 generations, the fitness value becomes stagnant meaning the fitness function has achieved its maximum value and is no longer improving.

Using the DE-PNN scheme, the best and worst were the accuracy of 99.84% for VESC and 95.41% for NORM, respectively. The DE-PNN scheme could classify NORM with an accuracy of 99.45%, PVC with 99.18%, PACE with 100.00%, RBBB

Table 8.3: Classification test result

Features	NumFeat	MCC	Acc	F1	AUC
All	253	0.1248	99.05	92.69	0.8242
Optimized	41	0.1250	99.33	92.52	0.8370
Difference	212	0.0002	0.28	0.17	0.0128

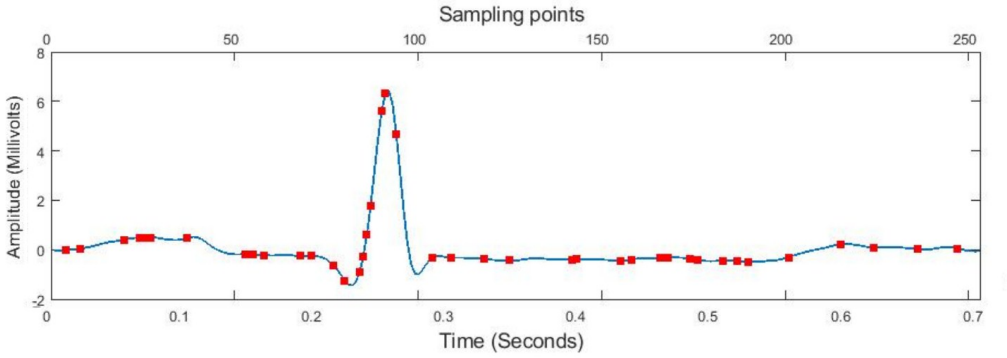

Figure 8.4: Selected features after DE.

with 99.94%, LBBB with 99.80%, APC with 99.76%, VFL with 99.61%, and VESC with 99.94%. These results demonstrate the abilities of the above-mentioned ECG arrhythmia classification schemes to classify the eight ECG beats effectively. The overall accuracy of the DE-PNN scheme, the DE-PNN scheme, and the DE-PNN scheme were 99.61%, 98.26%, and 99.71%, respectively as reported in Table−8.5.

To analyze the goodness of optimized features at distinguishing between simulated cardiac conditions, receiver operating characteristic (ROC) is plotted using again a one-versus-all class strategy and area under the curve (AUC) is calculated. By analogy, higher the AUC, the higher the capability of recognition of the particular class by the classification algorithm. Figure−8.5 shows the ROCs and AUCs of every class in case of optimized and all features. The AUC for all arrhythmia classes except paced beat has increased with maximum AUC improvement for ventricular flutter (10%) which is rarest class in the currently used dataset and secondarily premature ventricular contraction (4%), both representing critical pathological conditions. Overall the recognition for all classes has improved or stayed consistent with 83.79% reduction is number of features.

The proposed method presented an accurate and computationally efficient arrhythmia classification method using direct ECG amplitude signal features. More than 100,000 ECG heartbeats are obtained with eight types of ECG beats including normal beat and seven arrhythmic beats. Feature optimization was performed by modelling optimization input as binary vectors representing different feature combinations using

Table 8.4: Confusion matrices for testing subset with DE-optimized and All features with *fit* = MCC for 1 normal and 7 arrhythmia classes

T/P	NORM	LBBB	RBBB	PVC	PAC	VESC	VFLT	PACE
NORM	36476	9	312	34	68	0	3	5
LBBB	12	4007	1	9	1	1	0	0
RBBB	313	1	4208	6	4	1	0	0
PVC	108	16	4	3219	5	3	6	2
PAC	165	1	24	1	1079	0	1	0
VESC	1	1	0	0	0	51	0	0
VFLT	15	3	12	17	0	0	188	1
PACE	2	0	1	1	0	0	0	3503

T/P	NORM	LBBB	RBBB	PVC	PAC	VESC	VFLT	PACE
NORM	36503	6	302	19	72	3	1	1
LBBB	26	3999	1	1	2	2	0	0
RBBB	317	0	4206	5	4	1	0	0
PVC	270	16	7	3058	6	1	2	3
PAC	144	1	27	0	1099	0	0	0
VESC	0	0	0	0	1	52	0	0
VFLT	63	3	5	12	1	0	150	2
PACE	11	0	1	1	0	0	0	3494

DE. An optimized feature subset is obtained which was then used with a simple and PNN classifier. The proposed method achieved 83.79% reduction in directly acquired features with comparable classification performance. Figure−8.4 shows the optimized and selected 41 out of total 253 amplitude feature points. The higher classification performance achieved could be due to better beat definition (250 ms before and 450 ms after the R-peak positions as compared to [168, 139] which arbitrarily used 200 samples around the R-peak. Our definition makes sure the inclusion of important physiological characteristics necessary to distinguish between the currently classified arrhythmia types which are most ventricular type. Also on the algorithm design level, adding an all feature combination to the solution space pushes the optimization process to find a solution better than the *All features* scenario.

Also, we compared the classification performance of the proposed DE-PNN scheme for ECG arrhythmia classification with those of other schemes simultaneously utilizing different feature reduction methods and neural classifiers presented in the literature as summarized in Table−8.6. Jun et al. [168] used the same direct ECG amplitude features as done in this work and presented a comparison between 2D-CNN, AlexNet and VGGNet models. All three of the models were deployed using TensorFlow which is a deep learning Python library proposed by Google specially for GPGPUs and yet used 2 Intel Xeon E5 CPUs and 2 NVIDIA K20m GPUs to reduce the learning time. All tested classifiers had complex architectures implying extremely

Table 8.5: Classification results for testing subset with DE-optimized and All features with *fit* = MCC for 1 normal and 7 arrhythmia classes

Optimized features					
Class	Acc	Sen	Spe	F1	MCC
NORM	96.73	97.24	96.37	96.10	1
LBBB	99.65	99.06	99.73	98.60	-1
RBBB	98.50	96.13	98.84	94.12	0
PVC	98.93	94.13	99.62	95.66	0
PAC	98.12	84.00	99.40	88.14	0
VESC	99.90	96.22	99.93	94.44	0
VFLT	99.28	84.78	99.86	90.06	0
PACE	99.90	99.20	99.96	99.39	1
Average	99.90	99.20	99.96	99.39	1

All features					
NORM	94.46	97.52	92.30	93.58	1
LBBB	99.73	98.93	99.84	98.93	-1
RBBB	98.44	93.46	99.14	93.71	0
PVC	97.97	86.26	99.64	91.38	0
PAC	98.34	86.40	99.42	89.62	0
VESC	99.91	96.22	99.95	95.32	0
VFLT	98.62	64.78	99.96	78.21	0
PACE	99.80	98.00	99.96	98.79	1
Average	99.90	99.20	99.96	99.39	1

high computational cost with no feature optimization/reduction function which is not suitable for continuous monitoring using wearable sensing modality. Yildrim et al. [137], Tuncer et al. [138] and Elhaj et. al [129] used wavelet features with multiple different combination of features to perform arrhythmia classification adding feature computation layer in the processing algorithms performing optimizations focused on classifier parameters rather than feature engineering.

DE-PNN aimed at searching the optimum feature combination that provides maximum recognition capability for arrhythmic heartbeats removing redundant and selecting highly discriminating features. Overall the achieved ECG arrhythmia classification result indicates that detection of arrhythmia using 16.21% features of a complete ECG heartbeat can be an effective approach to help general physicians and cardiology specialists to diagnose critical cardiovascular diseases in a continuous and long-term, online or offline monitoring scenarios particularly well-suited for a wearable sensing setting. For the future work, the current algorithm may be extended to recognize 16 classes (1 normal and 15 arrhythmic) for which the annotations are available with MIT-BIH dataset. A future DE optimization might focus on

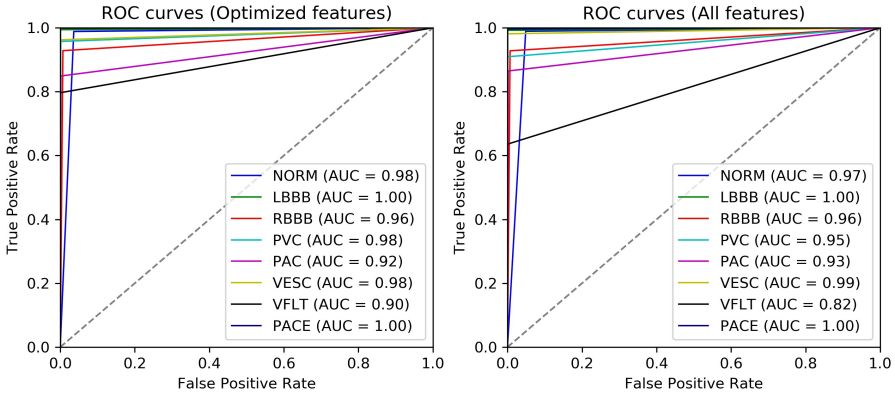

Figure 8.5: ROC curves of 8 classes for (a) Optimized feature subset and (b) All feature set.

Table 8.6: Comparison of the proposed DE-PNN scheme with latest literature

Research	Feature type	#Classes	Feature selection	Classification	Accuracy(%)
DE-PNN	Morphology	8	DE	PNN	99.33
[168]	Morphology	8	None	CNN	98.9
[168]	Morphology	8	None	AlexNet	98.8
[168]	Morphology	8	None	VGGNet	98.7
[137]	Morphology	5	CAE	LSTM	99.0
[145]	Wavelet	5	PSO	LS-SVM, RF	98.95
[129]	HOS+Wavelet	5	ICA+PCA	SVM+NN	98.91
[126]	PSD+DFT	17	GA	SVM, kNN, PNN, and RBFNN	98.85
[92]	DCT + weighted inter-beat	5, 15	none	SVM	98.46
[138]	Multilevel wavelet	17	NCA	1-NN	95.0
[131]	k-medoids vector quantization	4	none	parallel regression NN	95.00
[54]	Morphology	5	none	9-layer Deep CNN	94.03
[169]	Temporal vectorcardiogram	3	PSO	SVM	92.40

a multi-objective approach to maximize arrhythmia recognition whilst minimizing percentage signal distortion (accuracy and compression being the two objective functions) to make the ECG signal reproducible for clinical analysis. The proposed DE-PNN scheme can provide better classification accuracy considering one normal and seven types of arrhythmia with 83.79% reduced features which validates that the proposed scheme can be used as an effective tool for cardiologists to diagnose heart diseases using ambulatory ECG signals.

Chapter 9

Recurrence Analysis of Human Body Movements

9.1 Recurrence Quantification Analysis

Recurrence quantification analysis (RQA) [170, 171, 172] is a nonlinear data analysis (cf. chaos theory) technique used for the investigation of systems that continuously change state with reference to time also called dynamic systems. RQA quantifies the periodicity or non-periodicity and duration of recurrences in a dynamic system as reflected by its phase space trajectory signal. RQA was developed primarily to quantify distinct patterns or behaviors presenting in specific RQA figures called recurrence plots (RPs), based on the small-scale structures. RPs are used to visualise in detail the recurrence behaviour of the phase space trajectory of dynamic systems.

RPs typically contain single dots and combination of dots making line structures which are parallel to the mean diagonal called the line of identity (LOI). These line structures may show a vertical, horizontal or diagonal type structures. Because an RP is usually symmetric, horizontal and vertical lines correspond to each other, and, hence, only vertical lines are considered. These lines reflect a typical behavior of the phase space trajectory. The diagonal lines characterize such parts of the phase space trajectory which run parallel for some time, the vertical lines represent those segments which remain in the same phase space region for a certain time. The RQA quantifies the small-scale structures in RPs, which present the number and duration of the recurrences of a dynamical system. The measures introduced for the RQA were developed heuristically between 1992 and 2002 [173, 171, 174]. They are actually measures of complexity. The main advantage of the RQA is that it can provide useful information even for short and non-stationary data, where other methods fail. An RP are calculated as in Equation−(9.1):

$$\mathbf{R}_{i,j}^{m,\rho} = \Theta(\rho - \|\mathbf{x}(i) - \mathbf{x}(j)\|) \tag{9.1}$$

where, $\mathbf{x}(i), \mathbf{x}(j)\ \epsilon\ \mathbb{R}$, $i, j = 1, 2, 3, ..., N$, N is the number of states, m is the embedding dimension, $\Theta(.) : \mathbb{R} \rightarrow (0, 1)$ is the Heaviside step function, $\|(.)\|$ is the norm and ρ is a distance threshold usually calculated as $0.2 \cdot$ mean$(\|\mathbf{x}(i) - \mathbf{x}(j)\|$. The multiple RQA parameters used to characterize the state of a system from RPs

are:

1) Recurrence rate The percent recurrence (%RR) signifies how often a trajectory visits similar locations in state space computed as the percentage of recurrent points in the recurrence matrix as in Equation−(9.2):

$$\%RR = \frac{1}{N(N-1)} \sum_{i \neq j=1}^{N} \mathbf{R}_{i,j}^{m,\rho} \tag{9.2}$$

2) Determinism The percent determinism (%DET) is quantified as the fraction of recurrent points that form diagonal lines (at least three consecutive points in length) parallel to the main diagonal computed as in Equation−(9.3):

$$\%DET = \frac{\sum_{l=d_{min}}^{N} l H_D(l)}{\sum_{i,j=1}^{N} \mathbf{R}_{i,j}^{m,\rho}} \tag{9.3}$$

3) Entropy Shannon entropy (ENT) of the frequency distribution of the diagonal line lengths and measures the complexity of the system. The entropy of the probability distribution of the diagonal lines lengths $p(l)$ of $\mathbf{R}_{i,j}^{m,\rho}$ is calculated as in Equation−(9.4):

$$ENT = -\sum_{l=d_{min}}^{N} p\left(l\right) l\left(p\left(l\right)\right), \quad where\ p\left(l\right) = \frac{H_D(l)}{\sum_{l=d_{min}}^{N} H_D(l)} \tag{9.4}$$

4) Average diagonal line length It is the average time (L) two segments of the trajectory are close to each other In this case, L can be interpreted as the mean prediction time and is calculated as in Equation−(9.5):

$$L = \frac{\sum_{l=d_{min}}^{N} l H_D(l)}{\sum_{l=d_{min}}^{N} H_D(l)} \tag{9.5}$$

where, $i, j = 1, 2, 3, ..., N$, N is the number of states and $H_D(l)$ is the histogram of frequency of occurrence of different diagonal line lengths l in $\mathbf{R}_{i,j}^{m,\rho}$ and d_{min} is the minimum number of consecutive points considered a diagonal ($d_{min} = 3$).

One of the biggest challenges in the design and development of smart wearable devices targeted for 24 hour usage is catering for human body movements during daily life activities (ADL) since body movement noise hugely affects the signal recorded using wearable sensors. However, there are other factors that also play part in increasing everyday usability of wearable devices such as low power consumption, on-chip processing, skin-friendly fabrication material and user acceptance. Human body movement analysis is performed for multiple applications for example activity monitoring [175], fall detection for the elderly, technique analysis in athletes [176], dance composition [177], gait recognition, internet-of-things based healthcare sensors [178] and design and development of bio-mechanical products [179] etc.

Recurrence is a fundamental property of dynamical systems, which can be exploited to characterize the system's behaviour in time-varying states. Recurrence analysis

has been used successfully as a tool for describing complex dynamic systems that are inadequately characterized by standard methods for time-series data analysis [180, 181]. Recurrence plots (RPs) and cross recurrence plots (CRPs) produce readily interpretive visualizations of two input signals that provide insight into the characteristics of changing system states and also provide tools to assess repeated patterns, sequences, and regime shifts both quantitatively and qualitatively [182]. Recurrence quantification analysis (RQA) [183, 184] has recently gained importance regarding constantly changing complex signals for the identification, quantification and assessment of synchronization patterns. This method can be used to represent signals into time-changing regular and irregular system states. Recurrence plots have been shown to be a valuable data visualization tool for the analysis of dynamic systems in a variety of scientific application areas for e.g. neuroscience [180], engineering [185], cardiology [186], geosciences [187], behavioural sciences [188] specifically gait analysis [189] and other research disciplines.

Specific to this work, as mentioned above, ECG signals acquired by wearable devices are hugely corrupted by body movement noise which reduces their usage as the recorded input signal might not exactly or correctly reflect physiological factors. Hence, in an attempt to understand body movement signals and characterize them a couple of research studies were performed with ECG and acceleration signals since modern wearable devices now simultaneously record both ECG and acceleration signal which might help characterize the nature of body movements and possibly remove them too. But it remains a goal for the future. For the purposes of this work the following sections include 3 studies conducted that models RQA as a tool to characterize body movements using signals acquired by wearable sensors to enhance the functionality and usability of these sensing devices to put them to practical use [190, 191, 192].

9.2 Movement modelling in wearable ECG sensors

RQA has been previously used to inspect changing synchronization states using HRV and ECG signals to analyze various cardiac arrhythmias such as atrial fibrillation [55], ventricular fibrillation and superaventricular fibrillation phase patterns to reveal the onset and recurrence of arrhythmic states [193]. Moreover, recurrence metrics have proven to provide distinguishing classification features for various above mentioned arrhythmia classes. However, this technique has never been applied to exercise ECG data to study quantitatively distinctive recurrence features. This might lead to better understanding of effect of different types of body movements on the motion artifact corrupting ECG signal and help in evaluating specific design parameters for noise filtering in wearable ECG sensing devices. The database selected [194, 60] for this study offers simultaneously recorded ECG signals during performance of different exercise activities placing the wearable device at multiple angles. Utilizing this feature, in the current research we perform recurrence analysis using synchronicity

of ECG signals simultaneously recorded using multiple pairs electrodes embedded in a wearable device. Different values of recurrence measures recorded for three exercise activities standing, walking and jumping and 3 offset angles 0°, 45°and 90°are calculated using recurrence plots. The results are reported as distinguishing features for different exercise activities and offset angles.

Table 9.1: Recurrence metrics for exercise activities standing, walking and jumping and offset angles 0°, 45° and 90°

Activity	Angle	Recurrence Rate (RR)						Entropy (ENT)						Average Diagonal Length (L)					
		r_{12}	r_{13}	r_{14}	r_{23}	r_{24}	r_{34}	r_{12}	r_{13}	r_{14}	r_{23}	r_{24}	r_{34}	r_{12}	r_{13}	r_{14}	r_{23}	r_{24}	r_{34}
Standing (test_01 - test_09)	**0**	0.77 (0.09)	0.72 (0.11)	0.71 (0.16)	0.65 (0.09)	0.64 (0.14)	0.61 (0.15)	4.96 (0.06)	4.79 (0.16)	5.14 (0.54)	4.58 (0.17)	4.81 (0.49)	4.78 (0.38)	121.36 (33.04)	101.97 (31.69)	116.87 (52.16)	69.05 (13.46)	73.55 (22.62)	65.82 (19.87)
	45	0.68 (0.09)	0.74 (0.12)	0.82 (0.03)	0.69 (0.14)	0.76 (0.07)	0.82 (0.11)	4.58 (0.29)	5.05 (0.50)	5.07 (0.21)	4.9232 (0.44)	4.79 (0.25)	5.45 (0.62)	75.3045 (13.13)	93.74 (27.77)	125.35 (31.33)	82.93 (26.74)	108.29 (19.32)	141.46 (53.58)
	90	0.69 (0.17)	0.78 (0.11)	0.71 (0.12)	0.82 (0.15)	0.74 (0.15)	0.83 (0.08)	4.96 (0.57)	4.79 (0.25)	4.79 (0.51)	5.39 (0.63)	5.12 (0.68)	4.96 (0.16)	89.72 (31.44)	124.39 (44.44)	83.85 (30.30)	178.22 (32.94)	103.99 (48.49)	154.21 (71.87)
Walking (test_10 - test_18)	**0**	0.76 (0.08)	0.76 (0.13)	0.71 (0.18)	0.74 (0.15)	0.68 (0.13)	0.68 (0.18)	5.43 (0.50)	5.24 (0.53)	5.37 (0.70)	5.15 (0.70)	5.15 (0.63)	5.08 (0.66)	120.20 (41.56)	123.88 (50.17)	124.85 (46.81)	99.62 (46.00)	86.63 (40.97)	88.44 (46.03)
	45	0.75 (0.16)	0.78 (0.19)	0.77 (0.11)	0.73 (0.19)	0.72 (0.10)	0.80 (0.17)	5.13 (0.82)	5.39 (0.88)	5.25 (0.43)	5.28 (0.86)	5.13 (0.47)	5.69 (0.91)	104.36 (36.19)	145.62 (47.05)	132.93 (59.53)	117.15 (69.47)	106.51 (32.38)	181.97 (46.03)
	90	0.73 (0.18)	0.75 (0.13)	0.72 (0.17)	0.77 (0.12)	0.75 (0.17)	0.80 (0.12)	5.45 (0.94)	5.34 (0.75)	5.26 (1.06)	5.70 (0.76)	5.56 (1.07)	5.56 (0.78)	142.60 (42.88)	132.65 (33.72)	140.97 (26.76)	152.89 (53.86)	168.72 (64.57)	154.31 (61.70)
Jumping (test_19 - test_27)	**0**	0.48 (0.18)	0.46 (0.14)	0.43 (0.17)	0.63 (0.08)	0.59 (0.21)	0.56 (0.15)	4.97 (0.17)	4.84 (0.18)	5.03 (0.37)	4.82 (0.48)	4.97 (0.54)	4.85 (0.47)	86.54 (10.18)	84.76 (14.26)	91.36 (34.09)	72.21 (17.94)	79.91 (41.46)	70.63 (25.19)
	45	0.47 (0.13)	0.49 (0.15)	0.58 (0.20)	0.49 (0.05)	0.58 (0.05)	0.60 (0.09)	4.80 (0.42)	4.98 (0.44)	5.01 (0.14)	4.90 (0.47)	4.95 (0.27)	5.19 (0.43)	67.56 (13.72)	78.89 (27.11)	97.30 (22.87)	69.30 (23.40)	87.20 (20.04)	118.21 (45.68)
	90	0.69 (0.18)	0.74 (0.12)	0.71 (0.13)	0.78 (0.18)	0.74 (0.18)	0.80 (0.09)	5.21 (0.71)	5.22 (0.46)	5.16 (0.62)	5.72 (0.80)	5.30 (0.70)	5.32 (0.37)	102.44 (28.63)	130.9 (51.92)	95.54 (35.83)	178.18 (61.18)	118.21 (58.53)	155.77 (67.033)

9.2.1 Electrode synchronicity RQA model for ECG signal

Preprocessing steps include ECG frequency filtering using a bidirectional 6^{th}-order Butterworth band-pass filter with high-pass and low-pass cut-off points 0.5Hz and 40Hz, respectively. Baseline error was calculated using cubic-spline interpolation of fiducial points, placed 90 milliseconds before each R-peak (computed using a standard peak detection algorithm) and subtracted from the input signal.

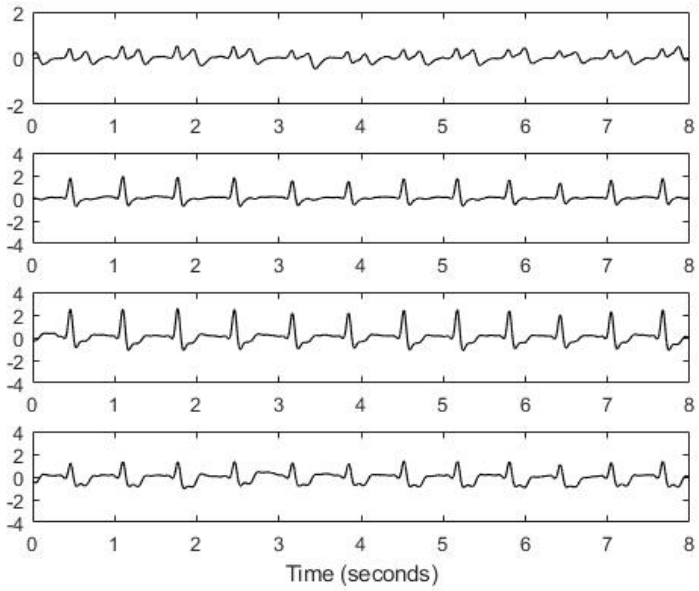

Figure 9.1: Input ECG signal through 4 pairs of electrodes

For a mathematical formulation of the recurrence analysis of motion artifacts, we consider ECG time series $e_i(n)$, with $0 \leq n \leq N$ and $1 \leq i \leq 4$. Where, i represents the number of electrode used for simultaneous recording from 4 electrode pairs and N as is the number of samples in each signal. Figure−9.5 shows the signal recorded from 4 different electrode pairs embedded in the used wearable device.

Our aim here is to test the level of synchronization between all electrode signals with each other. Hence, to test the two-electrode synchronization, all electrode combinations are considered i.e. (1, 2), (1, 3), (1, 4), (2, 3), (2, 4) and (3, 4). A cross-recurrence plot for each electrode pair combination is calculated. Hence, for a single ECG input record from the used database we get six cross-recurrence matrices $r_{12}(t)$, $r_{13}(t)$, $r_{14}(t)$, $r_{23}(t)$, $r_{24}(t)$ and $r_{34}(t)$, each calculated by Equation−(9.6):

$$r_{ij} = \begin{cases} 1 & d(e_i, e_j) \leq \rho \\ 0 & else \end{cases} \tag{9.6}$$

where, r_{ij} is the recurrence matrix for electrode combination (i,j), d is the distance metric, in the current case correlation d(e_i, e_j) = cross correlation (e_i, e_j) and ρ is the selected threshold used as a measure of closeness of points in the recurrence plot.

ECG recordings from two electrodes are said to be synchronized or recurrent if their respective time series points are within ρ distance of each. Since the distance metric is symmetric i.e., d(e_i, e_j) = d(e_j, e_i), the resulting cross-recurrence plots are also symmetric. A recurrence plot is generated for each electrode pair combination. In this case, time is represented directly on the recurrence plot.

9.2.2 Performance analysis

Data consisted of 27 ECG records of 8 second duration with sampling rate 500 Hz, analogue gain 100 and resolution of 16-bits from a healthy 25-year-old male are recorded performing different physical activities standing, walking and jumping to induce different types of motion artifacts. 4 pairs of electrodes are built into a single patch and arranged at 0, 45 and 90 degree offsets as shown in Figure−9.2 (a, b, c and d). The data is used from open source database *Motion Artifact Contaminated ECG Database* [194] provided by Physionet [60].

We present our analysis and results in terms of recurrence quantification measures:

1) Recurrence rate The percent recurrence (%RR) signifies how often a trajectory visits similar locations in state space computed as the percentage of recurrent points in the recurrence matrix as in Equation−(9.7):

$$\%RR = \frac{1}{N(N-1)} \sum_{i \neq j=1}^{N} \mathbf{R}_{i,j}^{m,\rho} \tag{9.7}$$

3) Entropy Shannon entropy (ENT) of the frequency distribution of the diagonal line lengths and measures the complexity of the system. The entropy of the probability distribution of the diagonal lines lengths $p(l)$ of $\mathbf{R}_{i,j}^{m,\rho}$ is calculated as in

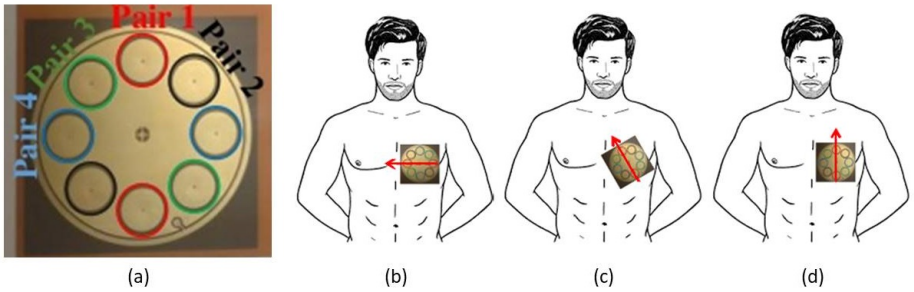

Figure 9.2: (a) ECG device with electrode pair embedding, device placement on body with (b) 90 degree, (c) 45 degree and (d) 0 degree offset

Equation−(9.8):

$$ENT = -\sum_{l=d_{min}}^{N} p(l)\, l(p(l)), \quad where\ p(l) = \frac{H_D(l)}{\sum_{l=d_{min}}^{N} H_D(l)} \tag{9.8}$$

4) Average diagonal line length It is the average time (L) two segments of the trajectory are close to each other In this case, L can be interpreted as the mean prediction time and is calculated as in Equation−(9.9):

$$L = \frac{\sum_{l=d_{min}}^{N} l H_D(l)}{\sum_{l=d_{min}}^{N} H_D(l)} \tag{9.9}$$

where, $i, j = 1, 2, 3, ..., N$, N is the number of states and $H_D(l)$ is the histogram of frequency of occurrence of different diagonal line lengths l in $\mathbf{R}_{i,j}^{m,\rho}$ and d_{min} is the minimum number of consecutive points considered a diagonal ($d_{min} = 3$). The value of threshold ρ is selected as 0.4 as the values for RR, ENT and L result in highest distinguishing values for standing, walking and jumping activities. Significance stratified with respect to exercise activities, standing, walking and jumping have been evaluated by using a paired Student's t-test. Values are reported as *mean* (*standard deviation*) taken over 3 activities and 3 offset angles each with 3 signal acquisition runs resulting in 27 input records, unless otherwise specified. The two-sided significance level p was set at 0.05 for every reported figure.

9.2.3 Results and discussion

Recurrence quantification measures, recurrence rate, entropy and average diagonal length are calculated for exercise activities standing, walking and jumping with offset angles 0°, 45° and 90° for all recurrence matrices r_{12}, r_{13}, r_{14}, r_{23}, r_{24} and r_{34} representing all electrode combinations using each record in the database and reported in Table−9.2.

The knowledge of transitions between regular and chaotic behaviors is essential to understand the underlying mechanisms behind complex systems.The highest

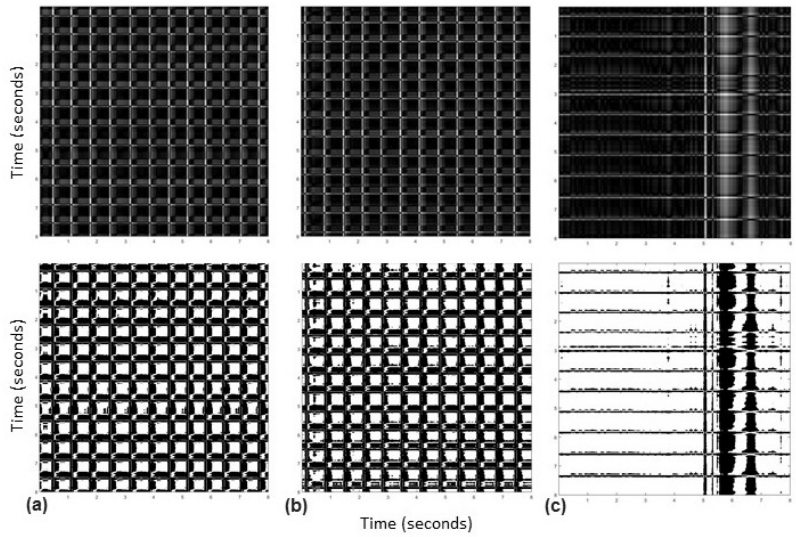

Figure 9.3: Recurrence plots (a) Standing, (b) Walking and (c) Jumping activities for electrode combination 3 and 4. Top figures represent no thresholding while bottom figures represent thresholded ($\rho = 0.4$) plots.

recurrence is observed for the standing position and least for the jumping activity showing that the probability of recurrence is high, and signal is least disrupted and most stable in the standing and highly disrupted, less stable with least probability of recurrence in the jumping case.

High value of entropy shows high electrode synchronization and low value of entropy shows less electrode synchronization. Entropy shows an increasing trend from standing to walking and jumping in all the electrode combinations processed. Average diagonal length decreases from standing to walking activity and increase from walking to jumping activity. The reduction in 'L'in the later segments also clearly indicate greater variability, so recurrences tend not to remain for long sequences. The highest values for disruption due to motion are observed for r_{34} in 20 out of 27 values recorded. Hence the electrode combination for 3 and 4 shows comparatively high distinguishing values for chaotic signal behavior repetitively.

Figure−9.3 shows recurrence plots for electrode combination 3 and 4 in case of standing, walking and jumping with ($\rho = 0.4$) and without thresholding. The plot clearly indicates most periodic and synchronized signal behaviour in case of standing, somewhat disturbances in the case of walking and a complete non-synchronicity in electrode outputs 3 and 4 is observed at the instance of the subject performing a jump. By comparing the RP measures between the standing, walking and jumping activity signals, we found a consistent decrease in RR, a consistent increase in ENT and an increasing to decreasing behavior from standing to walking and walking to jumping activities for L. In future, we intend to perform RQA analysis dividing the signal into different time intervals which might help us understand the different times in which a system stays in a disrupted state (due to motion) and when it recurs

back to a stable state. In this study, we used recurrence quantification measures to depict electrode synchronization for the assessment of motion artifacts. For every activity and all electrode placement angles, the distinguishing values of the parameters recurrence rate, line distribution Shannon entropy and diagonal line length show that RQA is a viable method for quantitative modelling and analysis of noise induced by motion artifacts into the recordings acquired through wearable ECG devices.

9.3 Body movement characterization

Based on the observation that wearable biomedical or specifically ECG devices also record acceleration signals in all 3 axis, these simultaneously recorded signals can very well be used to characterize the human body movement. This second study is novel in terms of presenting a quantification analysis for everyday activities, hence is applicable to daily activity monitoring scenarios. Some related work reports load-related movement complexity where Apley scratch, sit-and-reach and weight-bearing-lunge test were performed by subjects to quantify motion in the shoulders and thoracic spine, hip and trunk and dorsiflexion respectively [195]. Another research tests movement and cognition in a sit to stand task where adults executed a sit-to-stand task while counting backwards aloud as a secondary cognitive task [196]. Also, researchers analyzed posture maintenance of human test subjects on stable and stable sloped surfaces [197].

9.3.1 Time-series RQA modelling for acceleration signal

RQA analysis has been performed using the squared vector magnitude for acceleration calculated using x, y and z-axis data. Each time-series record was divided into three equal sections to analyze the rest and activity states separately. Computing recurrence plots and quantification metrics: recurrence rate, determinism and entropy for the available activities: lying and standing, picking up something and standing, sitting and standing, stepping up and down and walking, we show the difference between movement and resting states.

For a mathematical formulation of the recurrence analysis of body movements, we consider squared vector magnitude for acceleration $g_i(t)$, which for recording in number of samples can be written as $g_i(n)$ with $0 \leq n \leq N$ and $1 \leq i \leq 3$. Where, 'i 'represents the number of equal sections $g(t)$ is divided in to analyze the occurrence of activity with respect to time and 'N 'is the total number of samples in each signal.

Figure−9.4 shows the signal recorded for 5 different activities. The figure shows the division of signal into 3 sections: Section-I, Section-II and Section-III. Also the figure labels activities occurring on the time series by visual inspection. Our aim here is to make the recurrence plots and calculate recurrence parameters for Section-I, II and III. Hence, for a single 'g' input record from the used database we get three

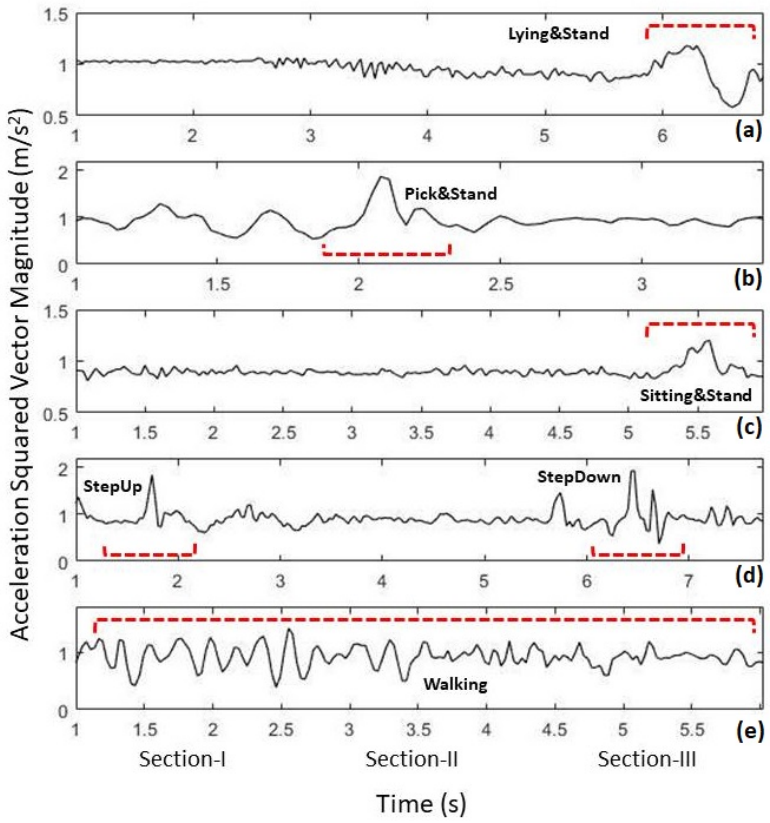

Figure 9.4: Input SVM signal for daily life activities a) lying and then standing, b) picking up and then standing, c) sitting and then standing, d) stepping up and then down, and e) walking acquired through MARG wearable sensor

Table 9.2: Recurrence metrics for ADL activities and time-divided sections

ADL	Recurrence Rate (RR)			Determinism (DET)			Entropy (ENT)		
	Section-I	Section-II	Section-III	Section-I	Section-II	Section-III	Section-I	Section-II	Section-III
Lying&Stand	0.869^{1} (0.145)	0.5 (0.196)	0.358^{2} (0.115)	0.96^{1} (0.064)	0.777 (0.097)	0.799^{2} (0.093)	2.674^{1} (0.816)	1.226^{1} (0.659)	1.398^{2} (0.370)
Pick&Stand	0.219^{1} (0.113)	0.242^{2} (0.093)	0.319 (0.159)	0.491 (0.165)	0.624^{12} (0.193)	0.6^{1} (0.182)	0.635^{1} (0.258)	0.874^{2} (0.358)	0.852 (0.396)
Sitting&Stand	0.38 (0.073)	0.808^{1} (0.082)	0.373^{2} (0.091)	0.688 (0.106)	0.948^{1} (0.039)	0.756^{12} (0.105)	0.965 (0.228)	2.062 (0.377)	1.12^{2} (0.292)
StepUp&Down	0.166^{12} (0.044)	0.307 (0.114)	0.201^{12} (0.105)	0.456^{2} (0.091)	0.616^{1} (0.145)	0.476^{2} (0.135)	0.591^{2} (0.138)	0.863^{1} (0.282)	0.634^{2} (0.232)
Walk	0.127^{12} (0.041)	0.118^{12} (0.039)	0.137^{12} (0.055)	0.339^{2} (0.091)	0.298^{2} (0.094)	0.335^{2} (0.117)	0.43^{12} (0.136)	0.383^{2} (0.110)	0.427^{12} (0.149)

$*$ p<0.05
† activity sections

recurrence matrices $r_1(t)$, $r_2(t)$ and $r_3(t)$, each calculated by Equation−(9.12):

$$r_i = \begin{cases} 1 & d(g_i, g_i) \leq \rho \\ 0 & else \end{cases} \tag{9.10}$$

where, 'd' is the distance metric, in the current case correlation d(g_i, g_i) =

correlation (g_i, g_i) and 'ρ' is the selected threshold used as a measure of closeness of points in the recurrence plot.

9.3.2 Performance analysis

The data [198] is acquired using the MARG (Magnetic Angular Rate and Gravity)[190], a multi-sensory wearable device tied to the subject's waist. 8 participants including 6 males and 2 females with average age 25.37 ± 2.56 years, height 1.79 ± 0.05 meters and weight 76.62 ± 10.59 kilograms perform different ADL: lying on a bed then standing, walking a few meters, sitting on a chair then standing, go up and down three steps and picking something up and then standing. Duration of records is variable among different subjects, trials and activities. The recorded data consists of 14 parameters for each recording of which we made use of 5 parameters: time in seconds, acceleration along x, y and z-axis and squared vector magnitude measured in terms of gravitational acceleration 'g' in meter per second square ($1g = 9.80665\ m/s^2$). Each record has three simultaneous acquisitions. The results were presented terms of RQA measures; RR, DET and ENT as in Equations−(9.7), (9.11) and (9.8), respectively.

Determinism (%DET) is quantified as the fraction of recurrent points that form diagonal lines (at least three consecutive points in length) parallel to the main diagonal computed as in Equation−(9.11):

$$\%DET = \frac{\sum_{l=d_{min}}^{N} l H_D(l)}{\sum_{i,j=1}^{N} \mathbf{R}_{i,j}^{m,\rho}} \tag{9.11}$$

where, $i, j = 1, 2, 3, ..., N$, N is the number of states and $H_D(l)$ is the histogram of frequency of occurrence of different diagonal line lengths l in $\mathbf{R}_{i,j}^{m,\rho}$ and d_{min} is the minimum number of consecutive points considered a diagonal ($d_{min} = 3$). The value of threshold 'ρ' is different for multiple activities ranging between 0.1 and 0.4. Results are presented for 5 activities and 3 time stages as mean (standard deviation) over 24 records (8 subjects and 3 simulation runs). The significance of the results is tested using Lilliefor's test setting $p < 0.05$. Total records processed are 120 (5 activities, 24 records for each activity).

9.3.3 Results and discussion

RQA measures, are calculated for the three sections of the recordings for all 5 ADL activities using the 3 recurrence matrices r_1, r_2 and r_3 defining the 3 separate sections. Values for each section are reported in Table−9.2. By visual inspection of inputs in Figure−9.4 and corresponding video files available with the dataset [198], section-I and section-II are non-activity and section-III is the activity phase for lying and then standing motion. Section-I and III are non-activity and section-II is the activity phase for picking and then standing motion. Section-I and II are non-activity and section-III is the activity phase for sitting and then standing motion. Section-II is the non-activity and section-I and III are the activity phase for stepping

up and down motion. There is no visible difference between sections with respect to activity/non-activity in the walking action.

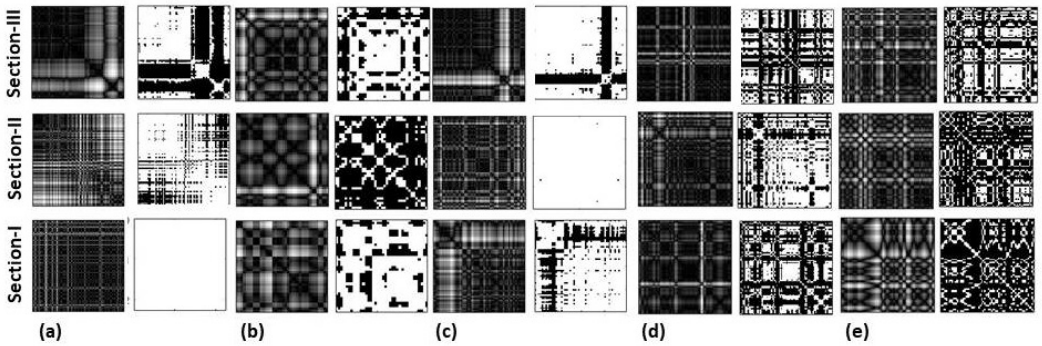

Figure 9.5: Recurrence plots for a) Lying&Stand, b) Pick&Stand, c) Sitting&Stand, d) StepUp&Down and e) Walk (left panel :non-thresholded, right panel:thresholded in all cases)

Understanding the changes between regular and irregular signal time periods in this case leads to identifying the rest and activity states of human body movements. As mentioned in the last paragraph, the observed mean values over the visually identified activity and non-activity sections respectively from Table−9.2 for recurrence rate are 0.249 and 0.466, for determinism 0.510 and 0.726 and entropy are 0.732 and 1.205. The highest recurrence is seen for the lying down phase and least for the walking activity showing that the signal is least disrupted while lying down and highly disrupted for walking activity. Determinism more or less follows the trend of recurrence. In other words, high value of determinism shows a less disrupted or rest phase in this case and low value shows a more disrupted or an activity state. High values of determinism are observed during the non-activity states and low vales are reported during the activity performance states. High value of entropy is reported in the case of non-activity and low value is observed in case of activity states showing less signal information contained in the non-activity state and high information contained in the activity state.

Figure−9.5 shows recurrence plots for all three time-divided sections I, II and III and, all five activities: a) lying and then standing, b) picking up something and standing, c) sitting and standing, d) stepping up and down and e) walking. These output recurrence plots correspond to the inputs shown in Figure−9.4. The left column represents non-thresholded while the right column represents thresholded plots for all corresponding activities. Figure−9.5 (panel a) identifies section-I as lying state, II as subject starting to move and III as the section in which the subject's position transitions from lying to standing position. Figure−9.5(panel b) identifies section-I as subject starting to pick up state, II as subject' main going down and moving back up activity and III as subject post-picking up section in which the subject's position transitions from moving up to standing position. Figure−9.5(panel

c) identifies section-I as sitting state, II as subject starting to move and III as the section in which the subject's position transitions from sitting to standing position. We notice similarities in section-III for both Figure−9.5(panel a) and Figure−9.5(panel c) (representing standing state in both cases) but differences in section-I between Fig.9.5(panel a) and Figure−9.5(panel c) (representing lying and sitting in the two referenced cases). Fig. 9.5(panel d) identifies section-I as stepping up, II as subject resting for a moment and III as the section in which the subject steps down again. Figure−9.5(panel e) identifies section-I, II and III as walking. We observe no clear difference between the three stages as the subject is continuously walking with a consistent body movement variation. For all time-divided sections and every activity, the discriminating numerical values of RQA parameters recurrence rate, determinism and entropy show that RQA is a useful assessment method for quantitative modelling and analysis of human body movements for data acquired through novel multi-sensory wearable sensors. In this study, we used recurrence quantification analysis to depict human body movements during daily life activities for the assessment of activity using wearable sensing device.

9.4 Fall detection

With the increase in human lifetime years over the last decades, the percentage of elderly people in the world keeps growing. The desire to stay at home and live independently can result in dangerous situations including undetected and harmful falls [199]. Falls in older adults often occur during walking and trunk position. Therefore, analysis of trunk movements during gait could present a viable approach to the development of such methods [200]. There are different ways to detect falls such as through vision or a wearable sensor [201]. Detection of fall is important and nowadays various practical solutions are presented for assisting the elderly against falls via detecting falls and triggering notification alarms calling for help as soon as falls occur in order to diminish fall consequences [202]. Novel algorithms and sensing devices can provide solutions to detect falls and generate alerts for first aid and rescue. The biggest challenge in the development of these algorithms and sensors is the flexibility to distinguish multiple kinds of falls during daily life scenarios. The common daily life activities include standing, walking on levelled ground, upstairs or downstairs, sitting down or getting up from a chair, running, jumping, lying down or getting up from the bed, and picking up object from floor, carrying load etc. [203] which could possibly lead to a fall event.

9.4.1 Time series RQA model for acceleration signal

RQA was performed and CRPs are plotted using both the squared vector magnitude for acceleration calculated using x, y and z-axis data and the orientation pitch angle

around the y-axis. Each time-series recorded was thresholded according to the value of 'g'to identify and analyse the pre-fall, fall and post-fall states separately. CRPs and quantification metrics; RR, DET and ENT were computed for two simulated falls: forward and backward. The distinguishing capabilities of the calculated novel RQA metrics are then tested using a basic support vctor machine (SVM) for the binary classification of pre-fall and fall states.

Squared vector magnitude of gravitational acceleration denoted by ga and the orientation pitch angle around the y-axis denoted by p are used as input signals for the computation of cross recurrence plots. For both signals the recording in number of samples is written as $ga_i(n)$ and $p_i(n)$ with $0 \leq n \leq N$ and $1 \leq i \leq 3$ where N is the total number of samples in each signal and i represents the number of equal-lengthed sections i.e. prefall, fall and postfall with respect to threshold on $ga \geq 1g$ for fall and $ga \leq 1g$ for pre-fall and post-fall (where g = 9.8 m/s^2).

Table 9.3: Recurrence metrics for fall simulations and thresholded sections

Falltype	*Recurrence Rate (RR)*			*Determinism (DET)*			*Entropy (ENT)*		
	Pre-fall	Fall	Post-Fall	Pre-fall	Fall	Post-Fall	Pre-fall	Fall	Post-Fall
Forward									
Kneelying	0.937	0.335	0.071	1.000	1.000	0.166	6.056	3.920	0.561
LateralPosition	0.965	0.716	0.571	1.000	1.000	0.788	5.262	4.462	3.604
Lying	0.403	0.105	0.005	0.542	0.375	0.042	2.785	1.446	0.079
LyingRecovery	0.417	0.070	0.090	0.500	0.250	0.125	2.846	0.973	0.711
Backward									
LateralPosition	0.774	0.623	0.504	0.872	0.958	0.657	4.152	3.995	2.977
Lying	0.798	0.287	0.111	0.958	0.957	0.166	4.518	3.024	0.717
LyingRecovery	0.835	0.246	0.098	0.986	0.914	0.207	4.932	3.208	0.901
Sitting	0.818	0.725	0.542	0.958	0.958	0.625	4.301	4.018	2.750

Figure−9.6 shows the 2 signals used as input for 8 different subcategories of backward and forward falls plotted against time. The 3 sections in which the signals are divided into are displayed: the solid line represents fall and the dotted line before and after it represent pre-fall and post-fall respectively. CRPs are then calculated for all three sections separately, so pre-fall, fall and post-fall, resulting into 3 cross recurrence matrices $r_i(n)$ using Equation−9.12:

$$r_i = \begin{cases} 1 & d(ga_i, p_i) \leq \rho \\ 0 & else \end{cases} \tag{9.12}$$

where 'd' is the distance metric, in the current case euclidean distance $d(ga_i, p_i) = euclidean(ga_i, p_i)$ and 'ρ' is the threshold used as a measure of closeness of points in the CRP and the recurrence metrics are calculated on the thresholded CRPs. In the last step, a simple SVM classifier is implemented to assess the detection accuracy for pre-fall and fall events using recurrence parameters as novel features. The test-train data split applied here is 50-50. The data was labeled with a 0 for pre-fall and a 1 for fall. After shuffling the data the classification was performed on the test data and the results are represented in terms of accuracy and positive detection rate.

9.4.2 RQA feature extraction

The results were presented terms of RQA measures for pre-fall, fall and post-fall phases. The parameters RR, DET and ENT are calculated as in Equations−(9.7), (9.11) and (9.8), respectively.

9.4.3 Performance analysis

SVM binary classification results are reported in terms of accuracy (Acc) and positive predictivity (+P) as given in Equation−(9.13) and (9.14) respectively:

$$Acc = \frac{TP + TN}{TP + TN + FP + FN} \tag{9.13}$$

$$+P = \frac{TP}{TP + FP} \tag{9.14}$$

where, TP = truely identified positives (pre-fall instances), TN = truely identified negatives (fall instances), FP = falsely identified positives and FN = falsely identified negatives. Threshold ρ for Equation−(9.7), (9.11) and (9.8) is set at 25.2, selected after hit and trial to maximize the detection accuracy in Equation−(9.13) of SVM classification algorithm in the second step of methodology. The test data [198] were collected from an experiment performed by 8 healthy participants (6 males and 2 females) with an average age 25.37 ± 2.56 years and weight 76.62 ± 10.59 Kgs. The data consist of 8 types of self-initiated falls of which 4 directed forward (falling on knees ending up lying, ending in lateral position, ending up lying, ending up lying with recovery) and 4 directed backward (falling sitting ending up lying, ending in lateral position, ending up lying, ending up lying with recovery). Every type of fall was performed 3 times by each participant while wearing a MARG (Magnetic Angular Rate and Gravity) multi-sensory device, tied to the waist. The duration of the trials was different for each fall, participant and trial. The required data consist of 14 parameters of which 5 were used in the analysis: time in 's' acceleration along the x, y and z-axis and squared vector magnitude measured in terms of gravitational acceleration in m/s^2. Results are presented for 8 fall subcategories and 3 phases as mean over 24 records (8 subjects and 3 simulation runs). The significance of the results is tested using Lilliefor's test setting $p < 0.05$. Total records processed are 192 (8 subcategories of falls, 24 records each).

9.4.4 Results and discussion

From the CRPs for pre-fall, fall and post-fall computed using 'ga' and 'p' the values of RR, DET and ENT are reported in Table−**??**. Comparing 'ga' and 'p' signals in Figure−9.6, the time section of activity with respect to the occurring fall action overlap. The confusion matrix of the result of the support vector machine is shown in Table−**??**. A detection rate of 70% and 82% was achieved for pre-fall and fall

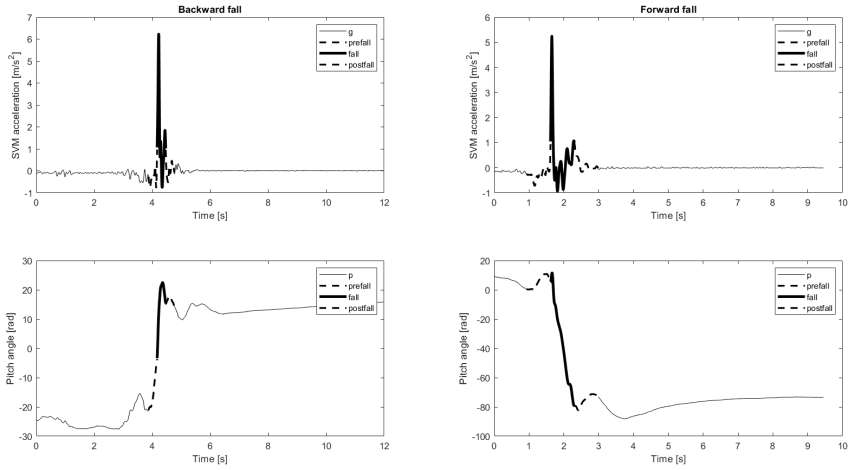

Figure 9.6: Input signals, (a) squared vector magnitude of 'g' and (b) pitch angle 'p', both thresholded on $g \leq 9.8m/s^2$ to represent pre-fall and post-fall phases and $g > 9.8m/s^2$ to define fall phase

respectively with overall classification accuracy of 76%.

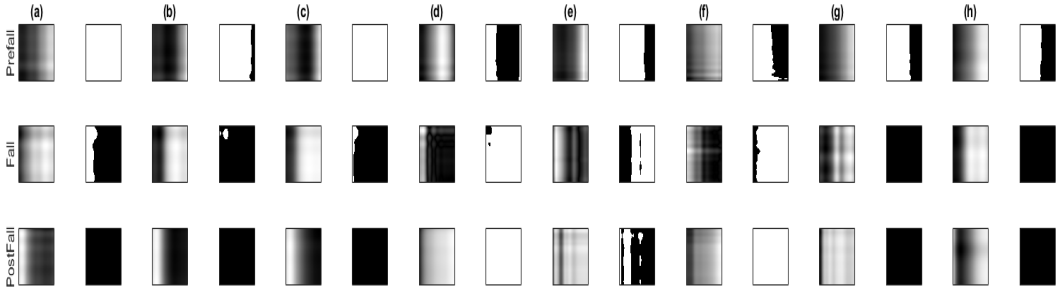

Figure 9.7: Cross recurrence plots for backward fall: (a) lateral, (b) lying, (c) lying recovery, (d) sitting, and for forward fall (e) knee lying, (f) lateral position, (g) lying, (h) lying recovery (left side: without threshold; right side: with threshold)

In addition to the squared vector magnitude 'ga' and 'p', other signals e.g. roll and yaw are available in the dataset. Different signal pairs were tried but 'ga' and 'p' gave the best result in case of the backward and forward fall types studied. Out of three angles available, 'p' was observed to have more dynamics for both backward and forward fall cases. Mean values of recurrence rate for the fall activities are higher for the pre-fall section than the fall section.

Table−**??** shows the mean values of the recurrence metrics for each fall case calculated for 24 tests - 8 subjects and 3 trials each. In our analysis and discussion we only compare the sections pre-fall and fall since the aim of the study is to detect prefall and fall. The highest recurrence is seen for the pre-fall phase and least for the fall phase showing that the signal is least disrupted while pre-fall and highly disrupted for the fall event. High probability value for determinism depicts a less

chaotic subject movement and low probability value represents a more chaotic subject movement, hence representing a fall. High values of determinism are observed during the pre-fall states and low vales are reported during the fall states. High value of line entropy is reported in the case of pre-fall and low value in case of fall phase showing less signal disruption contained in the non-fall state and signal disruption during the fall state. Figure−9.7 shows CRPs for all eight kinds of falls i.e. backward fall: (a) lateral, (b) lying, (c) lying recovery, (d) sitting, and for forward fall (e) knee lying, (f) lateral position, (g) lying, (h) lying recovery for all three phases of fall. These output CRPs correspond to the inputs shown in Figure−9.6. Using the reason that detecting a pre-fall and fall event is more important leading to appropriate prevention measures, the SVM is set to classify only pre-fall and fall event. In the selection of the threshold, the tested values were in the range: 0.1 to 60 and selected the optimum that produced maximum overall accuracy at SVM output. Figure−9.7 also shows some similarity between different falls but it is seen distinctions are better made with the recurrence metrics as shown comparing for instance Figure−9.7 (panel g) and Figure−9.7 (panel h). Table−**??** shows confusion matrix for pre-fall and fall detection.

Table 9.4: Confusion matrix for pre-fall and fall using SVM

True/Predicted	Pre-fall	Fall
Pre-fall	67	29
Fall	17	79

Further studies on a larger population could improve the detection rate achieved through SVM using parameter optimization procedures. Application of more complex deep learning algorithms could improve the detection accuracy. Also since falls entail more profound changes in pitch recordings compared to roll and yaw, quantification analysis on pitch angle data alone can be studied and compared to the detection produced using CRPs of 'ga' and 'p' . In this study, RQA was performed to detect falls using data acquired through wearable sensors. The results show that using novel RQA features produces good fall detection rate of 70% and 82% for pre-fall and fall respectively which results in an overall detection rate of 76%. Hence, RQA features are able to well-characterize the dynamics of a fall.

Chapter 10

Discussion and conclusive remarks

The goal of this research was to understand the issues related to wearable biomedical sensors specifically wearable cardiovascular health monitoring devices for example, belt-type, patch-based, wrist-type, textile-based etc. Focusing on the wearable applications is highly significant for analyzing the various signal characteristics, guiding design decisions for wearable ECG devices as compared to clinical ECG machines because of a huge shift in the use of continuous monitoring wearable sensing devices nowadays.

ECG signals acquired from wearable devices are particularly corrupted by baseline wander, power line interference, skin-electrode contact interference and motion and muscle artifacts. Moreover, there exist a number of variations due to sensor-type such as placement (wrist, chest, other), electrode type (wet, dry) and coupling (AC, DC) etc. A large number of ECG datasets are available today (Physionet, AHA), most of which are clinical ECG data. Unfortunately, none of these datasets focus on wearable ECG applications, that is to say, no special attention has been paid to the unique conditions in wearable ECG computers, such as interference or electrode type, placement, and coupling.

In order to meet a medical standard and clinically accepted monitoring system, early detection of abnormal conditions, accurate decision support and high quality and real-time patient data acquisition need to be considered. ECG signals acquired using wearable sensors are often a source of inaccurate information due to noise especially signal distortions arising due to body movements of the patient or subject. Hence, designing diagnostic systems specifically for signals acquired using wearable ECG sensors becomes a challenge. The limitations mainly come from the fact that these technical algorithms commonly are data-driven and compute-intensive and hence imply a significant computing overhead, which necessitates the use of high-end hardware systems with high compute capability [1].

This research developed research solutions according to the above-mentioned problem statement. The major part of research focused on adapting Segmented Beat Modulation Method to:

1. non-sinus rhythm ventricular and supraventricular arrhythmic beats,

2. modern fast processing hardware with GPU-based architecture,

3. compressed ECG signals to increase the storage capacity of wearable sensors, and

4. heart rate variability, a factor that is different for different subjects and physiological conditions.

In the minor domain, the research proposed:

5. a cardiovascular disease diagnosis solution with optimized minimum number of features using Differential Evolution for optimization and Probabilistic Neural Networks for classification.

6. a couple of preliminary studies using Recurrence Quantification Analysis for modelling of human body movements in an attempt to better understand and characterize the human body movements acquired through wearable sensors.

The ESBMM is a template-based method for ECG denoising implemented as an extended and improved version of the existing SBMM [4, 39], which is able to denoise ECG tracings characterized by sinus as well as nonsinus rhythm. It operates in short-term ECG. In case of long-term ECG, it is applied to short ECG windows recursively extracted from the long recording. This design choice allows one to maintain physiological ECG variability (time and amplitude) by significantly reducing the level of noise. An physiologically improved cardiac cycle segmentation rule separating depolarization and ventricular repolarization parts of each cardiac cycle was used, the first part (i.e., the PQRS segment) includes the P wave and the QRS complex, while the second (i.e., TUP segment) includes the T and U waves, respectively. Consequently, they can be hypothesized to show a similar dependency of instantaneous heart rate. Moreover, evaluation of P-wave presence and morphology is fundamental for a beat classification (all supraventricular arrhythmias show abnormalities at P-wave level). Taking into account that the electrical activity of a cardiac beat starts with the P wave, when classifying a cardiac beat, its P wave has to be present in the segments representing it and not in the segments representing the previous one. A beat classification functional layer was added with features including temporal intervals (RR interval and CC duration) [93], features obtained applying discrete wavelet transform to the modulated CC (detail coefficients level 4 to 7) [90], and novel statistical features (kurtosis and skewness) [94]. Beat classification was performed using a 1D convolutional neural network which receives these temporal, spectral and morphological ECG features as input.

The MIT–BIH arrhythmia database was chosen because it allowed us to evaluate the performance of the ESBMM in beat classification, which is the main novelty of the ESBMM with respect to the SBMM. Compared with the state of the art methods [92, 93, 95, 96, 97, 98, 99, 100] tested on the same database using CC defining features and classification algorithms different than the one used in ESBMM proved the strength of ESBMM in classiying chosen nonsinus rhythm beats. De

Chazal et al. [101] used a simple feature set based on heartbeat and RR intervals plus wave morphology. Zhang et al. [93] presented a one-versus-one feature reduction strategy focusing on the disease-specific features supporting the traditional support vector machine binary classifier. Eventually, Chen et al. [92] proposed a combination of projected and dynamic features for arrhythmia classification and a support vector machine classifier to cluster heartbeats. All methods were able to reliably classify N and V beats, but only the ESBMM was also able to reliably classify S beats. Due to this additional beat classification procedure, three templates (instead of one, as for the SBMM) are computed, one for each beat class (N, S, and V). Each template is obtained by performing the median computation over all beats belonging to a class, an operation which is known to reduce noise and to provide the most likely morphology in a class of beats. In order to perform the median operator, all CC needs to be modulated to have the same length. Indeed, the hypothesis behind the procedure is that each beat of a class is a slight modification of a class specific morphology (best represented by the median, i.e., the template). Thus, the beat modulation is only an intermediate step to obtain a denoised template for each class. Template waveforms are then concatenated, demodulated, and adjusted in order to provide an output clean ECG tracing characterized by the same beat-to-beat heart-rate variability characterizing the input noisy ECG. The ESBMM's ability to denoise ECG tracings aas confirmed by the statistically significant improvement of the signal-to-noise ratio with maximum signal-to-noise improvement up to 6.08 dB. However, the ESBMM's robustness to corrupting factors such as baseline wanders, muscle activity, and electrode motion artifacts was also evaluated. The results confirmed the ability of the method to estimate good quality ECG recordings in the presence of typical noises affecting the ECG, especially for the N class, analogous to what was previously observed for the SBMM [4, 58].

Since in an ECG recording, the number of N beats is generally much higher than the number of S and V beats, the template of class N is typically much cleaner than the templates of class S and V. Consequently, PP(N) is much less affected by the presence of noise than PP(S) and PP(V). The numbers of false positives in V beats seems to be quite high. This effect could be due to the presence of bundle branch block beats in the class N, that could be erroneously classified in class V. Future studies will evaluate the possibility of including the bundle branch block beats in an additional fourth class, in order to solve this limitation of our approach.

DCT-SBMM produces almost the same output for both uncompressed and compressed ECG, while providing an advantage of 50% reduction (CR=2) in storage size. The presented DCT-SBMM proves to be efficient in terms of both compression and denoising and hence is applicable to ambulatory, online and wearable sensing applications to be used for long-term and continuous monitoring of patient ECG by the clinicians. A comparatively high standard deviation in all calculations was observed due to the analog recording process of the used database making the compression testing more stringent than necessary [109] and occurrence of different kinds

of abnormal beats in about 10% of the records processed. Moreover, it is observed that for too noisy input records, peak detection becomes difficult and results in some additional but wrong peaks, which again is a limitation in producing high SNR values whilst keeping useful signal information intact. DCT-SBMM was a preliminary test for ambulatory condition testing and more sophisticated compression algorithms may be tested in future to incorporate better compression ratio and less signal distortion. Moreover lossless compression schemes may by proposed and tested for even better results.

The GPU implementation reduces the runtime of the noise reduction algorithm from 4.82 s to 0.63 s. Hence, the speedup achieved is 7.67 times higher than that of the CPU-based SBMM implementation. Improvement in SNR showed that GPU-SBMM is an effective processing and analysis method for removal of exercise-induced noise factors in the TECG data measured from wearable sensors and might play an important role in the prevention of SRSCD [110] . For future recommendation, full benefits of parallelism for GPU-SBMM might be seen when used with big data (larger datasets or online ECG data processing).

Dynamic-template SBMM presented an improved version of SBMM considering motion artifacts induced during different daily life activities. Highest level of denoising is achieved when the level of input noise is high (-5dB), good noise cancellation when the input signal is assumed to contain an average level of noise and least SNR improvement when the level of noise is low. For AC and DC coupling cases, the algorithm shows a good enough denoising for high level of input noise (-5dB) but shows a poor signal denoising in case of medium (0dB) and low (5dB) levels of input noise. The activity-wise analysis for the proposed algorithm shows a good SNR improvement for activities, drinking coffee, typing keyboard, pressing and releasing electrode, walking at 1 mph, walking at 3 mph, but for the activities highly disrupting the input signal i.e walking at relatively high speed (3 mph), running both at 5 and 7 mph, the reconstructed signal shows a negation of noise as well as useful signal. Hence, future studies are projected at specifically modelling the motion artifacts if possible and deleting them from the raw signal to get an even better result.

For efficient processing with optimally reduced features, a metaheuristic search algorithm Differential Evolution (DE) was modelled to optimize direct ECG beat amplitude features to maximize MCC for 8 cardiac beat classes having imbalanced and uncorrelated class distributions. An optimized feature subset was obtained which was then used with a simple and PNN classifier. The proposed method achieved 83.79% (41 out of total 253 CC defining amplitude points) reduction in directly acquired features with comparable classification performance. More than 100,000 ECG heartbeats were processed with eight types of ECG beats including one normal and seven arrhythmic beats. The DE-PNN scheme could classify normal with an accuracy of 99.45%, premature ventricular contraction with 99.18%, paced with 100.00%, right bundle branch block with 99.94%, left bundle branch block with 99.80%, atrial premature with 99.76%, ventricular flutter with 99.61%, and ventricular

escape condition with 99.94% accuracy. The average number of generations by which the optimization is achieved was 78±12. The algorithm is inherently tuned to find an optimum reduced combination of features that performs better as compared to all features. Using PNN for classifying abnormal heartbeats using reduced direct signal features skips the computation of secondary features, produces higher classification performance due to removal of unnecessary features and faster due to reduced features and less time-consuming learning algorithm. Overall the achieved ECG arrhythmia classification result indicated that detection of arrhythmia using 16.21% features of a complete ECG heartbeat can be an effective approach to help general physicians and cardiology specialists to diagnose critical cardiovascular diseases in a continuous and long-term, online or offline monitoring scenarios particularly well-suited for a wearable sensing setting. The algorithm has currently been tested for 1 normal and 7 arrhythmia classes. A future research may extend the recognition to 16 classes (1 normal and 15 arrhythmic) for which the annotations are available in the MIT-BIH dataset. A future DE-optimization may focus on a multi-objective approach to maximizing accuracy whilst minimizing percentage signal distortion (accuracy and compression being the two objective functions) to make the signal usable for automatic system while having a good signal reproducibility for clinical analysis.

In an attempt to understand and model motion artifact which is the biggest source of noise particularly affecting wearable sensing input data, 3 basic tests were conducted using RQA, a technique is used to differentiate and analyze the regular and irregular parts of a time-series signal using recurrence plots and quantification measures. The first study presents RQA for human body movements during routine ADL using parameters recorded using a wearable sensor attached to the test subject's waist. The RQA parameters reveal a chaotic behavior in case of activity (RR=0.249, DET=0.510, ENT=0.732), and a stable or least chaotic behavior in case of non-activity (RR=0.466, DET=0.726, ENT=1.205) regions of time. Distinguishing values for RQA-based measures for different human body movements taking place during ADLs. The second study presented RQA of multiple ECG time series simultaneously recorded through different electrodes and depicts the effect of motion artifacts through electrode synchronization and non-synchronization. The ECG data was acquired from a healthy 25-year-old male performing different exercise activities such as standing, walking and jumping. with the electrode placed at offset angles 0, 45 and 90 degrees. Highest and second highest disturbances with respect to exercise movements were observed for electrode combinations (3,4) and (1,4). Distinguishing values for RQA-based measures for different exercise movements, lying and then standing, picking up something and standing, sitting and standing, stepping up and down and walking suggest that RQA is a powerful tool for differentiation of regular and irregular states occurring due to motion artifacts in the temporal patterns of ECG. The third and most recent work presents RQA parameters as novel features for characterization of a fall event in case of backward and forward types of falls using data acquired through wearable sensors. To assess the discriminating capability of novel recurrence

features, SVM was used to perform binary classification for pre-fall and fall classes. The SVM results in overall accuracy of 76% with a positive prediction of 82% for fall and 70% for pre-fall events. The results indicated that recurrence metrics are successfully able to characterize a sudden fall event and could be used in designing fall detection algorithms using wearable sensors.

This work particularly focused on dealing with wearable sensing data for automatic cardiovascular disease diagnosis. We mainly developed ESBMM as an efficient denoising and accurate diagnostic procedure for diagnosing ventricular and supraventricular arrhythmia. Focusing on real world usage scenarios for wearable sensing devices, different improvements including DCT-SBMM a data compression for analog recorded data with high levels of noise, GPU-SBMM, a fast hardware implementation for SRSCD application and dynamic-SBMM for physiological data in daily life activities were developed and tested. DE-PNN further improves the accuracy of disease diagnosis by detecting 7 types of arrhythmic heartbeats in an efficient manner. RQA studies enable an insight into characterization of motion artifact noise to model and remove it from the raw acquired physiological specifically ECG data. Hence it is concluded that the presented work successfully increases the utility of wearable ECG sensors to make them an efficient and reliable diagnostic tool in everyday cardiovascular health and disease monitoring scenarios.

List of Publications

Journal papers

1. Nasim, A., Sbrollini, A., Morettini, M. and Burattini, L., 2020. Extended Segmented Beat Modulation Method for Cardiac Beat Classification and Electrocardiogram Denoising. Electronics, 9(7), p.1178.

2. Sbrollini, A., Morettini, M., Maranesi, E., Marcantoni, I., Nasim, A., Bevilacqua, R., Riccardi, G.R. and Burattini, L., 2019. Sport Database: Cardiorespiratory data acquired through wearable sensors while practicing sports. Data in brief, 27, p.104793.

3. Nasim, A., Burattini, L., Fateh, M.F. and Zameer, A., 2019. Solution of linear and non-linear boundary value problems using population-distributed parallel differential evolution. Journal of Artificial Intelligence and Soft Computing Research, 9(3), pp.205-218.

4. Nasim, A., Sbrollini, A., Morettini, M. and Burattini, L., 2020. DE-PNN: Differential Evolution-based feature optimization with Probabilistic Neural Network for heartbeat classification. Submitted.

Book chapter

1. Burattini, L., Marcantoni, I., Nasim, A., Burattini, L., Morettini, M. and Sbrollini, A., T-Wave Alternans Identification in Direct and Indirect Fetal Electrocardiography. In Innovative Technologies and Signal Processing in Perinatal Medicine (pp. 169-185). Springer, Cham.

Conference papers

1. Nasim, A., Sbrollini, A., Marcantoni, I., Morettini, M. and Burattini, L., 2019, July. Compressed Segmented Beat Modulation Method using Discrete Cosine Transform. In 2019 41st Annual International Conference of the IEEE Engineering in Medicine and Biology Society (EMBC) (pp. 2273-2276). IEEE.

2. Nasim, A., Pinti, F., Gentili, A., Belli, A., Palma, L. and Pierleoni, P., 2019, August. Dynamic Segmented Beat Modulation Method for Denoising ECG Data from Wearable Sensors. In 2019 International Conference on Sensing and Instrumentation in IoT Era (ISSI) (pp. 1-4). IEEE.

3. Nasim, A., Della Santa, E., Tanchi, D., Sbrollini, A., Marcantoni, I., Morettini, M. and Burattini, L., 2018, September. GPU-Based Segmented-Beat Modulation Method for Denoising Athlete Electrocardiograms During Training. In 2018 Computing in Cardiology Conference (CinC) (Vol. 45, pp. 1-4). IEEE.

4. Nasim, A., Marcantoni, I., Sbrollini, A., Morettini, M. and Burattini, L., 2019, June. Recurrence Quantification Analysis for Motion Artifacts in Wearable ECG Sensors. In 2019 IEEE 23rd International Symposium on Consumer Technologies (ISCT) (pp. 206-209). IEEE.

5. Nasim, A., Morettini, M., Marcantoni, I., Sbrollini, A. and Burattini, L., 2019, June. Recurrence Analysis of Human Body Movements during Activities of Daily Living. In 2019 IEEE 23rd International Symposium on Consumer Technologies (ISCT) (pp. 157-160). IEEE.

6. Nasim, A., Nchekwube, D., Khorasani, E., Van der Maaden, N., Morettini, M., Burattini L., 2020, June. Novel recurrence features for prefall and fall detection in backward and forward fall types. In VII Congress of the National Group of Bioengineering (GNB).

7. Marcantoni, I., Laratta, R., Mascia, G., Ricciardi, L., Sbrollini, A., Nasim, A., Morettini, M. and Burattini, L., 2019, July. Dofetilide-Induced Microvolt T-Wave Alternans. In 2019 41st Annual International Conference of the IEEE Engineering in Medicine and Biology Society (EMBC) (pp. 95-98). IEEE.

8. Sbrollini, A., Marcantoni, I., Nasim, A., Morettini, M. and Burattini, L., 2019, June. Electrocardiogram-Derived Respiratory Signal in Sleep Apnea by Segmented Beat Modulation Method. In 2019 IEEE 23rd International Symposium on Consumer Technologies (ISCT) (pp. 279-282). IEEE.

9. Sbrollini, A., Caraceni, G., Nasim, A., Marcantoni, I., Morettini, M., Belli, A., Pierleoni, P. and Burattini, L., 2019, June. Self-monitoring of cardiac risk while running around Ancona. In 2019 IEEE 23rd International Symposium on Consumer Technologies (ISCT) (pp. 1-4). IEEE.

List of abbreviations

CVD Cardiovascular Diseases
WHO World Health Organization
NCD Non-communicable diseases
LDL Low-density lipoprotein
HDL High-density lipoprotein
CT Computerized Tomography
MRI Magnetic Resonance Imaging
ECG Electrocardiogram
WSN Wireless Sensor Networks
SBMM Segmented Beat Modulation Method
ESBMM Extended Segmented Beat Modulation Method
GPU Graphical Processing Unit
GPU-SBMM GPU-based Segmented Beat Modulation Method
DCT Discrete Cosine Transform
DCT-SBMM DCT compressed Segmented Beat Modulation Method
Dynamic-SBMM Dynamic template Segmented Beat Modulation Method
CNN Convolutional Neural Network
PNN Probabilistic Neural Network
DE Differential Evolution
HR Heart Rate
HRV Heart Rate Variability
RQA Recurrence Quantification Analysis
SA Sinoatrial
Bpm beats per minute
AV Atrioventricular
P Permeability
FIR Finite Impulse Response
PI Powerline Interference
AC Alternating Current
DC Direct Current
CC Cardiac Cycle
RP Recurrence Plot
SEMG Surface Electromyography
SNR Signal-to-Noise Ratio
CR Compression Ratio
SISD Single Instruction Single Data
SIMD Single Instruction Multiple Data
SRSCD Sport-Related Sudden Cardiac Death
TECG ECG recordings acquired during Training
LRB Low-Resistance Bike

HRB High-Resistance Bike
PPG Photoplethesmogram
NSR Normal Sinus Rhythm
IoT Internet-of-Things
AAL Ambient Assisted Living
CAD Computer Aided Design
LSTM Long Short Term Memory
SVM Support Vector Machine
ADL Activities of Daily Living
CRP Cross Recurrence Plot
FECG Fetal Electrocardiogram
MECG Maternal Electrocardiogram
NEMG Needle Electromyography
FWEMG Fine-wire Electromyography
PSD Power Spectral Density
LF Linear Filtering
FFT Fast Fourier Transform
RR Recurrence Rate
DET Determinism
ENT Entropy
L Average diagonal length

Bibliography

[1] Adam Gacek and Witold Pedrycz. *ECG signal processing, classification and interpretation: a comprehensive framework of computational intelligence*. Springer Science & Business Media, 2011.

[2] Daniel C Sigg, Paul A Iaizzo, Yong-Fu Xiao, and Bin He. *Cardiac electrophysiology methods and models*. Springer Science & Business Media, 2010.

[3] Conduction system tutorial.

[4] Angela Agostinelli, Corrado Giuliani, and Laura Burattini. Extracting a clean ecg from a noisy recording: a new method based on segmented-beat modulation. In *In Proceedings of the Computing in Cardiology Conference (CinC 2014), Cambridge, USA, 7-10 September 2014*, pages 49–52. IEEE, 2014.

[5] Enas W Abdulhay, Rami J Oweis, Asal M Alhaddad, Fadi N Sublaban, Mahmoud A Radwan, and Hiyam M Almasaeed. Monitoring techniques. *Biomedical Science*, 2(3):53–67, 2014.

[6] Angela Agostinelli, Agnese Sbrollini, Luca Burattini, Sandro Fioretti, Francesco Di Nardo, and Laura Burattini. Noninvasive fetal electrocardiography part ii: Segmented-beat modulation method for signal denoising. *The open biomedical engineering journal*, 11:25–35, 2017.

[7] Emg biofeedback, indications and contraindications, electrode application sites.

[8] Kenneth Price, Rainer M Storn, and Jouni A Lampinen. *Differential evolution: a practical approach to global optimization*. Springer Science & Business Media, 2006.

[9] Donald F Specht. Probabilistic neural networks. *Neural networks*, 3(1):109–118, 1990.

[10] Shanthi Mendis, Pekka Puska, Bo Norrving, World Health Organization, et al. *Global atlas on cardiovascular disease prevention and control*. World Health Organization, 2011.

[11] Tobacco use and exposure to second-hand smoke linked to more than 20% of deaths from coronary heart disease.

[12] Emelia J Benjamin, Michael J Blaha, Stephanie E Chiuve, Mary Cushman, Sandeep R Das, Rajat Deo, Sarah D De Ferranti, James Floyd, Myriam Fornage, Cathleen Gillespie, et al. Heart disease and stroke statistics—2017 update. 2017.

[13] Angela Fehr, Mariken J Tijhuis, Sabrina Hense, Dominika Urbanski, Peter Achterberg, and Thomas Ziese. European core health indicators-status and perspectives. *Archives of Public Health*, 76(1):52, 2018.

[14] Alcohol use and your health.

[15] Nancy T Artinian, Gerald F Fletcher, Dariush Mozaffarian, Penny Kris-Etherton, Linda Van Horn, Alice H Lichtenstein, Shiriki Kumanyika, William E Kraus, Jerome L Fleg, Nancy S Redeker, et al. Interventions to promote physical activity and dietary lifestyle changes for cardiovascular risk factor reduction in adults: a scientific statement from the american heart association. *Circulation*, 122(4):406–441, 2010.

[16] Global cardiology network.

[17] NCD Risk. Factor collaboration (ncd-risc). trends in adult body-mass index in 200 countries from 1975 to 2014: a pooled analysis of 1698 population-based measurement studies with 19.2 million participants. *Lancet*, 387(10026):1377–1396, 2016.

[18] Vasanti S Malik, Walter C Willett, and Frank B Hu. Global obesity: trends, risk factors and policy implications. *Nature Reviews Endocrinology*, 9(1):13–27, 2013.

[19] Mirza Mansoor Baig, Hamid Gholamhosseini, and Martin J Connolly. A comprehensive survey of wearable and wireless ecg monitoring systems for older adults. *Medical & biological engineering & computing*, 51(5):485–495, 2013.

[20] Clare Davenport, Elaine Yee Lan Cheng, Yip Tung Tony Kwok, Annie Hiu On Lai, Taka Wakabayashi, Chris Hyde, and Martin Connock. Assessing the diagnostic test accuracy of natriuretic peptides and ecg in the diagnosis of left ventricular systolic dysfunction: a systematic review and meta-analysis. *British Journal of General Practice*, 56(522):48–56, 2006.

[21] Joseph J Oresko, Zhanpeng Jin, Jun Cheng, Shimeng Huang, Yuwen Sun, Heather Duschl, and Allen C Cheng. A wearable smartphone-based platform for real-time cardiovascular disease detection via electrocardiogram processing. *IEEE Transactions on Information Technology in Biomedicine*, 14(3):734–740, 2010.

[22] Paddy M Barrett, Ravi Komatireddy, Sharon Haaser, Sarah Topol, Judith Sheard, Jackie Encinas, Angela J Fought, and Eric J Topol. Comparison of 24-hour holter monitoring with 14-day novel adhesive patch electrocardiographic monitoring. *The American journal of medicine*, 127(1):95–e11, 2014.

[23] Zephyr. Bioharness 3.0 user manual, 2012.

[24] Goris Nazari, Pavlos Bobos, Joy C MacDermid, Kathryn E Sinden, Julie Richardson, and Ada Tang. Psychometric properties of the zephyr bioharness device: a systematic review. *BMC Sports Science, Medicine and Rehabilitation*, 10(1):6, 2018.

[25] Luca Pollonini, Nithin O Rajan, Shuai Xu, Sridhar Madala, and Clifford C Dacso. A novel handheld device for use in remote patient monitoring of heart failure patients—design and preliminary validation on healthy subjects. *Journal of medical systems*, 36(2):653–659, 2012.

[26] Keri J Heilman, Mika Handelman, Gregory Lewis, and Stephen W Porges. Accuracy of the stresseraser® in the detection of cardiac rhythms. *Applied psychophysiology and biofeedback*, 33(2):83–89, 2008.

[27] E Sardini and M Serpelloni. Instrumented wearable belt for wireless health monitoring. *Procedia Engineering*, 5:580–583, 2010.

[28] Gregorio López, Víctor Custodio, and José Ignacio Moreno. Lobin: E-textile and wireless-sensor-network-based platform for healthcare monitoring in future hospital environments. *IEEE Transactions on Information Technology in Biomedicine*, 14(6):1446–1458, 2010.

[29] Philippe Jourand, Hans De Clercq, Rogier Corthout, and Robert Puers. Textile integrated breathing and ecg monitoring system. *Procedia Chemistry*, 1(1):722–725, 2009.

[30] Young-Dong Lee and Wan-Young Chung. Wireless sensor network based wearable smart shirt for ubiquitous health and activity monitoring. *Sensors and Actuators B: Chemical*, 140(2):390–395, 2009.

[31] Anna Maria Bianchi, Martin Oswaldo Mendez, and Sergio Cerutti. Processing of signals recorded through smart devices: sleep-quality assessment. *IEEE Transactions on Information Technology in Biomedicine*, 14(3):741–747, 2010.

[32] Jerald Yoo, Long Yan, Seulki Lee, Hyejung Kim, and Hoi-Jun Yoo. A wearable ecg acquisition system with compact planar-fashionable circuit board-based shirt. *IEEE Transactions on Information Technology in Biomedicine*, 13(6):897–902, 2009.

[33] Shirley Coyle, King-Tong Lau, Niall Moyna, Donal O'Gorman, Dermot Diamond, Fabio Di Francesco, Daniele Costanzo, Pietro Salvo, Maria Giovanna Trivella, Danilo Emilio De Rossi, et al. Biotex—biosensing textiles for personalised healthcare management. *IEEE transactions on information technology in biomedicine*, 14(2):364–370, 2010.

[34] Fabio Buttussi and Luca Chittaro. Mopet: A context-aware and user-adaptive wearable system for fitness training. *Artificial Intelligence in Medicine*, 42(2):153–163, 2008.

[35] Michael Winterhalter, Jörg Schiller, Sinika Münte, Michael Bund, Ludwig Hoy, Christoph Weilbach, Siegfried Piepenbrock, and Niels Rahe-Meyer. Prospective investigation into the influence of various stressors on skin impedance. *Journal of clinical monitoring and computing*, 22(1):67–74, 2008.

[36] Merja Puurtinen, Jari Viik, and Jari Hyttinen. Best electrode locations for a small bipolar ecg device: signal strength analysis of clinical data. *Annals of biomedical engineering*, 37(2):331–336, 2009.

[37] Daniel Scherr, Darshan Dalal, Charles A Henrikson, David D Spragg, Ronald D Berger, Hugh Calkins, and Alan Cheng. Prospective comparison of the diagnostic utility of a standard event monitor versus a "leadless" portable ecg monitor in the evaluation of patients with palpitations. *Journal of Interventional Cardiac Electrophysiology*, 22(1):39–44, 2008.

[38] Youngzoon Yoon, Jung H Cho, and Gilwon Yoon. Non-constrained blood pressure monitoring using ecg and ppg for personal healthcare. *Journal of medical systems*, 33(4):261–266, 2009.

[39] Angela Agostinelli, Corrado Giuliani, Sandro Fioretti, Francesco Di Nardo, and Laura Burattini. Robustness of the segmented-beat modulation method to noise. In *In Proceedings of the 2015 Computing in Cardiology Conference (CinC)*, pages 205–208. IEEE, 2015.

[40] Agnese Sbrollini, Annachiara Strazza, Silvia Candelaresi, Ilaria Marcantoni, Micaela Morettini, Sandro Fioretti, Francesco Di Nardo, and Laura Burattini. Surface electromyography low-frequency content: Assessment in isometric conditions after electrocardiogram cancellation by the segmented-beat modulation method. *Informatics in Medicine Unlocked*, 13:71–80, 2018.

[41] Benedetta Pambianco, Agnese Sbrollini, Ilaria Marcantoni, Micaela Morettini, Sandro Fioretti, and Laura Burattini. Electrocardiogram derived respiratory signal through the segmented-beat modulation method. In *2018 40th Annual International Conference of the IEEE Engineering in Medicine and Biology Society (EMBC)*, pages 5681–5684. IEEE, 2018.

[42] M Cremer. Munchen. med weknschr 53: 811, 1906. cited in wh brown, a study of the esophageal lead in clinical electrocardiography. *Am Heart J.*

[43] David E Goldman. Potential, impedance, and rectification in membranes. *The Journal of general physiology*, 27(1):37–60, 1943.

[44] Alan L Hodgkin and Bernard Katz. The effect of sodium ions on the electrical activity of the giant axon of the squid. *The Journal of physiology*, 108(1):37, 1949.

[45] Ankit Jayant, Tripti Singh, and Manpreet Kaur. Different techniques to remove baseline wander from ecg signal. *International Journal of Emerging Research in Management and Technology*, 2(6):16–9, 2013.

[46] Staffan Bruce, KJ Vandamme, and Anders Rydberg. Temperature dependence and electrical properties of dominant low-frequency noise source in sige hbt. *IEEE Transactions on Electron Devices*, 47(5):1107–1112, 2000.

[47] Yue-Der Lin and Yu Hen Hu. Power-line interference detection and suppression in ecg signal processing. *IEEE Transactions on Biomedical Engineering*, 55(1):354–357, 2007.

[48] Richard F Santopietro. The origin and characterization of the primary signal, noise, and interference sources in the high frequency electrocardiogram. *Proceedings of the IEEE*, 65(5):707–713, 1977.

[49] Mireya Fernández-Chimeno, Marcos Quílez, and Fernando Silva. Understanding electrosurgical unit perturbations in order to address hospital operating room electromagnetic compatibility. *IEEE transactions on biomedical engineering*, 53(6):1206–1209, 2006.

[50] Raquel Bailón, Leif Sornmo, and Pablo Laguna. A robust method for ecg-based estimation of the respiratory frequency during stress testing. *IEEE transactions on biomedical engineering*, 53(7):1273–1285, 2006.

[51] Dale Dubin. *Rapid interpretation of EKG's: an interactive course.* Cover Publishing Company, 2000.

[52] Elizabeth Atkinson, Bridget Mikysa, Jeffrey A Conway, Morgan Parker, Karla Christian, Jayant Deshpande, Timothy Kevin Knilans, Jacqueline Smith, Carolyn Walker, Ronald E Stickney, et al. Specificity and sensitivity of automated external defibrillator rhythm analysis in infants and children. *Annals of emergency medicine*, 42(2):185–196, 2003.

[53] Pamela J McCabe, Shauna Schad, Andrea Hampton, and Diane E Holland. Knowledge and self-management behaviors of patients with recently detected atrial fibrillation. *Heart & Lung*, 37(2):79–90, 2008.

[54] U Rajendra Acharya, Shu Lih Oh, Yuki Hagiwara, Jen Hong Tan, Muhammad Adam, Arkadiusz Gertych, and Ru San Tan. A deep convolutional neural network model to classify heartbeats. *Computers in biology and medicine*, 89:389–396, 2017.

[55] Tiago P Almeida, Fernando S Schlindwein, João Salinet, Xin Li, Gavin S Chu, Jiun H Tuan, Peter J Stafford, G André Ng, and Diogo C Soriano. Characterization of human persistent atrial fibrillation electrograms using recurrence quantification analysis. *Chaos: An Interdisciplinary Journal of Nonlinear Science*, 28(8):085710, 2018.

[56] José García, L Sornmo, Salvador Olmos, and Pablo Laguna. Automatic detection of st-t complex changes on the ecg using filtered rms difference series: application to ambulatory ischemia monitoring. *IEEE Transactions on Biomedical Engineering*, 47(9):1195–1201, 2000.

[57] Javier Mateo and Pablo Laguna. Improved heart rate variability signal analysis from the beat occurrence times according to the ipfm model. *IEEE Transactions on Biomedical Engineering*, 47(8):985–996, 2000.

[58] Angela Agostinelli, Agnese Sbrollini, Corrado Giuliani, Sandro Fioretti, Francesco Di Nardo, and Laura Burattini. Segmented beat modulation method for electrocardiogram estimation from noisy recordings. *Medical engineering & physics*, 38(6):560–568, 2016.

[59] Marek Malik, Katerina Hnatkova, Martina Sisakova, and Georg Schmidt. Subject-specific heart rate dependency of electrocardiographic qt, pq, and qrs intervals. *Journal of electrocardiology*, 41(6):491–497, 2008.

[60] Ary L Goldberger, Luis AN Amaral, Leon Glass, Jeffrey M Hausdorff, Plamen Ch Ivanov, Roger G Mark, Joseph E Mietus, George B Moody, Chung-Kang Peng, and H Eugene Stanley. Physiobank, physiotoolkit, and physionet: components of a new research resource for complex physiologic signals. *circulation*, 101(23):e215–e220, 2000.

[61] George B Moody, W Muldrow, and Roger G Mark. A noise stress test for arrhythmia detectors. *Computers in cardiology*, 11(3):381–384, 1984.

[62] Otto Rompelman and HH Ros. Coherent averaging technique: A tutorial review part 1: Noise reduction and the equivalent filter. *Journal of biomedical engineering*, 8(1):24–29, 1986.

[63] Jiapu Pan and Willis J Tompkins. A real-time qrs detection algorithm. *IEEE transactions on biomedical engineering*, (3):230–236, 1985.

[64] Maurizio Varanini, Gennaro Tartarisco, Rita Balocchi, Alberto Macerata, Giovanni Pioggia, and Lucia Billeci. A new method for qrs complex detection in multichannel ecg: Application to self-monitoring of fetal health. *Computers in biology and medicine*, 85:125–134, 2017.

[65] Angela Agostinelli, Ilaria Marcantoni, Elisa Moretti, Agnese Sbrollini, Sandro Fioretti, Francesco Di Nardo, and Laura Burattini. Noninvasive fetal electrocardiography part i: Pan-tompkins' algorithm adaptation to fetal r-peak identification. *The open biomedical engineering journal*, 11:17, 2017.

[66] G Mihaela Ungureanu, Johannes WM Bergmans, S Guid Oei, Alexandru Ungureanu, and Werner Wolf. The event synchronous canceller algorithm removes maternal ecg from abdominal signals without affecting the fetal ecg. *Computers in biology and medicine*, 39(6):562–567, 2009.

[67] Janusz Jezewski, Adam Matonia, Tomasz Kupka, Dawid Roj, and Robert Czabanski. Determination of fetal heart rate from abdominal signals: evaluation of beat-to-beat accuracy in relation to the direct fetal electrocardiogram. *Biomedical Engineering/Biomedizinische Technik*, 57(5):383–394, 2012.

[68] GT Allison. Trunk muscle onset detection technique for emg signals with ecg artefact. *Journal of Electromyography and Kinesiology*, 13(3):209–216, 2003.

[69] S.L. Pullman, D.S. Goodin, A.I. Marquinez, S. Tabbal, and M. Rubin. Clinical utility of surface emg. *Neurology*, 55(2):171–177, 2000.

[70] B Jonsson, M Omfeldt, and A Rundgren. Discomfort from the use of wire electrodes for electromyography. *Electromyography*, 8(1):5, 1968.

[71] H Yeom and U Yoon. Ecg artifact removal from surface emg using adaptive filter algorithm. *International Journal of Multimedia and Ubiquitous Engineering*, 7(2):533–537, 2012.

[72] Charles E Kossmann, Daniel A Brody, George E Burch, Hans H Hecht, FRANKLIN D JOHNSTON, Calvin Kay, Eugene Lepeschkin, HUBERT V PIPBERGER, HUBERT V PIPBERGER, Gerhard Baule, et al. Recommendations for standardization of leads and of specifications for instruments in electrocardiography and vectorcardiography. *Circulation*, 35(3):583–602, 1967.

[73] Ivaylo I Christov and Ivan K Daskalov. Filtering of electromyogram artifacts from the electrocardiogram. *Medical engineering & physics*, 21(10):731–736, 1999.

[74] Marzieh Golabbakhsh, Monire Masoumzadeh, and Mohammad Farzan Sabahi. Ecg and power line noise removal from respiratory emg signal using adaptive filters. *Majlesi Journal of Electrical Engineering*, 5(4), 2011.

[75] Guohua Lu, John-Stuart Brittain, Peter Holland, John Yianni, Alexander L Green, John F Stein, Tipu Z Aziz, and Shouyan Wang. Removing ecg noise from surface emg signals using adaptive filtering. *Neuroscience letters*, 462(1):14–19, 2009.

[76] C Marque, C Bisch, R Dantas, S Elayoubi, V Brosse, and C Perot. Adaptive filtering for ecg rejection from surface emg recordings. *Journal of electromyography and kinesiology*, 15(3):310–315, 2005.

[77] Sara Abbaspour and Ali Fallah. Removing ecg artifact from the surface emg signal using adaptive subtraction technique. *Journal of biomedical physics & engineering*, 4(1):33, 2014.

[78] Yong Hu, XH Li, XB Xie, LY Pang, Yuzhen Cao, and KDK Luk. Applying independent component analysis on ecg cancellation technique for the surface recording of trunk electromyography. In *2005 IEEE Engineering in Medicine and Biology 27th Annual Conference*, pages 3647–3649. IEEE, 2006.

[79] Yong Hu, Joseph Mak, Hongtao Liu, and Keith DK Luk. Ecg cancellation for surface electromyography measurement using independent component analysis. In *2007 IEEE International Symposium on Circuits and Systems*, pages 3235–3238. IEEE, 2007.

[80] Yun Li, Xiang Chen, Xu Zhang, and Ping Zhou. Ecg artifact removal from emg recordings using independent component analysis and adapted filter. In *2013 6th International IEEE/EMBS Conference on Neural Engineering (NER)*, pages 347–350. IEEE, 2013.

[81] Joseph NF Mak, Yong Hu, and KDK Luk. Ica-based ecg removal from surface electromyography and its effect on low back pain assessment. In *2007 3rd International IEEE/EMBS Conference on Neural Engineering*, pages 646–649. IEEE, 2007.

[82] François Nougarou, Daniel Massicotte, and Martin Descarreaux. Efficient procedure to remove ecg from semg with limited deteriorations: Extraction, quasi-periodic detection and cancellation. *Biomedical Signal Processing and Control*, 39:1–10, 2018.

[83] Mohammad Shahbakhti, Elnaz Heydari, and Gia Thien Luu. Segmentation of ecg from surface emg using dwt and emd: a comparison study. *Fluctuation and Noise Letters*, 13(04):1450030, 2014.

[84] Nadica Miljković, Nenad Popović, Olivera Djordjević, Ljubica Konstantinović, and Tomislav B Šekara. Ecg artifact cancellation in surface emg signals by fractional order calculus application. *Computer methods and programs in biomedicine*, 140:259–264, 2017.

[85] PW Duncan and I Wether. K., chandler, j. and studenski, s., functional reach: a new clinical measure of balance. *J. Gerontol*, 45:M192, 1990.

[86] Roland Kadefors, Holger Broman, and Carlo J de Luca. Units, terms and standards in the reporting of emg research. 1980.

[87] David Caggiano and Stanley Reisman. Respiration derived from the electrocardiogram: a quantitative comparison of three different methods. In *Proceedings of the IEEE 22nd Annual Northeast Bioengineering Conference*, pages 103–104. IEEE, 1996.

[88] MA García-González, A Argelagós, Mireya Fernández-Chimeno, and J Ramos-Castro. Differences in qrs locations due to ecg lead: relationship with breathing. In *XIII Mediterranean Conference on Medical and Biological Engineering and Computing 2013*, pages 962–964. Springer, 2014.

[89] George B Moody and Roger G Mark. The impact of the mit-bih arrhythmia database. *IEEE Engineering in Medicine and Biology Magazine*, 20(3):45–50, 2001.

[90] Babak Mohammadzadeh Asl, Seyed Kamaledin Setarehdan, and Maryam Mohebbi. Support vector machine-based arrhythmia classification using reduced features of heart rate variability signal. *Artificial intelligence in medicine*, 44(1):51–64, 2008.

[91] Nitesh V Chawla, Kevin W Bowyer, Lawrence O Hall, and W Philip Kegelmeyer. Smote: synthetic minority over-sampling technique. *Journal of artificial intelligence research*, 16:321–357, 2002.

[92] Shanshan Chen, Wei Hua, Zhi Li, Jian Li, and Xingjiao Gao. Heartbeat classification using projected and dynamic features of ecg signal. *Biomedical Signal Processing and Control*, 31:165–173, 2017.

[93] Zhancheng Zhang, Jun Dong, Xiaoqing Luo, Kup-Sze Choi, and Xiaojun Wu. Heartbeat classification using disease-specific feature selection. *Computers in biology and medicine*, 46:79–89, 2014.

[94] Jinyuan He, Le Sun, Jia Rong, Hua Wang, and Yanchun Zhang. A pyramid-like model for heartbeat classification from ecg recordings. *PloS one*, 13(11):e0206593, 2018.

[95] Roshan Joy Martis, U Rajendra Acharya, and Lim Choo Min. Ecg beat classification using pca, lda, ica and discrete wavelet transform. *Biomedical Signal Processing and Control*, 8(5):437–448, 2013.

[96] Can Ye, BVK Vijaya Kumar, and Miguel Tavares Coimbra. Heartbeat classification using morphological and dynamic features of ecg signals. *IEEE Transactions on Biomedical Engineering*, 59(10):2930–2941, 2012.

[97] Mehmet Korürek and Berat Doğan. Ecg beat classification using particle swarm optimization and radial basis function neural network. *Expert systems with Applications*, 37(12):7563–7569, 2010.

[98] Sung-Nien Yu and Kuan-To Chou. Integration of independent component analysis and neural networks for ecg beat classification. *Expert Systems with Applications*, 34(4):2841–2846, 2008.

[99] Philip De Chazal and Richard B Reilly. A patient-adapting heartbeat classifier using ecg morphology and heartbeat interval features. *IEEE transactions on biomedical engineering*, 53(12):2535–2543, 2006.

[100] Santanu Sahoo, Bhupen Kanungo, Suresh Behera, and Sukanta Sabut. Multiresolution wavelet transform based feature extraction and ecg classification to detect cardiac abnormalities. *Measurement*, 108:55–66, 2017.

[101] Philip De Chazal, Maria O'Dwyer, and Richard B Reilly. Automatic classification of heartbeats using ecg morphology and heartbeat interval features. *IEEE transactions on biomedical engineering*, 51(7):1196–1206, 2004.

[102] WK Lee, H Yoon, and KS Park. Smart ecg monitoring patch with built-in r-peak detection for long-term hrv analysis. *Annals of biomedical engineering*, 44(7):2292–2301, 2016.

[103] Yishan Wang, Sammy Doleschel, Ralf Wunderlich, and Stefan Heinen. A wearable wireless ecg monitoring system with dynamic transmission power control for long-term homecare. *Journal of medical systems*, 39(3):35, 2015.

[104] Selcan Kaplan Berkaya, Alper Kursat Uysal, Efnan Sora Gunal, Semih Ergin, Serkan Gunal, and M Bilginer Gulmezoglu. A survey on ecg analysis. *Biomedical Signal Processing and Control*, 43:216–235, 2018.

[105] S Suave Lobodzinski and Michael M Laks. New devices for very long-term ecg monitoring. *Cardiology journal*, 19(2):210–214, 2012.

[106] K Ramamohan Rao and Ping Yip. *Discrete cosine transform: algorithms, advantages, applications*. Academic press, 2014.

[107] Pingzhang Zhou, Jianbin Du, and Zhenhua Lü. Highly efficient density-based topology optimization using dct-based digital image compression. *Structural and Multidisciplinary Optimization*, 57(1):463–467, 2018.

[108] Leonardo Vidal Batista, Elmar Uwe Kurt Melcher, and Luis Carlos Carvalho. Compression of ecg signals by optimized quantization of discrete cosine transform coefficients. *Medical engineering & physics*, 23(2):127–134, 2001.

[109] George B Moody, Roger G Mark, and Ary L Goldberger. Evaluation of the trim ecg data compressor. *Computers in Cardiology*, 15:167–170, 1988.

[110] Angela Agostinelli, Micaela Morettini, Agnese Sbrollini, Elvira Maranesi, Lucia Migliorelli, Francesco Di Nardo, Sandro Fioretti, and Laura Burattini. Carisma 1.0: cardiac risk self-monitoring assessment. *The Open Sports Sciences Journal*, 10(1), 2017.

[111] Michael S Emery and Richard J Kovacs. Sudden cardiac death in athletes. *JACC: Heart Failure*, 6(1):30–40, 2018.

[112] Kimberly G Harmon, Monica Zigman, and Jonathan A Drezner. The effectiveness of screening history, physical exam, and ecg to detect potentially lethal cardiac disorders in athletes: a systematic review/meta-analysis. *Journal of Electrocardiology*, 48(3):329–338, 2015.

[113] Shuto Nagai, Daisuke Anzai, and Jianqing Wang. Motion artefact removals for wearable ecg using stationary wavelet transform. *Healthcare technology letters*, 4(4):138–141, 2017.

[114] Shufang Liu, Aurélien Bustin, Darius Burshka, Anne Menini, and Freddy Odille. Gpu implementation of levenberg-marquardt optimization for ti mapping. In *2017 Computing in Cardiology (CinC)*, pages 1–4. IEEE, 2017.

[115] Amnah Nasim, Adnan Maqsood, and Tariq Saeed. Multicore and gpu based pupillometry using parabolic and elliptic hough transform. *International Journal of Mechanical Engineering and Robotics Research*, 6(5), 2017.

[116] Delaram Jarchi and Alexander J Casson. Description of a database containing wrist ppg signals recorded during physical exercise with both accelerometer and gyroscope measures of motion. *Data*, 2(1):1, 2017.

[117] Gene M Amdahl. Validity of the single processor approach to achieving large scale computing capabilities. In *Proceedings of the April 18-20, 1967, spring joint computer conference*, pages 483–485, 1967.

[118] Enea Cippitelli, Samuele Gasparrini, Ennio Gambi, Susanna Spinsante, Jonas Wåhslény, Ibrahim Orhany, and Thomas Lindhy. Time synchronization and data fusion for rgb-depth cameras and inertial sensors in aal applications. In *2015 IEEE International Conference on Communication Workshop (ICCW)*, pages 265–270. IEEE, 2015.

[119] Qingxue Zhang, Chakameh Zahed, Viswam Nathan, Drew A Hall, and Roozbeh Jafari. An ecg dataset representing real-world signal characteristics for wearable computers. In *2015 IEEE Biomedical Circuits and Systems Conference (BioCAS)*, pages 1–4. IEEE, 2015.

[120] Omid Sayadi and Mohammad Bagher Shamsollahi. Ecg denoising and compression using a modified extended kalman filter structure. *IEEE Transactions on Biomedical Engineering*, 55(9):2240–2248, 2008.

[121] D Panigrahy and PK Sahu. P and t wave detection and delineation of ecg signal using differential evolution (de) optimization strategy. *Australasian physical & engineering sciences in medicine*, 41(1):225–241, 2018.

[122] Achuth Rao, Prakhar Gupta, and Prasanta Kumar Ghosh. P-and t-wave delineation in ecg signals using parametric mixture gaussian and dynamic programming. *Biomedical Signal Processing and Control*, 51:328–337, 2019.

[123] D Panigrahy and PK Sahu. Extended kalman smoother with differential evolution technique for denoising of ecg signal. *Australasian physical & engineering sciences in medicine*, 39(3):783–795, 2016.

[124] Pasi Luukka and Jouni Lampinen. A classification method based on principal component analysis and differential evolution algorithm applied for prediction diagnosis from clinical emr heart data sets. In *Computational Intelligence in Optimization*, pages 263–283. Springer, 2010.

[125] Miha Mlakar, Dejan Petelin, Tea Tušar, and Bogdan Filipič. Gp-demo: differential evolution for multiobjective optimization based on gaussian process models. *European Journal of Operational Research*, 243(2):347–361, 2015.

[126] Paweł Pławiak. Novel genetic ensembles of classifiers applied to myocardium dysfunction recognition based on ecg signals. *Swarm and evolutionary computation*, 39:192–208, 2018.

[127] Christian Padilla-Navarro, María del Rosario Baltazar-Flores, David Cuesta-Frau, Arnulfo Alanis Garza, and Víctor Manuel Zamudio Rodríguez. Cardiac arrhythmia classification using knn and naive bayes classifiers optimized with differential evolution (de) and particle swarm optimization (pso). In *Intelligent Environments (Workshops)*, pages 36–46, 2013.

[128] G Sayantan, PT Kien, and KV Kadambari. Classification of ECG beats using deep belief network and active learning. *Medical & Biological Engineering & Computing*, 56(10):1887–1898, 2018.

[129] Fatin A Elhaj, Naomie Salim, Arief R Harris, Tan Tian Swee, and Taqwa Ahmed. Arrhythmia recognition and classification using combined linear and nonlinear features of ECG signals. *Computer methods and programs in biomedicine*, 127:52–63, 2016.

[130] Rashid Ghorbani Afkhami, Ghanbar Azarnia, and Mohammad Ali Tinati. Cardiac arrhythmia classification using statistical and mixture modeling features of ECG signals. *Pattern Recognition Letters*, 70:45–51, 2016.

[131] Tong Liu, Yujuan Si, Dunwei Wen, Mujun Zang, and Liuqi Lang. Dictionary learning for vq feature extraction in ECG beats classification. *Expert Systems with Applications*, 53:129–137, 2016.

[132] Chia-Ping Shen, Wen-Chung Kao, Yueh-Yiing Yang, Ming-Chai Hsu, Yuan-Ting Wu, and Feipei Lai. Detection of cardiac arrhythmia in electrocardiograms using adaptive feature extraction and modified support vector machines. *Expert Systems with Applications*, 39(9):7845–7852, 2012.

[133] Qin Qin, Jianqing Li, Li Zhang, Yinggao Yue, and Chengyu Liu. Combining low-dimensional wavelet features and support vector machine for arrhythmia beat classification. *Scientific reports*, 7(1):6067, 2017.

[134] Xiaolong Zhai and Chung Tin. Automated ECG classification using dual heartbeat coupling based on convolutional neural network. *IEEE Access*, 6:27465–27472, 2018.

[135] Shu Lih Oh, Eddie YK Ng, Ru San Tan, and U Rajendra Acharya. Automated diagnosis of arrhythmia using combination of CNN and LSTM techniques with variable length heart beats. *Computers in biology and medicine*, 102:278–287, 2018.

[136] Yuwei Zhang, Yuan Zhang, Benny Lo, and Wenyao Xu. Wearable ECG signal processing for automated cardiac arrhythmia classification using cfase-based feature selection. *Expert Systems*, page e12432, 2019.

[137] Ozal Yildirim, Ulas Baran Baloglu, Ru-San Tan, Edward J Ciaccio, and U Rajendra Acharya. A new approach for arrhythmia classification using deep coded features and LSTM networks. *Computer methods and programs in biomedicine*, 176:121–133, 2019.

[138] Turker Tuncer, Sengul Dogan, Paweł Pławiak, and U Rajendra Acharya. Automated arrhythmia detection using novel hexadecimal local pattern and multilevel wavelet transform with ECG signals. *Knowledge-Based Systems*, 186:104923, 2019.

[139] Jeen-Shing Wang, Wei-Chun Chiang, Yu-Liang Hsu, and Ya-Ting C Yang. ECG arrhythmia classification using a probabilistic neural network with a feature reduction method. *Neurocomputing*, 116:38–45, 2013.

[140] Felipe Alonso-Atienza, Eduardo Morgado, Lorena Fernandez-Martinez, Arcadi García-Alberola, and José Luis Rojo-Alvarez. Detection of life-threatening arrhythmias using feature selection and support vector machines. *IEEE Transactions on Biomedical Engineering*, 61(3):832–840, 2013.

[141] Ying-Hsiang Chen and Sung-Nien Yu. Selection of effective features for ECG beat recognition based on nonlinear correlations. *Artificial intelligence in medicine*, 54(1):43–52, 2012.

[142] Hassan Hamsa Haseena, Abraham T Mathew, and Joseph K Paul. Fuzzy clustered probabilistic and multi layered feed forward neural networks for electrocardiogram arrhythmia classification. *Journal of Medical Systems*, 35(2):179–188, 2011.

[143] Rahime Ceylan and Yüksel Özbay. Comparison of FCM, PCA and WT techniques for classification ECG arrhythmias using artificial neural network. *Expert Systems with Applications*, 33(2):286–295, 2007.

[144] Kemal Polat and Salih Güneş. Detection of ECG arrhythmia using a differential expert system approach based on principal component analysis and least square support vector machine. *Applied Mathematics and Computation*, 186(1):898–906, 2007.

[145] Özal Yildirim and Ulas Baran Baloglu. Heartbeat type classification with optimized feature vectors. *An International Journal of Optimization and Control: Theories & Applications (IJOCTA)*, 8(2):170–175, 2018.

[146] Essam H Houssein, Ahmed A Ewees, and Mohamed Abd ElAziz. Improving twin support vector machine based on hybrid swarm optimizer for heartbeat classification. *Pattern Recognition and Image Analysis*, 28(2):243–253, 2018.

[147] Hongqiang Li, Danyang Yuan, Xiangdong Ma, Dianyin Cui, and Lu Cao. Genetic algorithm for the optimization of features and neural networks in ECG signals classification. *Scientific reports*, 7:41011, 2017.

[148] Sophia Daskalaki, Ioannis Kopanas, and Nikolaos Avouris. Evaluation of classifiers for an uneven class distribution problem. *Applied artificial intelligence*, 20(5):381–417, 2006.

[149] Kai Wei Sun and Chong Ho Lee. Addressing class-imbalance in multi-label learning via two-stage multi-label hypernetwork. *Neurocomputing*, 266:375–389, 2017.

[150] Hualong Yu, Changyin Sun, Xibei Yang, Wankou Yang, Jifeng Shen, and Yunsong Qi. ODOC-ELM: Optimal decision outputs compensation-based extreme learning machine for classifying imbalanced data. *Knowledge-Based Systems*, 92:55–70, 2016.

[151] Brian W Matthews. Comparison of the predicted and observed secondary structure of t4 phage lysozyme. *Biochimica et Biophysica Acta (BBA)-Protein Structure*, 405(2):442–451, 1975.

[152] Leming Shi, Gregory Campbell, Wendell D Jones, Fabien Campagne, Zhining Wen, Stephen J Walker, Zhenqiang Su, Tzu-Ming Chu, Federico M Goodsaid, Lajos Pusztai, et al. The microarray quality control (MAQC)-ii study of

common practices for the development and validation of microarray-based predictive models. *Nature biotechnology*, 28(8):827, 2010.

[153] Rainer Storn and Kenneth Price. Differential evolution–a simple and efficient heuristic for global optimization over continuous spaces. *Journal of global optimization*, 11(4):341–359, 1997.

[154] Hans-Paul Schwefel and Günter Rudolph. Contemporary evolution strategies. In *European conference on artificial life*, pages 891–907. Springer, 1995.

[155] John R Koza and John R Koza. *Genetic programming: on the programming of computers by means of natural selection*, volume 1. MIT press, 1992.

[156] Donald F Specht and Harlan Romsdahl. Experience with adaptive probabilistic neural networks and adaptive general regression neural networks. In *Proceedings of 1994 IEEE International Conference on Neural Networks (ICNN'94)*, volume 2, pages 1203–1208. IEEE, 1994.

[157] Yasha Zeinali and Brett A Story. Competitive probabilistic neural network. *Integrated Computer-Aided Engineering*, 24(2):105–118, 2017.

[158] Vincent Cheung and Kevin Cannons. An introduction to probabilistic neural networks. *Retrieved August*, 2:2011, 2003.

[159] Zbigniew Michalewicz and Marc Schoenauer. Evolutionary algorithms for constrained parameter optimization problems. *Evolutionary computation*, 4(1):1–32, 1996.

[160] Rogene M Eichler West, Erik De Schutter, and George L Wilcox. Using evolutionary algorithms to search for control parameters in a nonlinear partial differential equation. In *Evolutionary Algorithms*, pages 33–64. Springer, 1999.

[161] Carlos A Coello Coello and Arturo Hernández Aguirre. Design of combinational logic circuits through an evolutionary multiobjective optimization approach. *Artificial Intelligence for Engineering Design, Analysis and Manufacturing: AI EDAM*, 16(1):39, 2002.

[162] Daniele Marinucci, Agnese Sbrollini, Ilaria Marcantoni, Micaela Morettini, Cees A Swenne, and Laura Burattini. Artificial neural network for atrial fibrillation identification in portable devices. *Sensors*, 20(12):3570, 2020.

[163] Ferrante Neri and Ville Tirronen. Recent advances in differential evolution: a survey and experimental analysis. *Artificial Intelligence Review*, 33(1-2):61–106, 2010.

[164] Ming Yang, Zhihua Cai, Changhe Li, and Jing Guan. An improved adaptive differential evolution algorithm with population adaptation. In *Proceedings of*

the 15th annual conference on Genetic and evolutionary computation, pages 145–152. ACM, 2013.

[165] Jan Gorodkin. Comparing two k-category assignments by a k-category correlation coefficient. *Computational biology and chemistry*, 28(5-6):367–374, 2004.

[166] Huaiyu Zhu, Yun Pan, Fan Wu, and Ruohong Huan. Optimized electrode locations for wearable single-lead ECG monitoring devices: A case study using WFEES modules based on the LANS method. *Sensors*, 19(20):4458, 2019.

[167] Jianhua Xu. An extended one-versus-rest support vector machine for multi-label classification. *Neurocomputing*, 74(17):3114–3124, 2011.

[168] Tae Joon Jun, Hoang Minh Nguyen, Daeyoun Kang, Dohyeun Kim, Daeyoung Kim, and Young-Hak Kim. ECG arrhythmia classification using a 2-d convolutional neural network. *arXiv preprint arXiv:1804.06812*, 2018.

[169] Gabriel Garcia, Gladston Moreira, David Menotti, and Eduardo Luz. Inter-patient ECG heartbeat classification with temporal VCG optimized by PSO. *Scientific reports*, 7(1):10543, 2017.

[170] Norbert Marwan, M Carmen Romano, Marco Thiel, and Jürgen Kurths. Recurrence plots for the analysis of complex systems. *Physics reports*, 438(5-6):237–329, 2007.

[171] Charles L Webber Jr and Joseph P Zbilut. Dynamical assessment of physiological systems and states using recurrence plot strategies. *Journal of applied physiology*, 76(2):965–973, 1994.

[172] Norbert Marwan. A historical review of recurrence plots. *The European Physical Journal Special Topics*, 164(1):3–12, 2008.

[173] Joseph P Zbilut and Charles L Webber Jr. Embeddings and delays as derived from quantification of recurrence plots. *Physics letters A*, 171(3-4):199–203, 1992.

[174] Norbert Marwan, Niels Wessel, Udo Meyerfeldt, Alexander Schirdewan, and Jürgen Kurths. Recurrence-plot-based measures of complexity and their application to heart-rate-variability data. *Physical review E*, 66(2):026702, 2002.

[175] Fotini Patrona, Anargyros Chatzitofis, Dimitrios Zarpalas, and Petros Daras. Motion analysis: Action detection, recognition and evaluation based on motion capture data. *Pattern Recognition*, 76:612–622, 2018.

[176] Øyvind Gløersen, Håvard Myklebust, Jostein Hallén, and Peter Federolf. Technique analysis in elite athletes using principal component analysis. *Journal of sports sciences*, 36(2):229–237, 2018.

[177] Andreas Aristidou, Efstathios Stavrakis, Margarita Papaefthimiou, George Papagiannakis, and Yiorgos Chrysanthou. Style-based motion analysis for dance composition. *The visual computer*, 34(12):1725–1737, 2018.

[178] G Elhayatmy, Nilanjan Dey, and Amira S Ashour. Internet of things based wireless body area network in healthcare. In *Internet of things and big data analytics toward next-generation intelligence*, pages 3–20. 2018.

[179] Naishi Feng, Qiurong Shi, Hong Wang, Jiale Gong, Chong Liu, and Zhiguo Lu. A soft robotic hand: design, analysis, semg control, and experiment. *The International Journal of Advanced Manufacturing Technology*, 97(1-4):319–333, 2018.

[180] Nicola C Anderson, Walter F Bischof, Kaitlin EW Laidlaw, Evan F Risko, and Alan Kingstone. Recurrence quantification analysis of eye movements. *Behav Res Methods.*, 45(3):842–856, 2013.

[181] Amnah Nasim, Ilaria Marcantoni, Agnese Sbrollini, Micaela Morettini, and Laura Burattini. Recurrence quantification analysis for motion artifacts in wearable ecg sensors. In *2019 IEEE 23rd International Symposium on Consumer Technologies (ISCT)*, pages 206–209. IEEE, 2019.

[182] Timothy R Brick, Allison L Gray, and Angela D Staples. Recurrence quantification for the analysis of coupled processes in aging. *The Journals of Gerontology: Series B*, 73(1):134–147, 2018.

[183] Reik V Donner, Yong Zou, Jonathan F Donges, Norbert Marwan, and Jürgen Kurths. Recurrence networks—a novel paradigm for nonlinear time series analysis. *New Journal of Physics*, 12(3):033025, 2010.

[184] Norbert Marwan, M Carmen Romano, Marco Thiel, and Jürgen Kurths. Recurrence plots for the analysis of complex systems. *Physics reports*, 438(5-6):237–329, 2007.

[185] Constantin Ovidiu Ilie, Octavian Alexa, Ion Lespezeanu, Marin Marinescu, and Dănuț Grosu. Recurrence plot analysis to study parameters of a gasoline engine. In *Applied Mechanics and Materials*, volume 823, pages 323–328, 2016.

[186] Paolo Melillo, Raffaele Izzo, Ada Orrico, Paolo Scala, Marcella Attanasio, Marco Mirra, Nicola De Luca, and Leandro Pecchia. Automatic prediction of cardiovascular and cerebrovascular events using heart rate variability analysis. *PLoS One.*, 10(3):e0118504, 2015.

[187] *Nonlinear Time Series Analysis in the Geosciences-Applications in Climatology, Geodynamics and Solar-Terrestrial Physics*, 112, 2008.

[188] Jeremy Morton, Tim A Wheeler, and Mykel J Kochenderfer. Analysis of recurrent neural networks for probabilistic modeling of driver behavior. *IEEE Transactions on Intelligent Transportation Systems*, 18(5):1289–1298, 2017.

[189] Francesca Sylos Labini, Annalisa Meli, Yuri P Ivanenko, and Davide Tufarelli. Recurrence quantification analysis of gait in normal and hypovestibular subjects. *Gait & posture*, 35(1):48–55, 2012.

[190] Paola Pierleoni, Alberto Belli, Lorenzo Palma, Marco Pellegrini, Luca Pernini, and Simone Valenti. A high reliability wearable device for elderly fall detection. *IEEE Sensors Journal*, 15(8):4544–4553, 2015.

[191] Angela Agostinelli, Micaela Morettini, Agnese Sbrollini, Elvira Maranesi, Lucia Migliorelli, Francesco Di Nardo, Sandro Fioretti, and Laura Burattini. Carisma 1.0: cardiac risk self-monitoring assessment. *The Open Sports Sciences Journal*, 10(1), 2017.

[192] Subhas Chandra Mukhopadhyay. Wearable sensors for human activity monitoring: A review. *IEEE sensors journal*, 15(3):1321–1330, 2015.

[193] Niels Wessel, Norbert Marwan, Udo Meyerfeldt, Alexander Schirdewan, and Jürgen Kurths. Recurrence quantification analysis to characterise the heart rate variability before the onset of ventricular tachycardia. In *International Symposium on Medical Data Analysis*, pages 295–301. Springer, 2001.

[194] Vahid Behravan, Neil E Glover, Rutger Farry, Patrick Y Chiang, and Mohammed Shoaib. Rate-adaptive compressed-sensing and sparsity variance of biomedical signals. In *2015 IEEE 12th International Conference on Wearable and Implantable Body Sensor Networks (BSN)*, pages 1–6. IEEE, 2015.

[195] Stephen M Glass, Christopher K Rhea, Randy J Schmitz, and Scott E Ross. Potential mediators of load-related changes in movement complexity in young, healthy adults. *Journal of athletic training*, 54(1):70–80, 2019.

[196] Aviroop Dutt-Mazumder, Adam C King, and Karl M Newell. Recurrence dynamics reveals differential control strategies to maintain balance on sloped surfaces. *Gait & posture*, 69:169–175, 2019.

[197] Cameron T Gibbons, Polemnia G Amazeen, and Jen J Jondac. Thinking on your feet: An analysis of movement and cognition in a sit to stand task. *Acta psychologica*, 192:52–58, 2019.

[198] Valentina Cotechini, Alberto Belli, Lorenzo Palma, Micaela Morettini, Laura Burattini, and Paola Pierleoni. A dataset for the development and optimization of fall detection algorithms based on wearable sensors. *Data in Brief*, 23:103839, 2019.

[199] Tony Luxton and Jackie Riglin. Preventing falls in older people: a multi-agency approach. *Nursing Older People (through 2013)*, 15(2):18, 2003.

[200] F Riva, MJP Toebes, MAGM Pijnappels, R Stagni, and JH Van Dieën. Estimating fall risk with inertial sensors using gait stability measures that do not require step detection. *Gait & posture*, 38(2):170–174, 2013.

[201] Muhammad Mubashir, Ling Shao, and Luke Seed. A survey on fall detection: Principles and approaches. *Neurocomputing*, 100:144–152, 2013.

[202] Nashwa El-Bendary, Qing Tan, Frédérique C Pivot, and Anthony Lam. Fall detection and prevention for the elderly: A review of trends and challenges. *International Journal on Smart Sensing & Intelligent Systems*, 6(3), 2013.

[203] Natthapon Pannurat, Surapa Thiemjarus, and Ekawit Nantajeewarawat. Automatic fall monitoring: a review. *Sensors*, 14(7):12900–12936, 2014.